

AD-A169 635

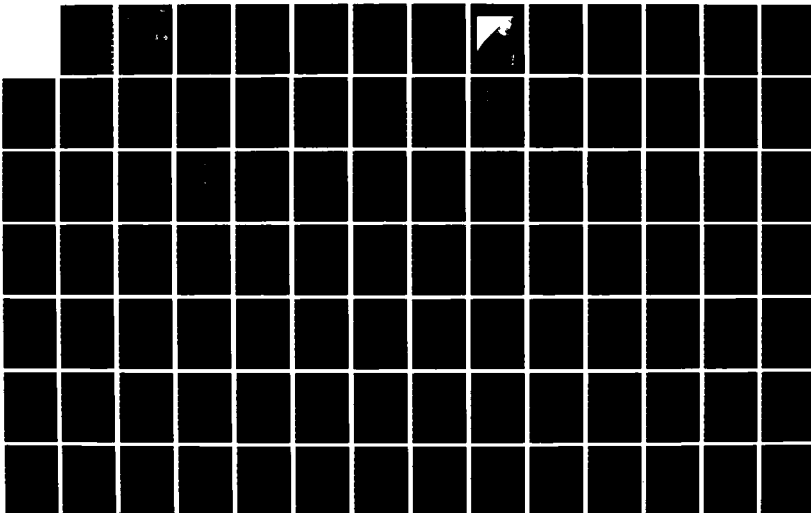
PHASED ARRAY LASER SYSTEM (PALS)(U) TRW SPACE AND
TECHNOLOGY GROUP REDONDO BEACH CA APPLIED TECHNOLOGY
DIV A D SCHNURR ET AL. 09 JUL 86 N00014-85-C-2338

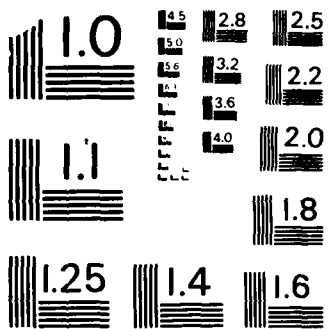
1/2

UNCLASSIFIED

F/G 20/5

NL





MICROCOPY RESOLUTION TEST CHART
NATIONAL BUREAU OF STANDARDS-1963-A

AD-A169 635

12



Phased Array Laser System (PALS)

Alvin D. Schnurr
TRW, Inc.
One Space Park, 01/1270
Redondo Beach, CA 90278

09 July 1986
Final Report

DTIC
ELECTE
JUL 10 1986
S D

Prepared for
Strategic Defense Initiative Office
1717 H Street
Washington, D.C.

DTIC FILE COPY

Naval Research Laboratory
4555 Overlook Avenue
Washington, D.C. 20375

This document has been approved
for public release and sale; its
distribution is unlimited.

86 7 10 005

REPORT DOCUMENTATION PAGE

| | | | |
|---|---|--|----------------------|
| 1a REPORT SECURITY CLASSIFICATION Unclassified | | 1b RESTRICTIVE MARKINGS Per clause H-9. | |
| 2a SECURITY CLASSIFICATION AUTHORITY OPNAVINST 5513.8(7) | | 3 DISTRIBUTION/AVAILABILITY OF REPORT Unlimited | |
| 2b DECLASSIFICATION/DOWNGRADING SCHEDULE OADR | | | |
| 4 PERFORMING ORGANIZATION REPORT NUMBER(S) N00014-85-C-2338 | | 5 MONITORING ORGANIZATION REPORT NUMBER(S) Naval Research Laboratory | |
| 6a NAME OF PERFORMING ORGANIZATION Applied Technology Division TRW Space and Technology Group | 6b OFFICE SYMBOL (If applicable) | 7a NAME OF MONITORING ORGANIZATION Naval Research Laboratory | |
| 6c ADDRESS (City, State, and ZIP code) One Space Park Redondo Beach, CA 90278 | | 7b ADDRESS (City, State, and ZIP code) Washington, D.C. 20375-5000 | |
| 8a NAME OF FUNDING/SPONSORING ORGANIZATION Naval Research Laboratory | 8b OFFICE SYMBOL (If applicable) | 9 PROCUREMENT INSTRUMENT IDENTIFICATION NUMBER | |
| 8c ADDRESS (City, State, and ZIP code) Washington, D.C. 20375-5000 | | 10 SOURCE OF FUNDING NOS | |
| 11 TITLE (Include Security Classification) Phased Array Laser System (PALS) | | PROGRAM ELEMENT NO | TASK NO |
| | | PROJECT NO | WORK UNIT NO |
| 12 PERSONAL AUTHOR(S) A. Schnurr, S. Meisenholder, M. Litvak, S. Quon, G. Koop, D. Dee, R. Wagner, M. Valley, S. Lissit, T. Mandre, M. DelleDonne, V. Chai, M. Piliavin | | | |
| 13a TYPE OF REPORT Final | 13b TIME COVERED FROM Jul 1985 TO Jul 1986 | 14 DATE OF REPORT (Yr. Mo. Day) 1986 Jul 09 | 15 PAGE COUNT 146 |
| 16 SUPPLEMENTARY NOTATION | | | |
| 17 COSATI CODES | | 18 SUBJECT TERMS (Continue on reverse if necessary and identify by block number) | |
| FIELD | GROUP | phased-array laser system, master oscillator, power amplifier, phase conjugator, beam director | |
| | SUB GR | | |
| 19 ABSTRACT (Continue on reverse if necessary and identify by block number) This final report for the Phased Array Laser System (PALS) project presents analyses and design approaches for a high brightness space-based HF phase-conjugate laser system answering current SDI needs. These efforts, both analytic and subscale experimental, are first steps toward a conceptual design for an SDI SBL system with substantial advantages over conventional non-phase-conjugate systems. The analyses deal with the master oscillator, power amplifier, phase conjugation and beam director subsystems. ALPHA-type devices comprising the MOPA are modeled with the ANOM/CLAM/LFCM codes. The assembly for separating the high power conjugated beam from the low power master oscillator beam is modeled with a French polarization grating code and U of Arizona and OCLI quarter-wave retarder codes. A phase-conjugator SBS cell with 40-atm xenon is modeled with BOUNCE/BRIWON codes. Multisegmented primary and monolithic secondary mirror beam director assemblies are modeled with wave optics codes developed in this project. Subscale experiments on xenon gas and CCl ₄ liquid SBS phase conjugation explored dependence of SBS reflectivity and conjugation fidelity on parameters such as beam quality degradation by aberrators and on the f/number of the focusing geometry. | | | |
| 20 DISTRIBUTION/AVAILABILITY OF ABSTRACT UNCLASSIFIED/UNLIMITED <input checked="" type="checkbox"/> SAME AS RPT <input type="checkbox"/> DTIC USERS <input type="checkbox"/> | | 21 ABSTRACT SECURITY CLASSIFICATION UNCLASSIFIED | |
| 22a NAME OF RESPONSIBLE INDIVIDUAL A.D. Schnurr | | 22b TELEPHONE NUMBER (include Area Code) 213-536-1200 | 22c OFFICE SYMBOL |

CONTENTS

| | Page |
|--|------|
| 1. INTRODUCTION | 1 |
| 1.1 Project Summary | 1 |
| 2.1 System Requirements | 3 |
| 2.2 System Design Approach | 3 |
| 2.3 Subsystem Design Approaches and Analysis | 5 |
| 2.3.1 Master Oscillator and Power Amplifier (MOPA) Subsystems | 5 |
| 2.3.2 Phase-Conjugation Subsystem | 6 |
| 2.3.3 Beam Director Subsystem | 8 |
| 3. MISSION REQUIREMENTS, GUIDELINES, AND MISSION ANALYSIS | 9 |
| 3.1 Starting Point | 9 |
| 3.2 Mission Requirements | 10 |
| 3.3 Mission Analysis | 11 |
| 4. PALS Subsystem Overview | 15 |
| 4.1 Functional Description | 15 |
| 4.2 Subsystem Description | 17 |
| 4.2.1 Oscillator Subsystem | 17 |
| 4.2.2 Power Amplifier Subsystem | 17 |
| 4.2.3 Beam Director Subsystem | 18 |
| 4.2.4 Phase-Conjugation Subsystem | 19 |
| 4.3 Preliminary Power Budget | 21 |
| 5. MOPA (MASTER OSCILLATOR AND POWER AMPLIFIER) SUBSYSTEMS | 23 |
| 5.1 MOPA Subsystem Preliminary Concept and Trade Studies | 23 |
| 5.2 MOPA Extraction Efficiency and Beam Quality | 26 |
| 5.2.1 ALPHA Device Amplifier Models in LFCM | 27 |
| 5.2.2 Master Oscillator Power Requirements | 32 |
| 5.2.3 Effect of SBS Shift on MOPA Extraction Efficiency | 34 |

CONTENTS (Continued)

| | Page | |
|-------|---|-----|
| 5.2.4 | Effect of Gain Distribution | 34 |
| 5.2.5 | Interaction of Gain Saturation with Phase Conjugation | 36 |
| 5.2.6 | Phase Screens for the LFCM Code | 38 |
| 5.2.7 | Extraction Efficiency | 46 |
| 5.2.8 | PALS MOPA System Model Upgrade | 61 |
| 5.3 | Low/High Power Beam Separation Grating Rhomb Isolation Study | 67 |
| 5.3.1 | Grating Rhomb Design Goals | 69 |
| 5.3.2 | French Grating Code Results | 69 |
| 5.3.3 | Grating Subscale Results | 76 |
| 5.3.4 | Summary | 76 |
| 5.4 | Quarter-Wave Retarder Study | 77 |
| 5.4.1 | Discussion | 78 |
| 5.4.2 | Summary | 81 |
| 6. | BEAM DIRECTOR SUBSYSTEM | 82 |
| 6.1 | Beam Director Preliminary Concept and Trade Issues | 82 |
| 6.1.1 | Objective and Approach | 82 |
| 6.1.2 | Beam Director Major Trade Issues | 82 |
| 6.1.3 | Beam Director Preliminary Configuration Summary | 85 |
| 6.2 | Geometric Optics Multisegment Beam Director Subsystem | 85 |
| 6.2.1 | Introduction to MICROCODE | 85 |
| 6.3 | Wave Optics Analyses of Multisegment Beam Director Subsystem - Multisegment Beam Director Misalignment Analysis | 91 |
| 6.3.1 | The Model | 91 |
| 6.3.2 | Calculations and Results | 109 |

CONTENTS (Continued)

| | | Page |
|-------|---|------|
| 7. | PHASE CONJUGATION SUBSYSTEM | 119 |
| 7.1 | Phase Conjugation Subsystem Preliminary Concept and Trade Studies | 119 |
| 7.1.1 | Objective and Approach | 119 |
| 7.1.2 | Phase Conjugation Major Trade Issues | 119 |
| 7.1.3 | Preliminary Configuration | 121 |
| 7.2 | Phase Conjugation Analysis | 121 |
| 7.2.1 | SBS Modeling | 121 |
| 7.2.2 | Competition with SBS | 126 |
| 7.2.3 | Thermal Blooming, Self-Focusing, and IR Gas Breakdown in SBS Cell | 128 |
| 7.3 | Subscale Experiments | 134 |



| | |
|--------------------|-------------------------------------|
| Accession For | |
| NTIS CRA&I | <input checked="" type="checkbox"/> |
| DTIC TAB | <input type="checkbox"/> |
| Unannounced | <input type="checkbox"/> |
| Justification | |
| By | |
| Distribution/ | |
| Availability Codes | |
| Dist | Avail and/or special |
| A-1 | |

1. INTRODUCTION

1.1 PROJECT SUMMARY

This report presents the results of the Phased Array Laser System (PALS) project. During the PALS project, analyses and design approaches were developed for a space-based HF phase-conjugate laser system. The preliminary configuration reviewed in this report is the result of a number of modeling and analytical efforts, and some subscale testing and data review, aimed at providing the first step toward an eventual system conceptual design.

It is anticipated that HF phase-conjugation technology development, made possible by this project, may become the basis for an SDI SBL system design. Such a system has substantial advantages of design and performance margin over more conventional, non-phase-conjugate systems. In a phase-conjugate system, device beam quality is limited only by the beam quality of a small oscillator which, given the low oscillator power requirement, can be near-diffraction limited. Furthermore, the key requirement of multiple device coupling requires minimal alignment control (~ 5 waves of angular alignment, and ~ 3 meters of piston control). Similarly, output device jitter depends only on the jitter of the small oscillator, with high energy laser (HEL) device jitter corrected to > 1 MHz. These performance and design advantages provided powerful motivation for the PALS project, which has developed initial approaches to the design of such a system.

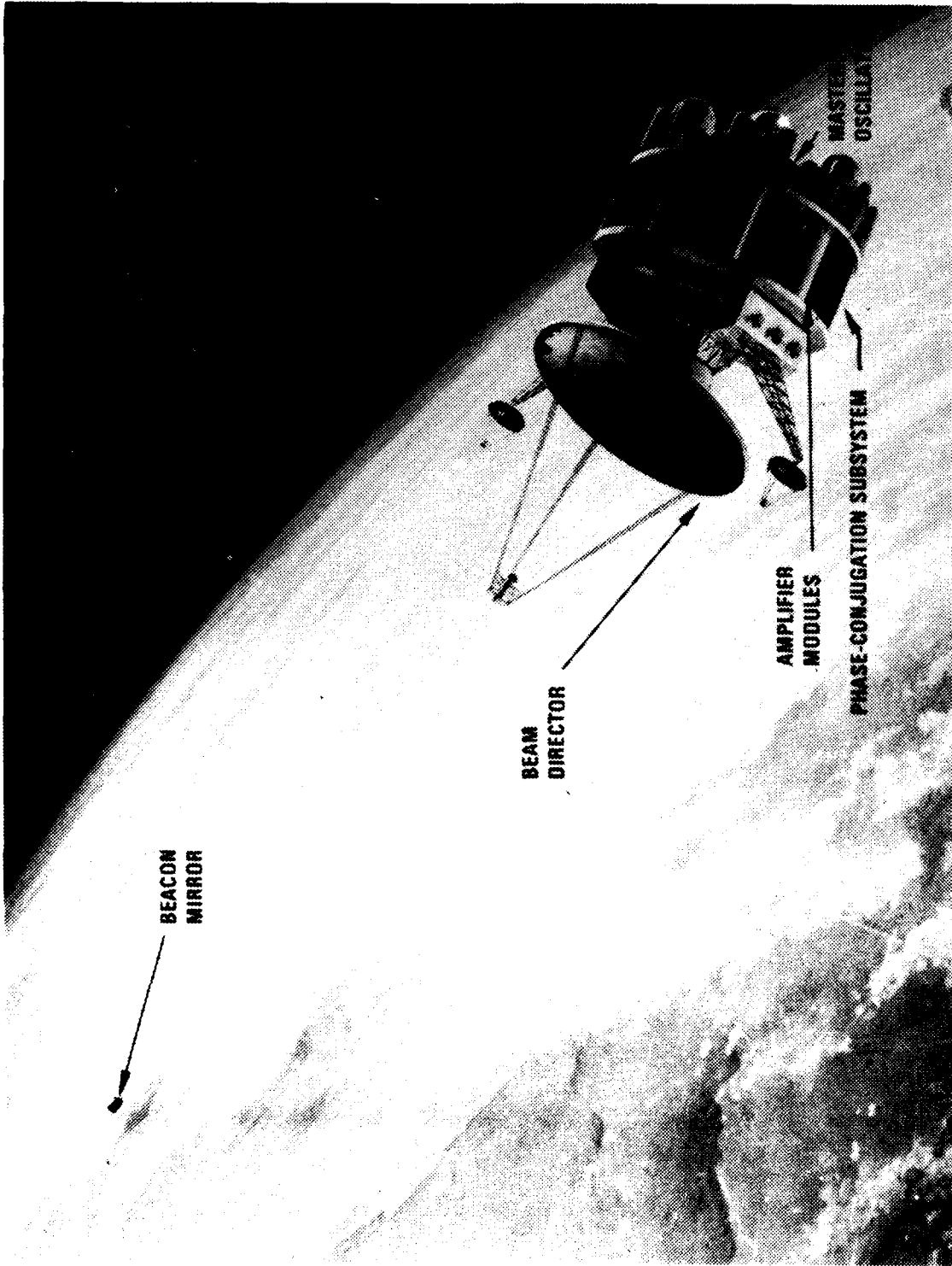


Figure 1-1. Phased array laser concept -- artist's concept.

2. PROJECT SUMMARY

2.1 SYSTEM REQUIREMENTS

The PALS mission requirements, most of which are classified (Ref. 2.1), are based on the SDIO SBL 1985 technical guidelines document. More specific requirements were based on the Lockheed SBL Phase IIB mission analysis report, as a typical example of SBL brightness levels. However, the PALS phase-conjugate design has a key advantage over conventional HEL systems for brightness scalability: In a phase-conjugate design, complexity is not a strong function of system power and diameter. This feature makes the PALS approach intrinsically scalable to much higher brightness levels.

2.2 SYSTEM DESIGN APPROACH

The performance benefits provided by nonlinear phase conjugation for an SBL system design can be maximized by changing the design at the system level. Ultimately, this technology makes possible two important areas of performance improvement:

- o Transfer of virtually the complete HEL beam quality and jitter budgets from the HEL device to a low power oscillator subsystem
- o Phase-locking of multiple HEL gain generator outputs.

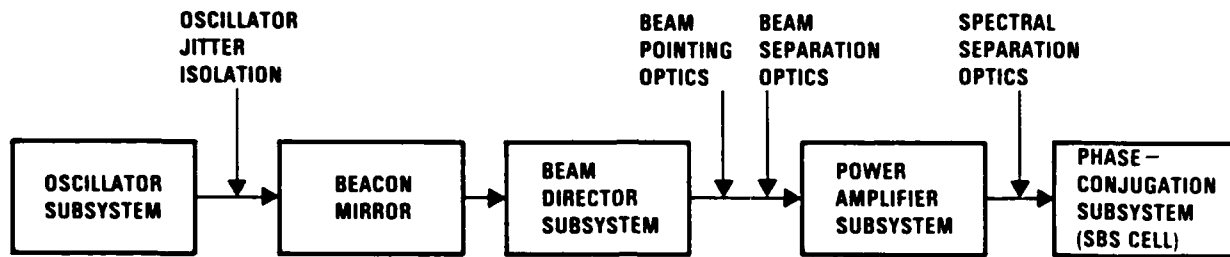
The system configuration that achieves this is a Bidirectional Phase Conjugate MOPA. As shown in the functional block diagram in Figure 2-1, there are four subsystems:

- o Oscillator subsystem
- o Power amplifier subsystem
- o Beam director subsystem
- o Phase conjugation subsystem

The oscillator subsystem provides a reference beam which will define the beam quality and jitter of the full HEL system after later amplification and conjugation. The output reference beam from this subsystem propagates to a beacon mirror, which would be the key element on a very small, separate beacon satellite used only for that purpose. The beam leaving the beacon diverges to fill the composite primary of a single-aperture telescope, which then focuses the beam to a demagnified size on a telescope secondary mirror. The beam at this point includes OPD information such as

2.1 "Final PALS Mission Requirements and Guidelines Document (U)," TRW AP-0382, 19 Feb 1986 (Secret).

Forward Trip



Return Trip

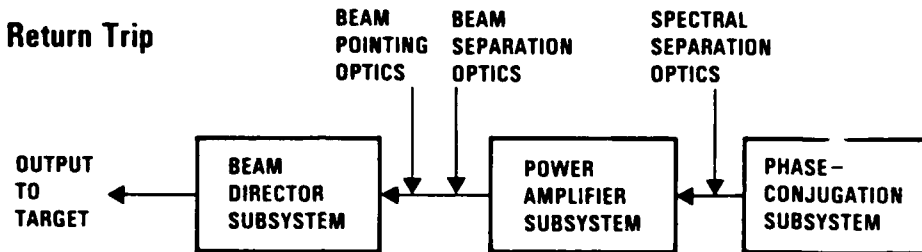


Figure 2-1. Phased array laser system (PALS).

the relative piston errors of the composite primary. After propagation through the next subsystem, the power amplifier subsystem, these and other accumulated OPD errors and jitter will be conjugated in the phase conjugation subsystem.

As the conjugate beam returns through the HEL system, it corrects for the original OPDs by passing back through them with their phase conjugate. As it leaves the power amplifier subsystem, the beam passes through beam separation optics which direct the beam through a somewhat different optical path, so that the final output beam is approximately collimated (directed to a target) after correcting primary mirror piston errors. Figure 2-1 is a block diagram which shows the relationship between the different subsystems.

2.3 SUBSYSTEM DESIGN APPROACHES AND ANALYSIS

2.3.1 Master Oscillator and Power Amplifier (MOPA) Subsystems

The MOPA activity was principally concerned with development of preliminary constraints to guide selection of the number and size of HEL amplifiers. This activity also involved modeling to define the oscillator size required to suppress ASE and to provide good extraction from the power amplifiers.

Preliminary selection of appropriate design ranges was made by modifying the LFCM amplifier model to include HF kinetics. This model was used to look at both extraction efficiency and ASE issues as a function of the relative sizes of the oscillator and amplifier subsystems. The ANOM and CLAM models were also used to look at the effects of SBS Doppler shifting on extraction efficiency; the results of this effort showed that Doppler shift compensation using a near-sonic axial xenon flow is unnecessary to get good extraction.

At the conclusion of this modeling effort, review of the results showed that the required oscillator and amplifier sizes are well within the capability ranges of HF gain generators. This result was based on assessments of the power needed to meet three requirements:

1. Adequate margin over the SBS threshold at the SBS subsystem
2. Good overall amplifier extraction efficiency
3. ASE suppression.

Modularity of the amplifiers makes them particularly well-suited to any further power scaling that may be necessitated by increases in requirements on future systems. Figure 2-2 shows the power amplifier subsystem.

Another activity included in this effort was development of beam separation approaches. Beam separation techniques using a polarization separation grating rhomb and optically active coatings were modeled, and preliminary design approaches look effective.

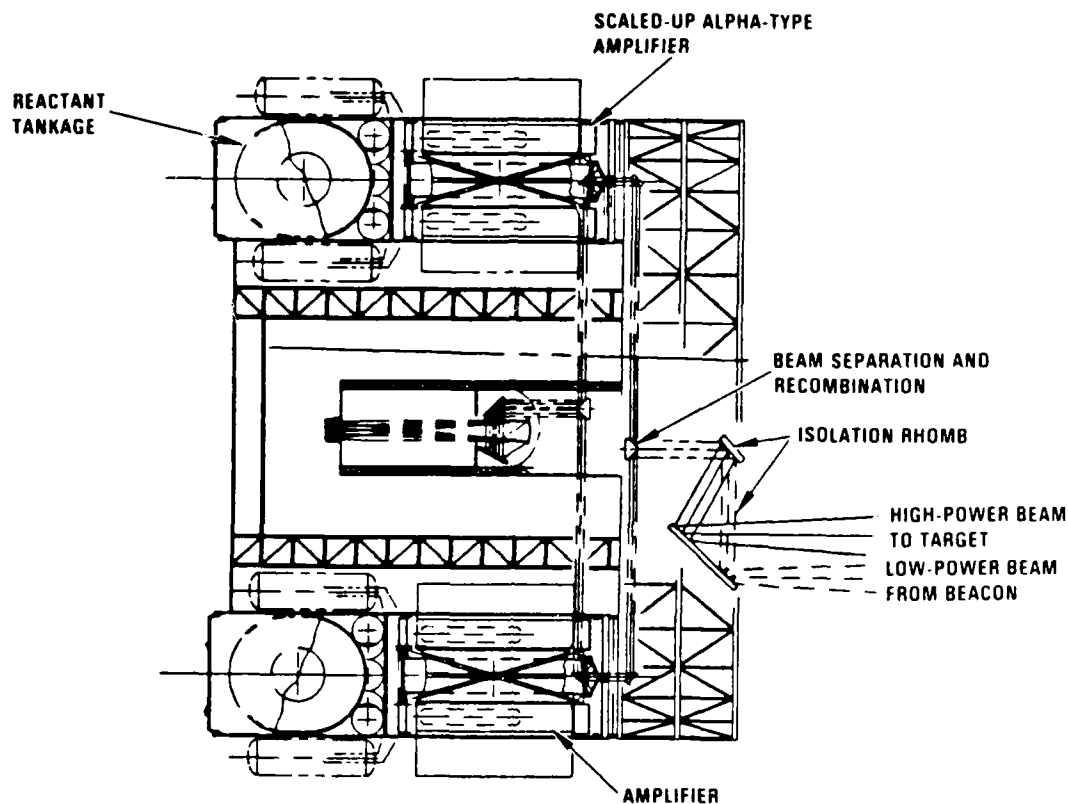
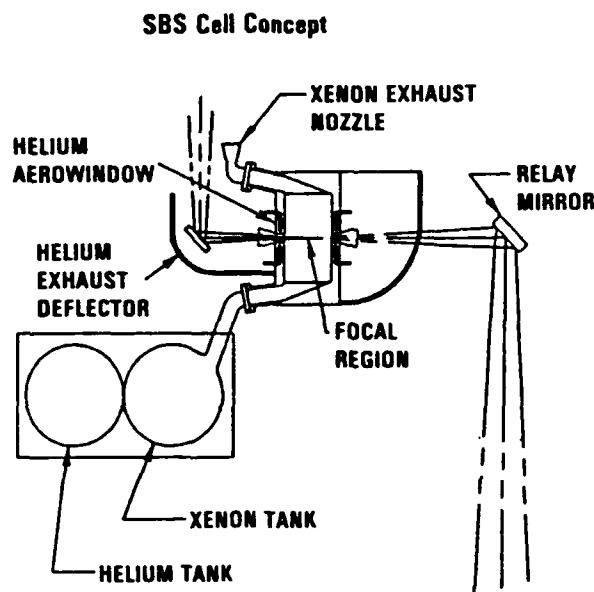


Figure 2-2. Power amplifier subsystem.

2.3.2 Phase-Conjugation Subsystem

Utilization of the BOUNCE SBS phase conjugation model was particularly key to development of design approaches for this subsystem. Using this model, the SBS threshold was derived, and the result was similar to although somewhat lower than that measured in NRL experiments. The derived value is well-suited to the SBL operating point.

One important feature of the SBS subsystem is the design approach and approximate size and complexity required for the flowing SBS cell. Due to the similarity between design requirement for a pulsed design and a CW design flowing cell, it was possible to use conceptual designs available GFE from an HF conjugation experiment design program (CLPCT). Figure 2-3 shows features of the preliminary design concept.



Primary features

- Flowing xenon cell at 40 atm pressure, 300 K temperature
- Cross flow velocity between 20–80 m/s
- Individual cells for each laser line
- Based on results of BOUNCE code computer model of SBS process

Figure 2-3. PALS preliminary design concept.

Additional work done in this area included some subscale testing on basic SBS issues, and beam combination modeling done with the BOUNCE code. The modeling effort yielded an initial design point for multiple beam combination geometry, using 40 atm xenon, as discussed below.

2.3.3 Beam Director Subsystem

The baseline beam director design developed on this project was aimed at meeting the two most basic design constraints:

1. Bidirectional operation to permit conjugation of multisegment piston errors
2. Reasonable field of view to allow pointing within a target field without moving the primary.

Conjugation of the beam director is a powerful tool to increase performance margins and reduce the otherwise severe segment-to-segment alignment constraints; primary mirror conjugation yields ~ 2 orders of magnitude improvement in piston error and angular alignment tolerances.

Both of the above design constraints were met by the design approach developed on PALS. The basic scheme was to use a primary with a conic constant near zero, to make it possible to maintain the same primary/

secondary optical alignment as the pointing angle changed. A modification of this approach was also developed, in which a single secondary mirror replaces earlier approaches which required separate secondaries for low and high power beams (Figure 2-4).

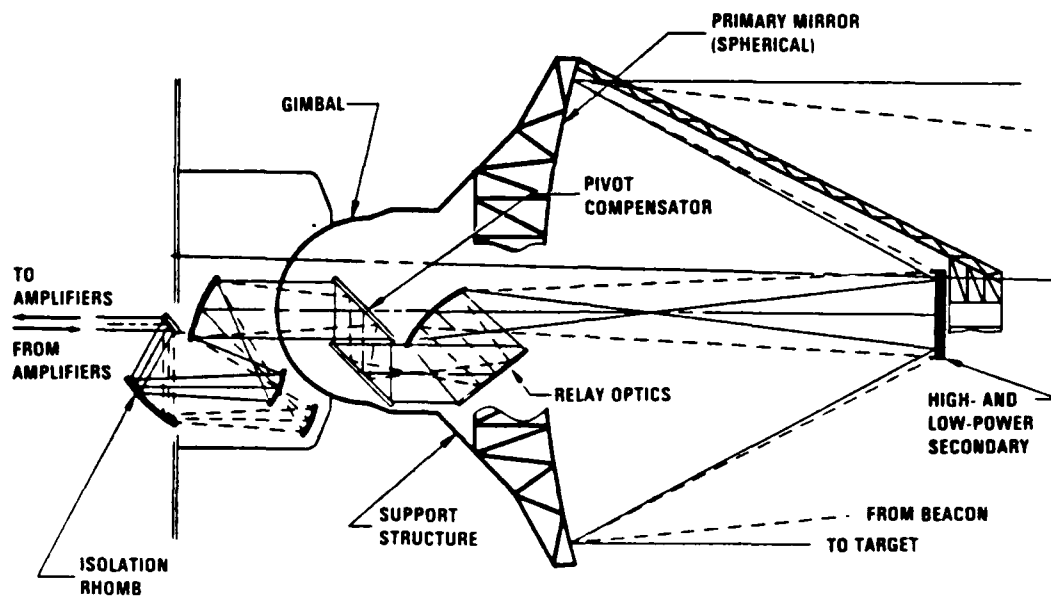


Figure 2-4. Beam director concept showing secondary and relay optics.

3. MISSION REQUIREMENTS, GUIDELINES, AND MISSION ANALYSIS

3.1 STARTING POINT

In order to determine the kind of mission for which PALS is to be used, existing space-based laser programs were examined to provide a technical starting point for the PALS program. One was chosen that seemed representative of most such programs, namely the Lockheed Space-Based Laser (SBL) program. That program was examining the design issues associated with a high brightness HF laser much like the proposed PALS design.

The SBL program made use of a technical guideline document (Ref. 3.1) and the decision was made to use this document for the PALS program also. This document specifies an SBL mission in terms of 1-on-P performance guidelines, which detail number and type of RVs and launch vehicles killed, and gives a range histogram for the M-on-N target scenario, complete with trajectories, launch, and target coordinate information. Also included are target vulnerability parameters for the specified launch vehicles and RVs, given in terms of minimum intensity and fluence requirements, and damage spot size requirements.

Under phase IIA and IIB of this program Lockheed performed a detailed mission analysis of the specific threat, and determined a minimum overall system brightness level required to perform the mission. Although this is likely to be a constantly evolving requirement, continually subject to change as program requirements become better defined, their value was taken as an initial design point for this important parameter.

The definition for overall brightness is based on the Air Force version of the equation and is shown below.

$$\text{Brightness} = \frac{PA (1 - \epsilon^2) \exp-(2\pi\phi)^2}{\lambda^2 \rho^2 \left[1 + \frac{\sigma_j^2}{(0.431 \lambda/D)^2 f(\epsilon)} \right]} \quad (3-1)$$

3.1 "Space-Based Laser Phase II (U)," USAF, February 19, 1985.

where

- P is system output power
- ϵ is beam obscuration
- ϕ is phase error induced by the beam director
- λ is wavelength
- σ_j is jitter beam spread, usually expressed in terms of λ/D
- A is aperture area
- $f(\epsilon)$ is correction in beam spread due to obscuration and is equal to $1/(1 + 1.7 \epsilon^{1.8})$
- σ_D is diffractive beam spread = $0.431 \lambda/D$
- D is primary aperture diameter
- β is output beam quality assuming a perfect beam director

It is important to note that most of the key system parameters appear in this equation. Therefore, if one parameter is changed, the equation dictates what other parameter(s) must be changed, and by how much, in order to keep overall brightness constant. The effect of some of these parameters will be shown later in this section.

3.2 MISSION REQUIREMENTS

The mission requirements are listed in Table 3-1. Most are classified and can be found in Reference 2.1.

TABLE 3-1. PALS Mission Requirements.

1. Minimum damage spot diameter
2. Minimum edge fluence requirement
3. Minimum edge intensity requirement
4. Minimum overall system brightness
5. Total firing time capability
6. Maximum target engagement time
7. Maximum time delay to reach battle-ready condition
8. Maximum time delay for laser beam initiation
9. Minimum time between refuelings
10. Shut-off, restart capability
11. Acquisition, pointing, tracking system compatibility

The mission derived guidelines are presented in Table 3-2. Most of these are internally generated system parameters which are intended to guide the design, and may be changed more frequently than the requirements, if this becomes necessary.

TABLE 3-2. PALS Mission Derived Guidelines.

- | | |
|-----|---|
| 1. | Minimum system output power |
| 2. | Primary mirror diameter |
| 3. | Maximum overall system jitter |
| 4. | Maximum allowable beam director large angle slew acceleration |
| 5. | Minimum beam director large slew angle capability |
| 6. | Minimum retargeting time within a target field |
| 7. | System beam quality assuming a perfect beam director, stated as a range between a minimum and maximum value |
| 8. | Beam director wavefront error |
| 9. | Weight and volume optimization as system consideration |
| 10. | Design for operational and nonoperational conditions |
| 11. | Minimum overall lifetime |
| 12. | Survivability in specified battle conditions |
| 13. | Simplicity and reduced complexity |

3.3 MISSION ANALYSIS

In order to determine the effect of the major terms in the brightness equation, Equation (3-1) is rewritten as follows:

$$\text{Brightness} = \frac{PA(1-\epsilon^2)}{\lambda^2} \cdot \exp-(2\pi\phi)^2 \cdot \frac{1}{\beta^2} \cdot \frac{1}{1 + \frac{\sigma_j^2}{(.431 \lambda/D)^2 f(\epsilon)}}$$

It is of interest to determine the effect of the three coefficients of the PA/λ^2 term. This is shown in Figure 3-1. In order to keep the overall brightness greater than the required value, the product of the three coefficients must be greater than 0.61. That is a decrease in one factor must be compensated by an increase in one or both of the other terms.

The above values are for optimum range conditions. At ranges greater than the optimum, the intensity in the damage spot decreases with increasing range due to diffractive effects. Figure 3-2 shows this effect for peak, average, and edge intensities over the ranges of interest. All values have been normalized. Note that at ranges less than the optimum range the intensities remain constant, due to the defocus of the beam necessary to provide the required intensity at the edge of the specified damage spot (otherwise the spot would be smaller than the required damage spot size). An alternate method for accomplishing this is to scan the beam around the edge of the spot, however, this results in a decrease in intensity in the center of the spot, which might be undesirable.

When examining the two vulnerability requirements, edge intensity and fluence, it is useful to determine which one has the *dominant effect* as ranges are increased. The answer is that the edge fluence is the more stringent of the two, and the target dwell time must be increased to keep the edge fluence at or above the minimum required level. Figure 3-3 shows the effect on target dwell time over the ranges of interest. All values have been normalized.

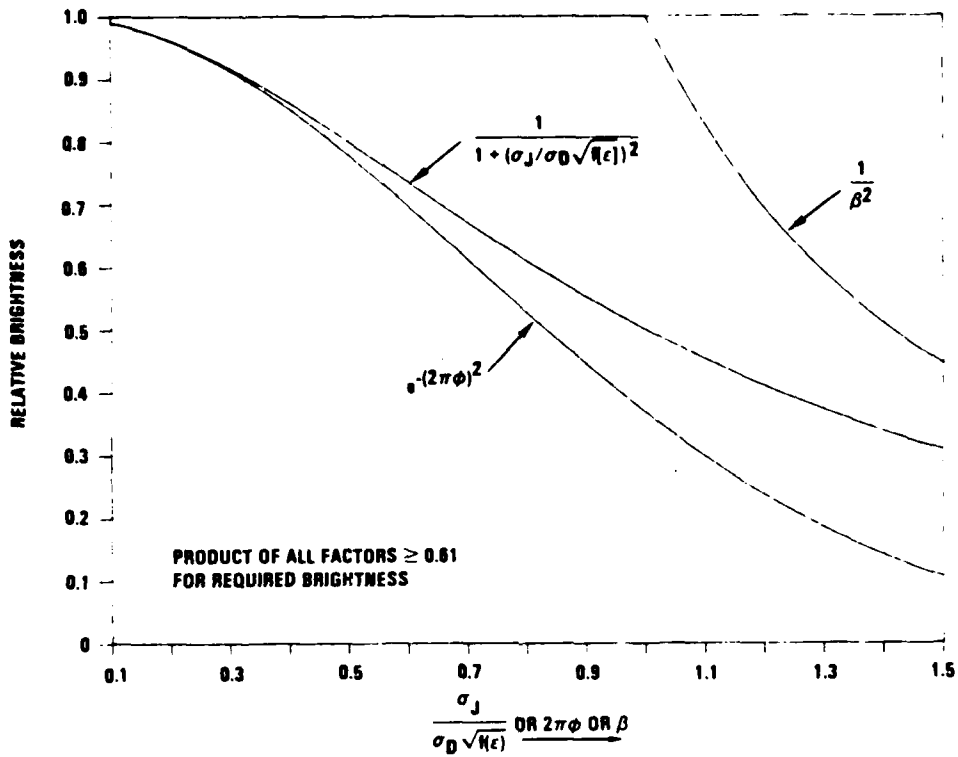


Figure 3-1. Relative brightness affected by jitter WFE, BQ, and OBSC.

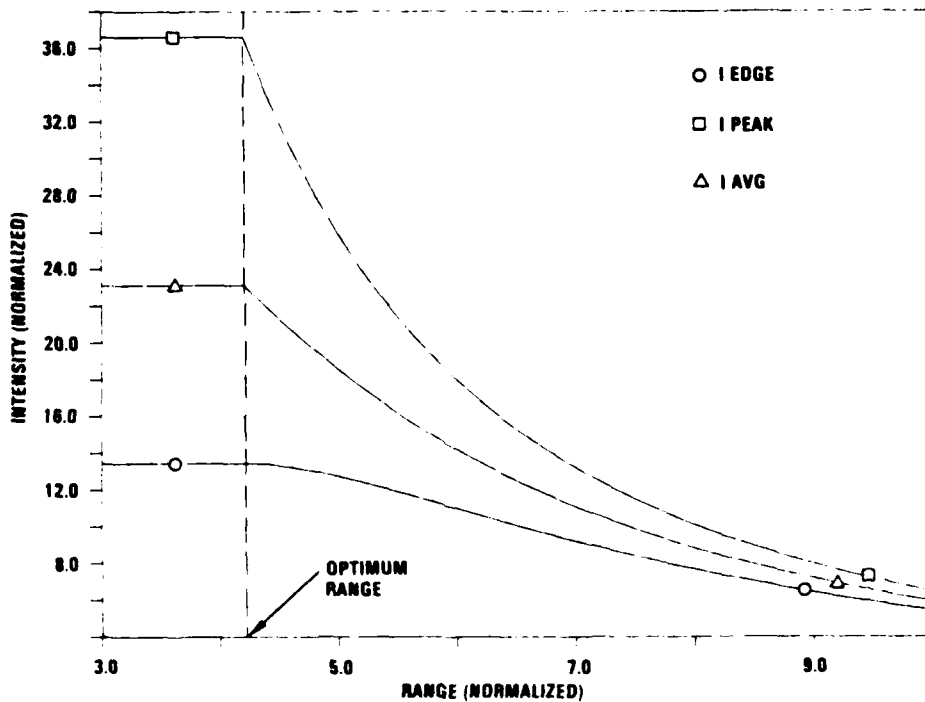


Figure 3-2. Intensities at several ranges for PALS SBL mission.

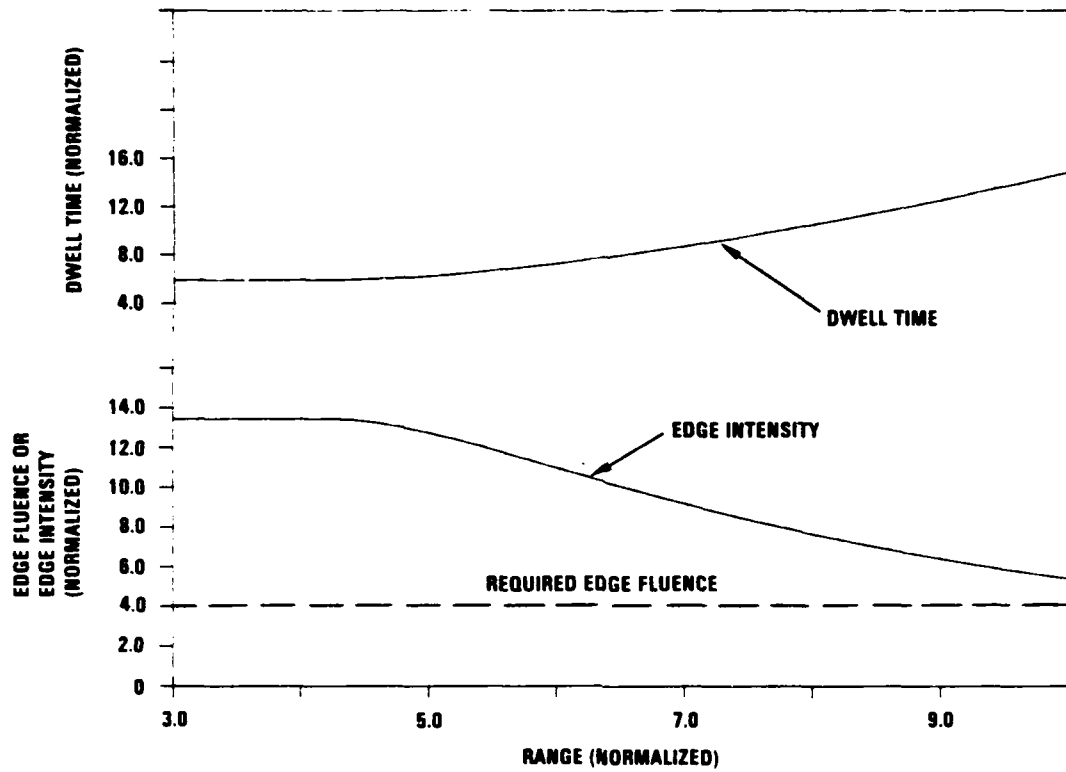


Figure 3-3. Edge intensity and dwell time for PALS SBL mission.

4. PALS SUBSYSTEM OVERVIEW

4.1 FUNCTIONAL DESCRIPTION

The Phased Array Laser System (PALS) preliminary configuration has been chosen to satisfy the mission requirements and guidelines (classified), as well as the system and subsystem requirements listed in the PALS project requirements document (PRD). The preliminary configuration has been divided into four subsystems and nine assemblies listed below:

1. Master Oscillator Subsystem

- Oscillator assembly
- Oscillator output optical train assembly

2. Power Amplifier Subsystem

- Amplifier assembly
- Beam separation and recombination assembly
- Amplifier optical train assembly

3. Beam Director Subsystem

- Beam director assembly
- Beacon assembly

4. Phase-Conjugation Subsystem

- Conjugation optical train assembly
- Conjugation assembly

These subsystems are shown schematically in Figure 4-1, and functionally in Figure 4-2. In this configuration the beam begins at the oscillator subsystem at the left of Figure 4-1 and is directed to the free-flying beacon mirror which is off the right side of the page at a distance of approximately 20 times the primary mirror diameter away from the primary mirror. The beam is then directed back towards the primary mirror, diverging to fill the entire aperture.

The low power, near diffraction-limited beam is then directed towards the secondary mirror which sends it towards the amplifiers via the beam director pointing optics and amplifier separation and recombination optics. The smaller beams are directed to the individual amplifiers, where they are amplified and directed to the phase-conjugation subsystem.

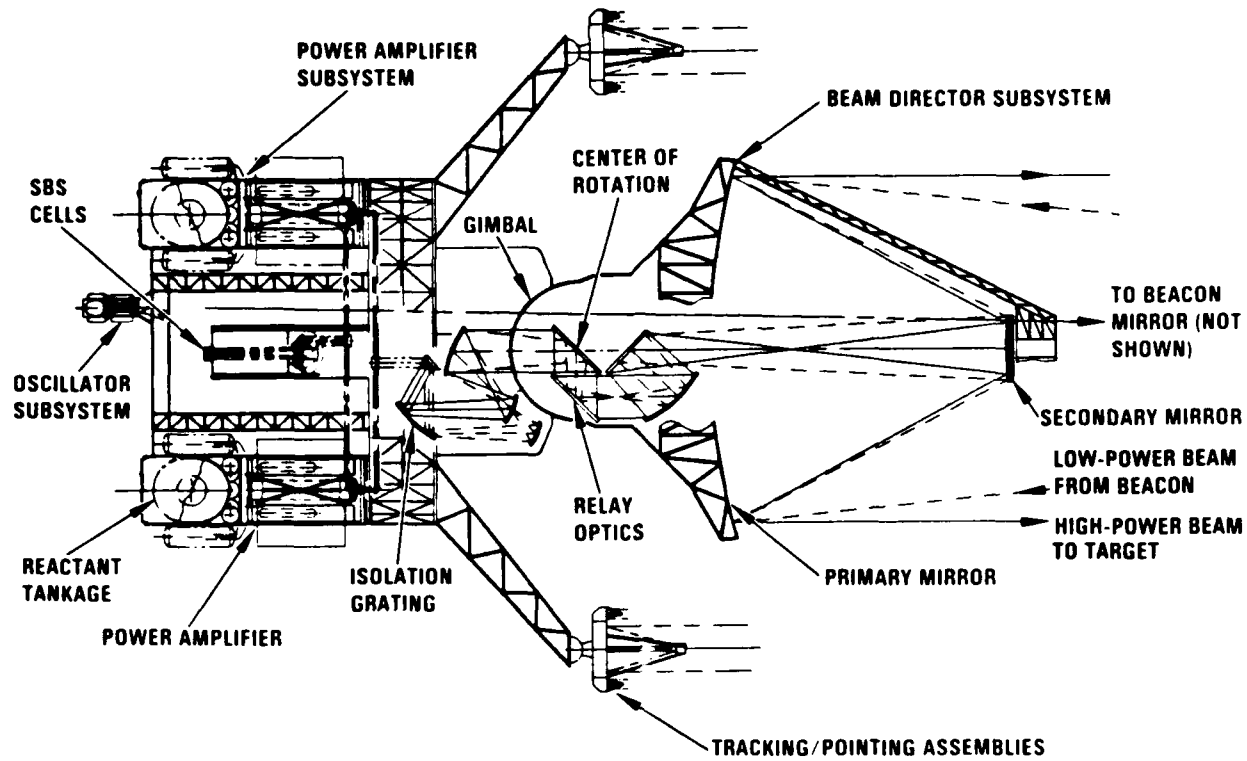
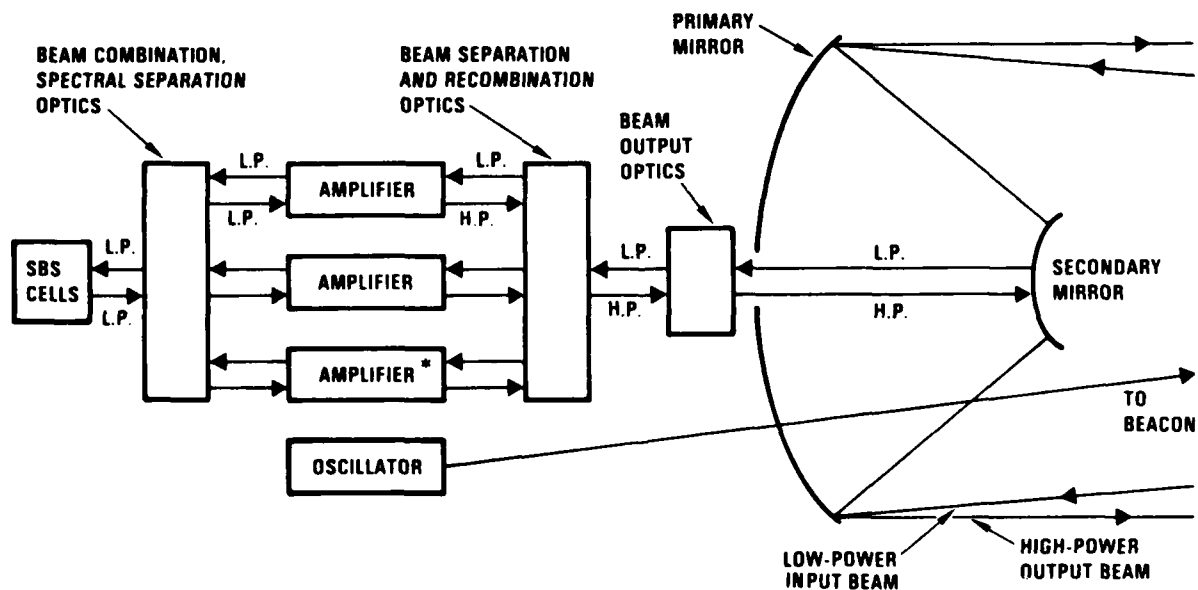


Figure 4-1. Phased array laser system (PALS) concept.



*ADDITIONAL AMPLIFIERS NOT SHOWN

Figure 4-2. PALS functional configuration.

The phase-conjugation optical train spectrally separates the beams into separate lines and directs them to the SBS cells. A conjugate beam is reflected back from the cells and propagates back along the input beam path. It is spectrally recombined and sent to the amplifiers for amplification to maximum power.

The high-power beam is then directed towards the beam director pointing optics after passing through the isolation grating rhomb which spatially separates the high- and low-power beams due to their different polarizations. The high-power beam is then directed to the secondary and primary mirrors from which it is propagated to the target.

4.2 SUBSYSTEM DESCRIPTION

4.2.1 Oscillator Subsystem

The primary function of the oscillator subsystem is to provide a very good beam quality, linearly polarized low-power reference beam to the amplifiers (via the beacon and primary mirror).

This is accomplished by using a small HF laser with a cylindrical gain generator much like the larger amplifier design. The oscillator beam must be spectrally matched to the power amplifiers to provide good extraction efficiency and to limit to four the number of lines on which the major portion of the output power is contained. It also must start with sufficient power to propagate the relatively long distance to the beacon mirror and still provide the required input power to the amplifiers.

The oscillator optical train will include optics to remove high frequency jitter from the beam and direct it to the beacon within the allowable pointing requirements. An enlargement of the oscillator subsystem is shown in Figure 4-3.

4.2.2 Power Amplifier Subsystem

The primary function of the power amplifier subsystem is to receive the oscillator beam, amplify it bidirectionally, and delivery the high power beam to the beam director.

This is accomplished by using seven scaled-up ALPHA II type amplifiers arranged in a parallel configuration with the exhaust gases directed

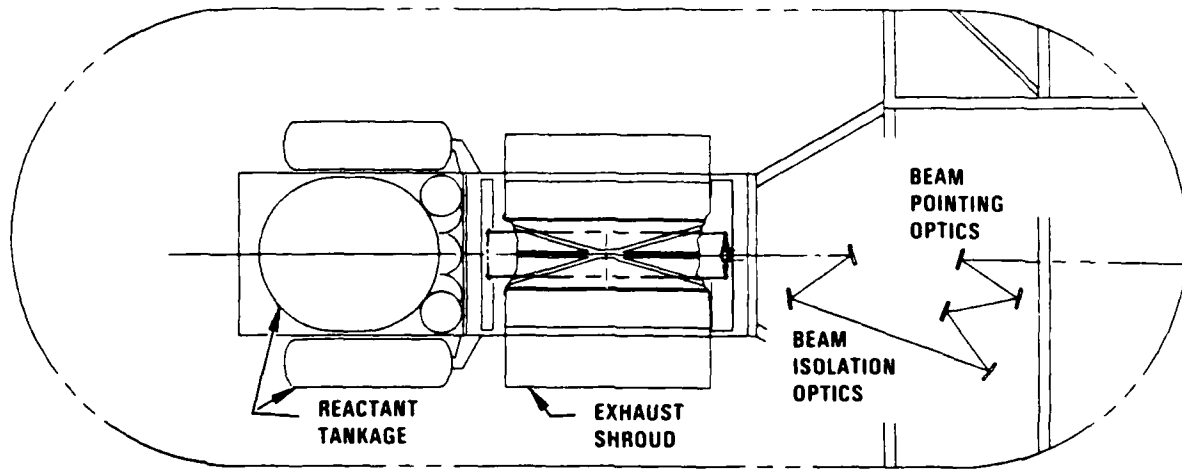


Figure 4-3. Cylindrical oscillator.

radially outward to avoid contamination of optics or absorption of the beam. The amplifiers are operated bidirectionally in order to phase conjugate most of the gain generator aberrations. Beam separation and recombination optics are provided to direct the beam to and from the amplifiers, with coarse correction of low-power beam alignment errors. An isolation grating rhomb is used to spatially separate the high- and low-power beams due to the difference in polarization caused by the quarter-wave coating in the phase conjugation subsystem. An enlargement of the power amplifier subsystem is shown in Figure 4-4.

4.2.3 Beam Director Subsystem

The primary function of the beam director subsystem is to receive the low-power oscillator beam and direct it to the amplifiers, then receive the amplified high-power beam and direct it to the target, with the necessary pointing accuracy.

This is accomplished using a primary, secondary, tertiary, and relay mirrors, as well as a free-flying lightweight beacon mirror to relay the low power oscillator beam to the amplifiers. The primary mirror is spherical, gimballed, multisegmented (with identical segments), and has piston and jitter errors corrected by the phase-conjugation subsystem. A single secondary is used for both the high- and low-power beams since this minimizes obscuration and enables the secondary to be conjugated. Small angle

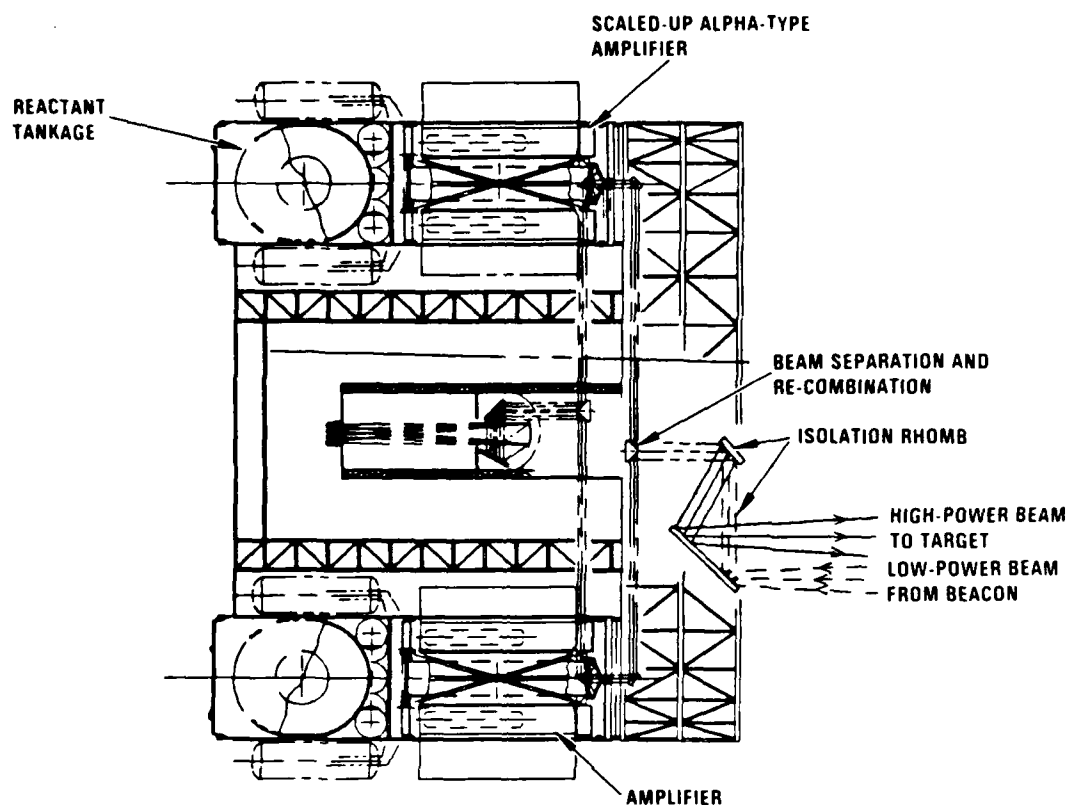


Figure 4-4. Power amplifier subsystem.

pointing is accomplished by small rotations and translations of the secondary and tertiary mirrors, which are part of a concentric (zero-field) design that eliminates off-axis pointing aberrations. An enlargement of the beam director subsystem is shown in Figures 4-5a and 4-5b and a functional block diagram is shown in Figure 4-6.

4.2.4 Phase-Conjugation Subsystem

The primary function of the phase-conjugation subsystem is to accept the partially amplified beam from the amplifiers, and reflect a phase-conjugated beam back through the amplifiers.

This is accomplished by using a flowing SBS cell concept similar in design to the cell to be used in the COS experiment of the CLPCT program. This cell utilizes xenon at 40 atmospheres pressure and 300 K, which is filtered, purified and flowed transversely across the beam at between 20 and 80 m/s. Two helium aerowindows, one each at the entrance and exit apertures, are used to confine the xenon within the SBS cell at the correct pressure, with minimum beam distortion. Individual SBS cells are used for

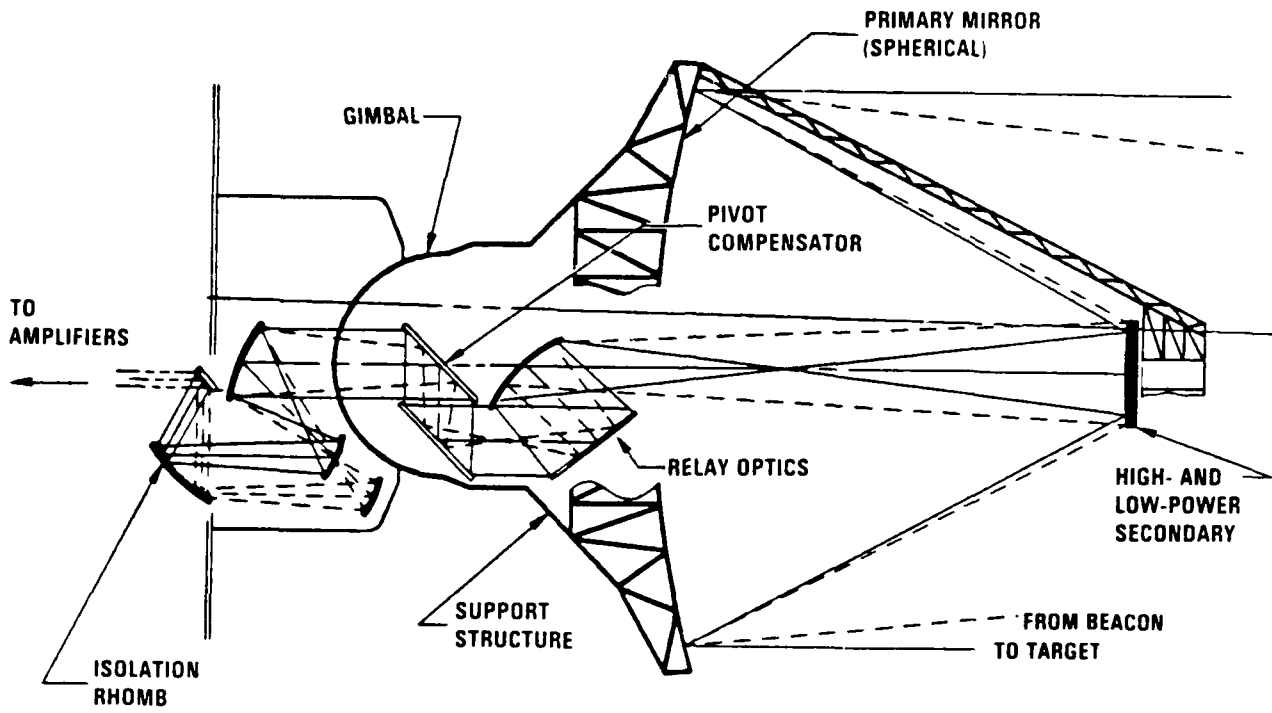


Figure 4-5a. Beam director concept showing secondary and relay optics.

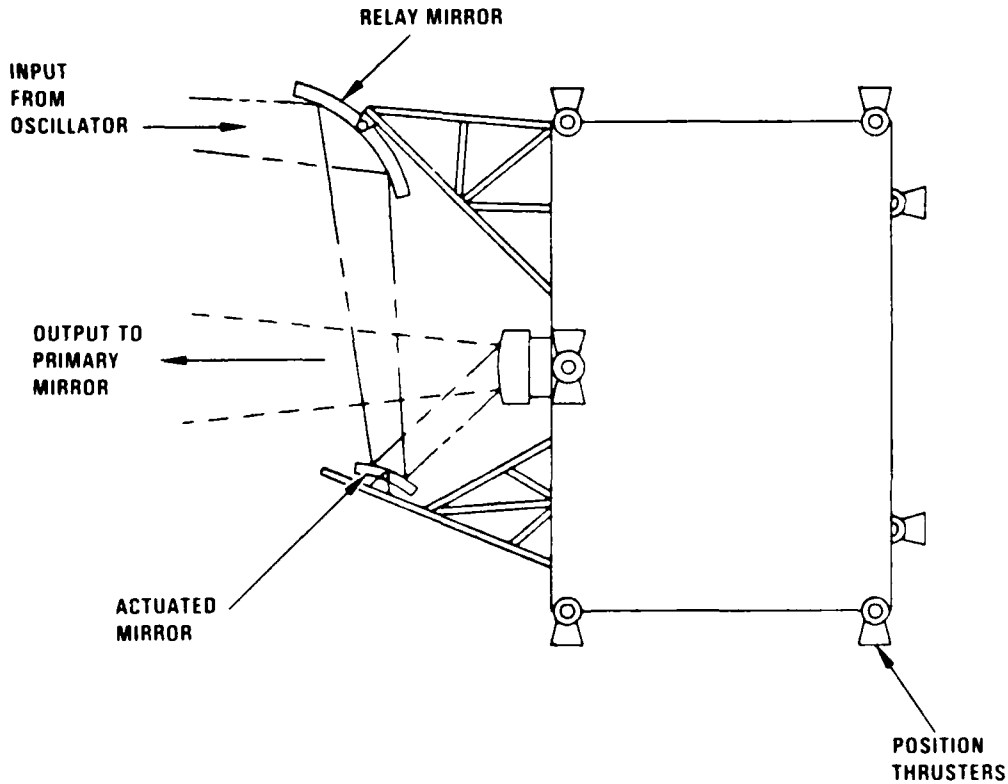


Figure 4-5b. Free-flying beacon mirror--relays oscillator beam to primary mirror.

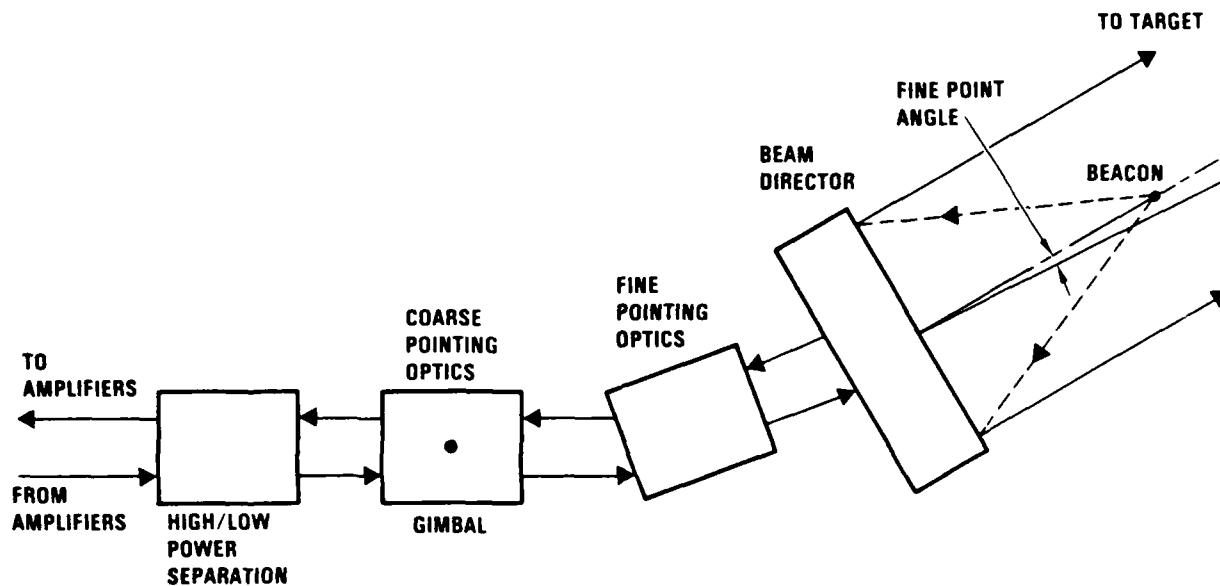


Figure 4-6. Functional diagram of beam director subsystem.

each spectral line, since it will probably be simpler to construct several small cells than one large one, and also to prevent the focal regions from disturbing each other. Note that the focal volume of each cell contains the combined energy from all the amplifiers contained on a single line. An enlargement of the SBS cell configuration showing four side-by-side cells is shown in Figure 4-7.

4.3 PRELIMINARY POWER BUDGET

Table 4-1 is a preliminary power budget used to determine the oscillator power required to supply the output power specified in reference 4.1. Best possible estimates were used for mirror reflectivities and grating efficiencies, and propagation loss to the beacon was based on an initial beam quality of 1.2 and a bucket size of $Q = 0.8$. Amplifier gain was taken as the ratio of the output power to the power reflected from the SBS cell, which is also equal to the ratio of the SBS input power to the input power supplied by the oscillator. Both were calculated for ideal cases assuming no losses in the system.

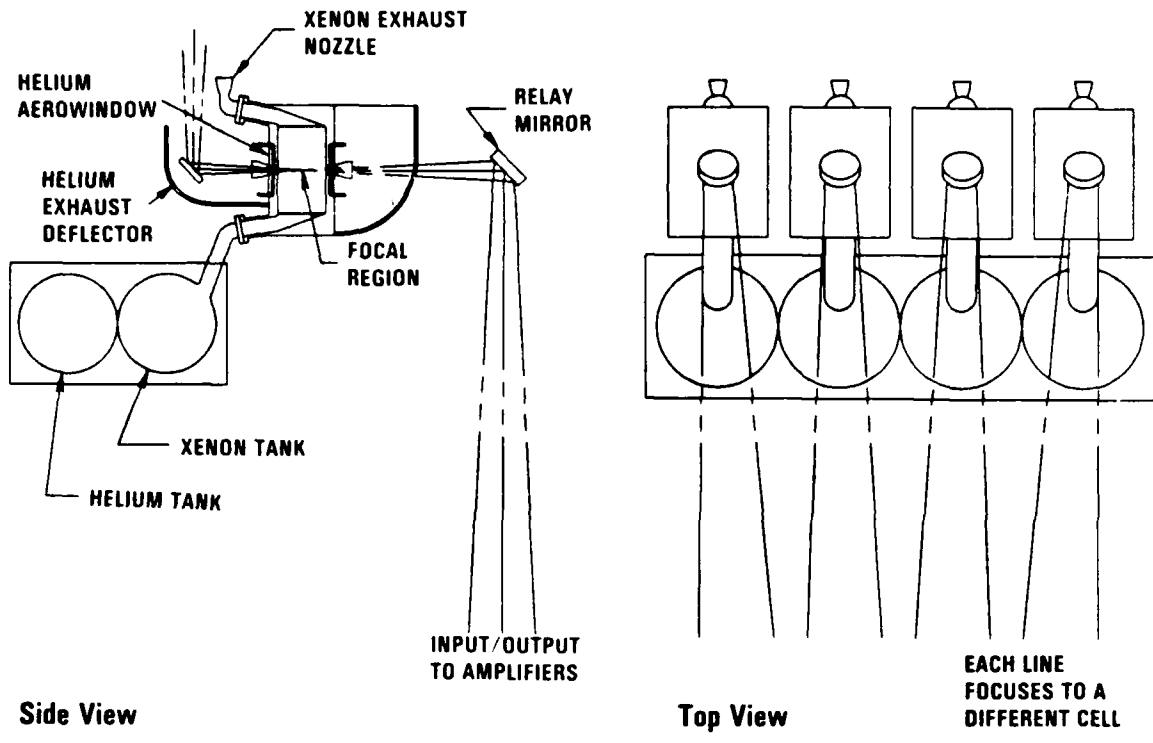


Figure 4-7. Transverse flowing SBS cell concept.

TABLE 4-1. Preliminary PALS power Budget.

| | Component | Transmission | Normalized Power |
|--------------|-------------------|--------------|------------------|
| Forward Pass | Oscillator | | 0.150 |
| | Isolation optic | 0.995 | 0.149 |
| | Propagation loss | 0.550 | 0.082 |
| | Beacon relay | 0.985 | 0.081 |
| | Primary | 0.995 | 0.080 |
| | Secondary | 0.995 | 0.080 |
| | Six relay optics | 0.970 | 0.078 |
| | Isolation rhomb | 0.640 | 0.050 |
| | Beam distribution | 0.995 | 0.049 |
| | Amplifier | 32.300 | 1.598 |
| | SBS grating | 0.980 | 1.566 |
| | Quarter wave | 0.970 | 1.519 |
| | Focusing mirror | 0.995 | 1.511 |
| | SBS cell | 0.680 | 1.028 |
| Return Pass | Focusing mirror | 0.995 | 1.023 |
| | Quarter wave | 0.970 | 0.992 |
| | SBS grating | 0.980 | 0.972 |
| | Amplifier | 32.300 | 31.397 |
| | Beam distribution | 0.995 | 31.240 |
| | Isolation rhomb | 0.980 | 30.615 |
| | Six relay optics | 0.970 | 29.708 |
| Secondary | 0.995 | 29.560 | |
| Primary | 0.995 | 29.412 | |

5. MOPA (MASTER OSCILLATOR AND POWER AMPLIFIER) SUBSYSTEMS

5.1 MOPA SUBSYSTEM PRELIMINARY CONCEPT AND TRADE STUDIES

The objective of this task was to develop analytical tools to optimize the MOPA configuration with respect to mission requirements and guidelines. The approach was to perform parametric studies on ALPHA-type cylindrical amplifiers to determine a preliminary design point. The parameters to be optimized include the number of amplifiers, the amplifier length, diameter, input power, output power, and power to the SBS cell. Issues to be considered include suppression of amplified spontaneous emission (ASE), and the interaction of gain saturation in the amplifier with phase conjugation, which depends on the amplifier Fresnel number and the saturation level.

Several analytical models have been used to address these issues. They include the ANOM and CLAM codes, which are one-dimensional models of CW HF resonators and amplifiers, respectively, and are anchored to the three-dimensional model of the ALPHA device (the CROQ code). Also used was the LFCM code, which is a two-dimensional model of an amplifier and includes an ASE model. These codes are described in more detail in the next section.

The preliminary configuration for the gain generator geometry was chosen to provide the required power with the minimum design risk. LFCM was used to perform a systems trade between the gain generator diameter, the gain length, and the number of amplifiers. The constraints were that the total output power must equal the PALS requirement, and that the gain generator diameter and length must be less than the structural and alignment limits set by the ALPHA program. The normalized input power was $0.1/(\text{number of amplifiers})$ kW, and the SBS reflectivity was 0.68. The results of these calculations are shown in Figure 5-1. An additional consideration in the choice of configuration is that while fewer amplifiers minimize the system complexity, a greater gain generator volume is required for each amplifier. The preliminary configuration choice is shown in Figure 5-1 and consists of seven amplifiers 9 m long and 2.7 m in diameter. The arrangement of these seven amplifiers is shown in section view in Figure 5-2 and in lateral view in Figure 5-3.

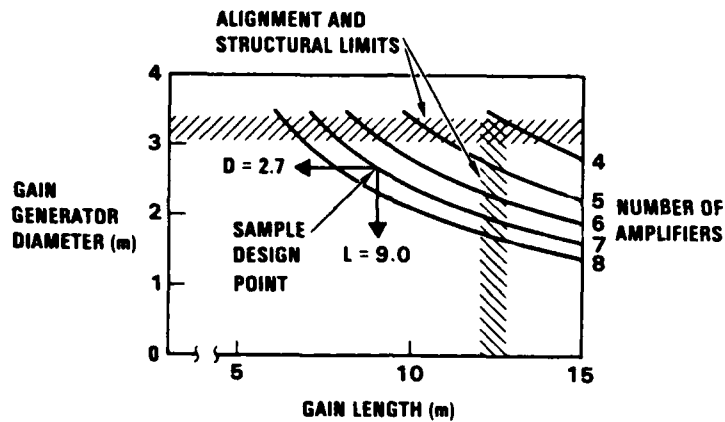


Figure 5-1. Gain generator geometry chosen to provide required power with minimum design risk.

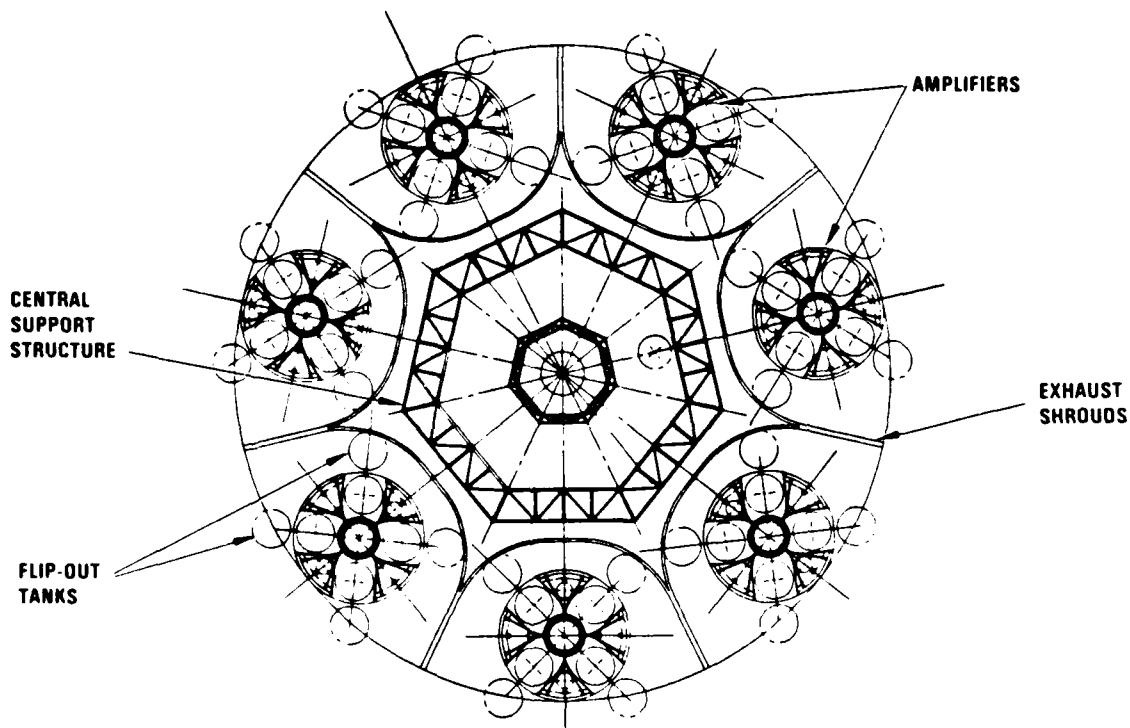
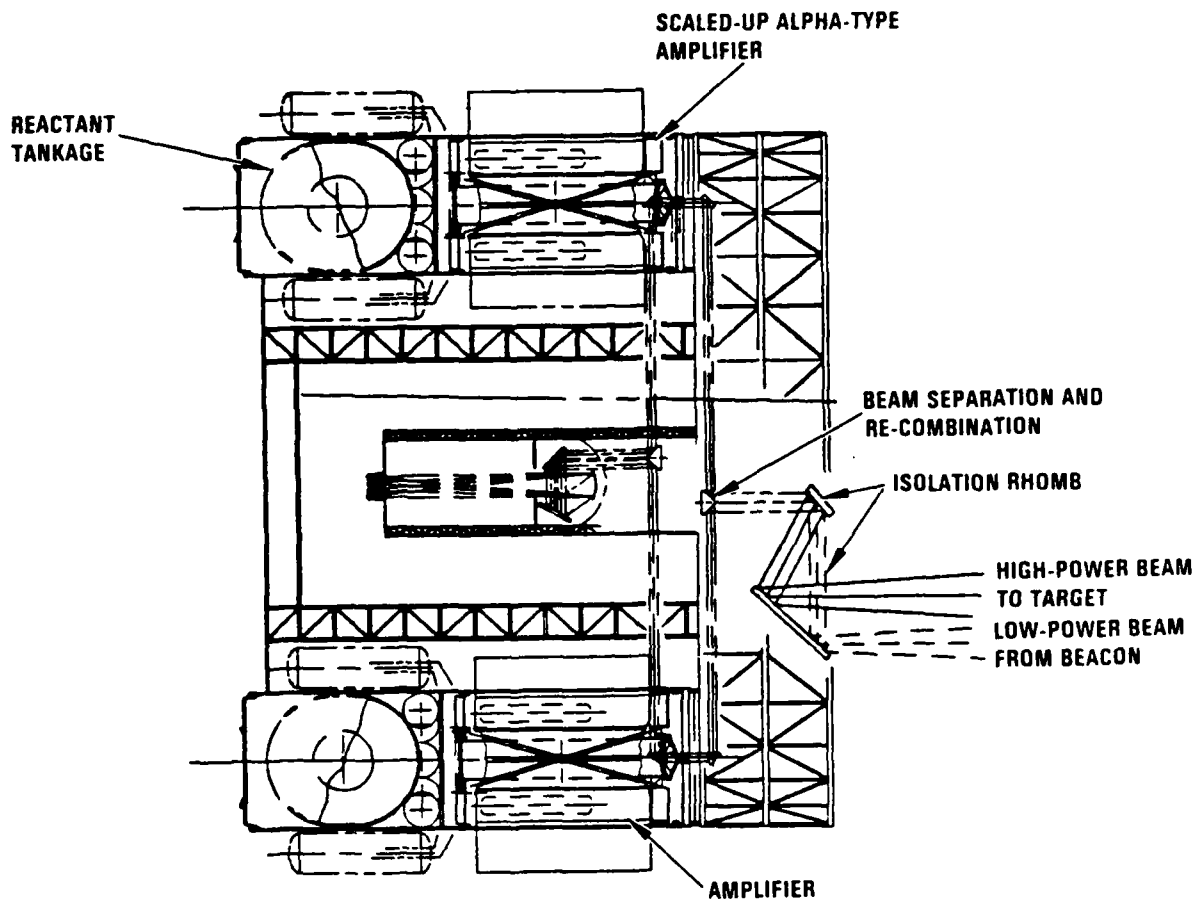
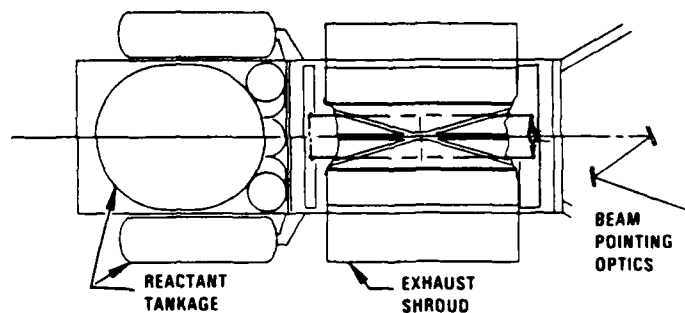


Figure 5-2. Section view of PALS amplifier assembly.



a. Amplifier Concept

- o Seven bidirectional amplifiers in parallel configuration
- o Sample design point 9-m long by 2.7-m wide
- o Multifaceted beam separation optics



b. Master Oscillator Concept

- o Small cylindrical laser
- o Spectrally matched with amplifiers
- o Pointing capability for beacon

Figure 5-3. MOPA subsystem concepts.

More detailed analyses on components of the MOPA subsystem are described in the following sections. These include the MOPA extraction efficiency and beam quality and beam separation issues such as design of the grating rhomb and the quarter-wave retardation coatings.

5.2 MOPA EXTRACTION EFFICIENCY AND BEAM QUALITY*

The overall objective of the MOPA analysis task was to develop the analytical tools needed to define the MOPA configuration. In particular, these tools will be used to define the conceptual changes to modify the ALPHA resonator design to an amplifier design. The analytical models developed are intended to address the following issues:

- Master oscillator power and bandwidth required to provide optimum extraction efficiency, good beam quality, amplified spontaneous emission (ASE) suppression, and adequate SBS reflectivity in the power amplifier.
- Effect of the SBS frequency shift on amplifier extraction efficiency.
- Effect of amplifier gain saturation on the ability of phase conjugation to correct for aberrations.

The approach to this task was to modify one- and two-dimensional models of CW HF lasers. The ANOM and CLAM codes are one-dimensional models of a resonator and an amplifier, respectively. They both contain the ACLOS gain model, which describes the effect of both inhomogeneous and homogeneous broadening in cascade-connected transitions of a CW HF laser. This gain model is based on pumping and quenching rates anchored to a full kinetics model of the ALPHA gain medium including the effects of rotational nonequilibrium and mixing in a flowing gain medium. The ALPHA gain model has been validated by comparison with data from the ALPHA verification module on small signal and saturated gain, output and intracavity power spectra, and output intensity profiles (reference 5.1). The output of the ANOM and CLAM codes includes intensity on each longitudinal mode and saturated gain and index as a function of frequency.

5.1 SCORE Review Report (U), TRW 35980-6077-SX-00, 22 July 1983 (Secret).

*This section reports work partly done on the Coupled Amplifiers program.

The LFCM code is a two-dimensional model of an amplifier which can be used to predict amplifier beam quality as well as extraction efficiency. LFCM was originally developed for excimer systems. Under PALS it has been modified to model the ALPHA amplifier gain generator configuration and the ALPHA gain distribution in the flow coordinate. Modifications have been made to permit input of phase screens describing the medium aberrations as calculated by fluid dynamics codes. LFCM can also accept input fields from the wave optics model of the optical train which include the effects of primary mirror segment piston and tilt.

5.2.1 ALPHA Device Amplifier Models in LFCM

Three configurations have been implemented in the LFCM (large Fresnel number conjugated MOPA) amplifier code to model extraction efficiency and beam quality in the amplifier subsystem. The linear geometry is redescribed, the newly added "two-pass" geometry is explained and input parameters of interest are defined (although explanations of these parameters are also found in the comment section at the beginning of the source code and in reference 5.2).

5.2.1.1 Cavity and Gain Length Geometry

Figure 5-4 shows a schematic of an ALPHA resonator. In this ring resonator, the circulating beam enters at the waxicon, is annularized to the waxicon outer cone, expands as it travels to the rear element, becomes smaller as it goes to the reflaxicon outer cone, and is recompact; the beam then gets scraped and the feedback portion travels to the waxicon inner cone. The beam passes through the annular leg (and through the gain medium) twice.

The ALPHA resonator configuration has been modified slightly to produce a "two-pass" amplifier. The beam is assumed to be annularly symmetric, so that LFCM can be reasonably accurate even though it models only one annular slice.

LFCM models the two-pass amplifier shown in Figure 5-5, when the logical variable ALPHA2 is set to TRUE. Figure 5-5a shows LFCM's "cavity"

5.2 "Geometry Configurations for the MOPA Code," D. Copeland and C.C. Shih, TRW 83.K323-43, 1983.

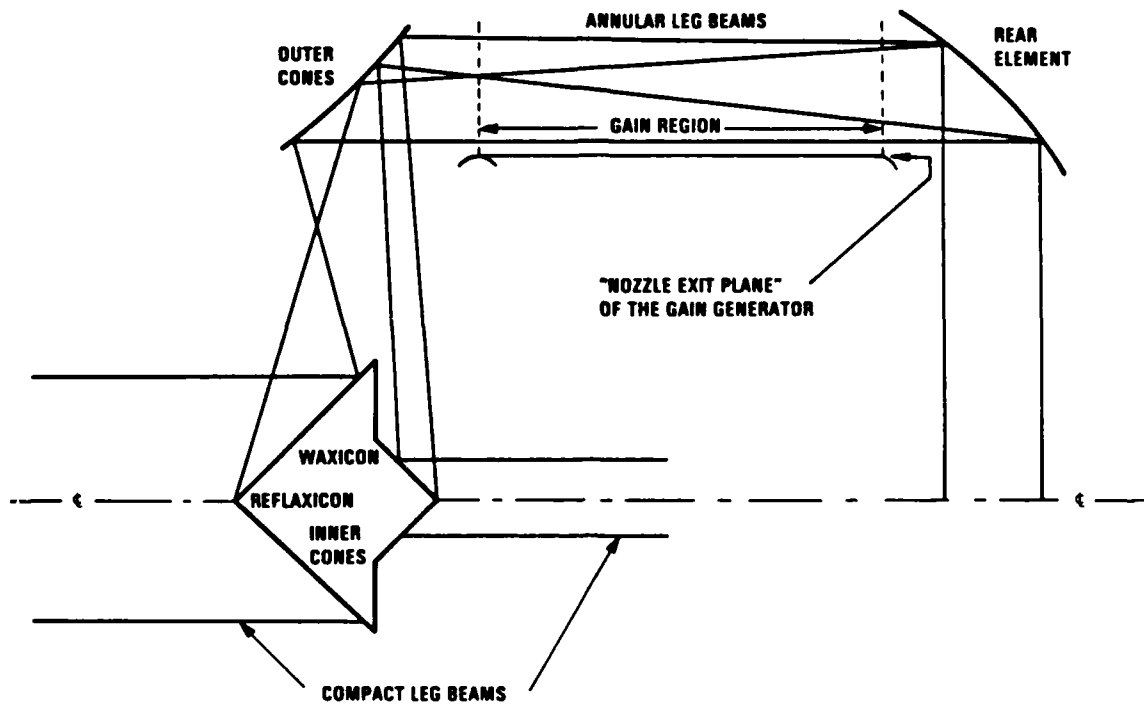


Figure 5-4. ALPHA resonator schematic diagram.

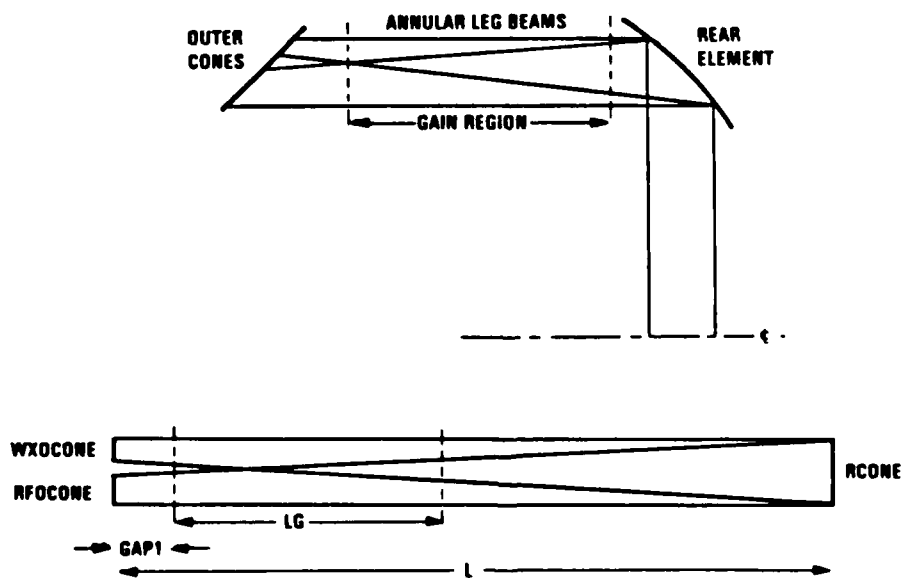


Figure 5-5a. LFCM cavity models ALPHA device annular leg.

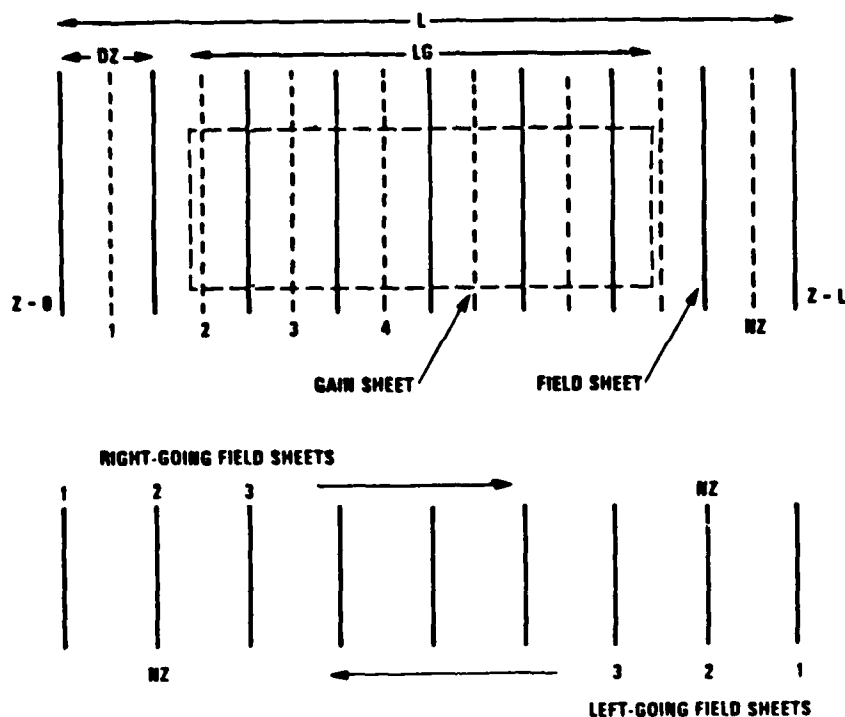


Figure 5-5b. Gain and field sheets in the LFCM code.

and relates it to the ALPHA device. Figure 5-5b shows the positions of the field and gain sheets and their numbering. The inputs to LFCM are L , the cavity length; LG , the gain length (assumed equal to L unless input); and $GAP1$, the distance from the outer cones to the beginning of the gain medium. The gain generator is assumed to be centered between the rear element and the outer cones.

If R_{GG} is the radius of the gain generator (cm), then $L = R_{GG} + 3 \text{ cm} + GAP1 + LG + GAP1$. A nominal value of 40 cm for $GAP1$ has been used in the calculations.

When the gain medium is shorter than the cavity ($LG < L$), there are some gain sheets where the gain medium does not fill the space between the field sheets or is absent altogether. In order to handle this, the code defines a gain length window function, WZ , which consists of NZ numbers, each of which is the fraction of space between corresponding field sheets filled by gain medium. (For the case illustrated in Figure 5-5b, the values of WZ would be 0, .65, 1, 1, ..., 1, .4, 0.) The gain is calculated

at each gain sheet, then multiplied by the window function, so that the appropriate amount of gain is applied to the field.

In this "two-pass" amplifier configuration, there are three options. The first, with the parameter ONEWAY true, sends the beam into one axicon, through the gain medium twice, and then out the other axicon. There is no phase conjugator or mirror. In the second and third options, with ONEWAY false, the beam is sent into one axicon, through the gain medium twice, then out the other axicon; the beam is reflected by a mirror (MIRROR true) or by a perfect phase conjugator (PERPHS true), returns twice again through the gain medium to the axicon by which it originally entered, and then is output. (With MIRROR true, the reflectivity is 100%; with PERPHS true, the amplitude reflectivity RCONJG is input.) The first and second options enable modeling of an amplifier in a system using "conventional" optics; the third, "nonlinear" optics. The first option also allows for calibration of the amplifier model by simulation of one round trip through an oscillator and then comparison of the results to those of the well-anchored oscillator models (such as BLAZER and CROQ).

The choice of whether the beam enters the annular leg at the waxicon or the reflaxicon is controlled by the parameter FORWARD. Since in the ALPHA resonator the beam enters at the waxicon, this will correspond to FORWARD true. FORWARD false will tell LFCM to have the beam enter at the reflaxicon.

In the case of a "linear" amplifier (LINEAR true), the device is as shown in Figure 5-6a. The beam enters at one axicon, a collimated beam passes through the annular leg, then the beam exits at the other axicon. The ONEWAY, MIRROR, and PERPHS options work for this configuration also, as well as for the previously used multiple-round-trip ($NRT > 1$) options.

5.2.1.2 Transverse Geometry -- Linear Amplifier

Figure 5-6b shows the geometry of the linear amplifier as seen by LFCM. WX is the total field width, including guard bands. $WX = OVERSIZ * DR$. DR is the geometric size of the right-hand mirror. The extent of the gain medium (GX) is equal to WX, unless otherwise input. DL is the size of the left-hand (beam input) mirror; it equals DR unless otherwise input. In

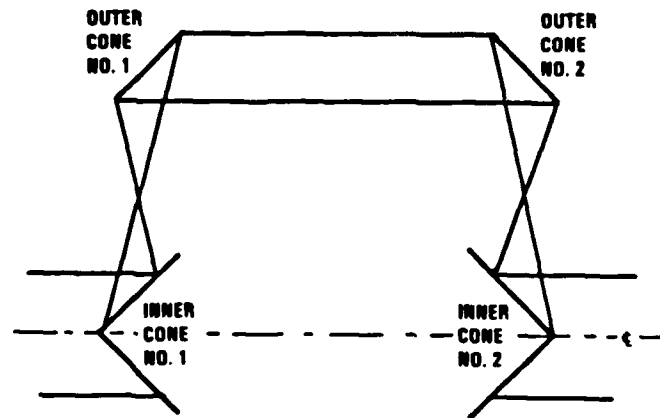


Figure 5-6a. ALPHA "one-pass" resonator schematic diagram.

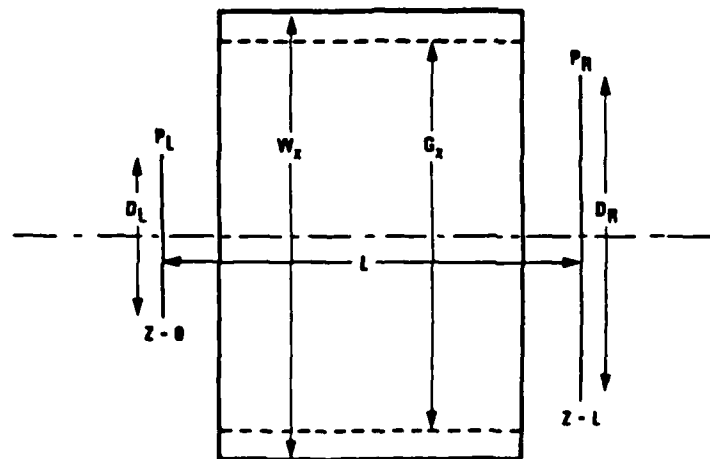


Figure 5-6b. Annular leg modeled by LFCM "linear amplifier".

LFCM, the beam always enters on the left. For this linear case, the transverse coordinate X will have the value zero in the center of the transverse direction, as shown by the dot-dash line in the figure.

There are transverse window functions which make sure the fields and the gain roll off smoothly but quickly to zero outside of their geometric apertures. These are set by calls in the code to subroutine WINDOW.

The amplified spontaneous emission (ASE) model, described in reference 5.3 by Shih, has been modified to work for ONEWAY true.

5.2.1.3 Transverse Geometry -- ALPHA "Two-Pass" Amplifier

Figures 5-7a and 5-7b show the geometry of the ALPHA device two-pass amplifier model. (FORWARD false has been assumed in the figures.) The new parameters are:

OFFSET Distance between the gain generator's nozzle exit plane and the inner geometric edge of the field. Default = 0.3 cm. LFCM's X=0 is at the nozzle exit plane (NEP).

WXOCONE Waxicon outer cone radius. Default = 1.0 cm.

RFOCONE Reflexicon outer cone radius. Default = 1.3 cm.

Other parameters are:

RCONE Rear element radius. Default = 2.6 cm.

WX Largest field size; WX is set to RCONE * OVERSIZ. (OVERSIZ must be large enough; about 1.8 is recommended.)

FX Input field size; FX is set to (WXOCONE or RFOCONE) * OVERSIZ.

GX The extent of the gain region; GX is set to RCONE + OFFSET.

5.2.2 Master Oscillator Power Requirements

Calculations performed on PALS, with support from results of the Coupled Amplifiers program, were used to set the requirements on master oscillator power. These calculations, performed with the ANOM and CLAM models, demonstrated that the power requirement at the phase conjugator could be met simultaneously with meeting a requirement that the power extracted from a bidirectional amplifier be approximately the same as that extracted from a resonator with the same size gain generator. These calculations included the effect of the SBS frequency shift (see below).

5.3 "ASE Model in MOPA Code," C.C. Shih, TRW 83.K323-69 (and 83.K326-73 for details of derivation of F) (FA in the code), 1983.

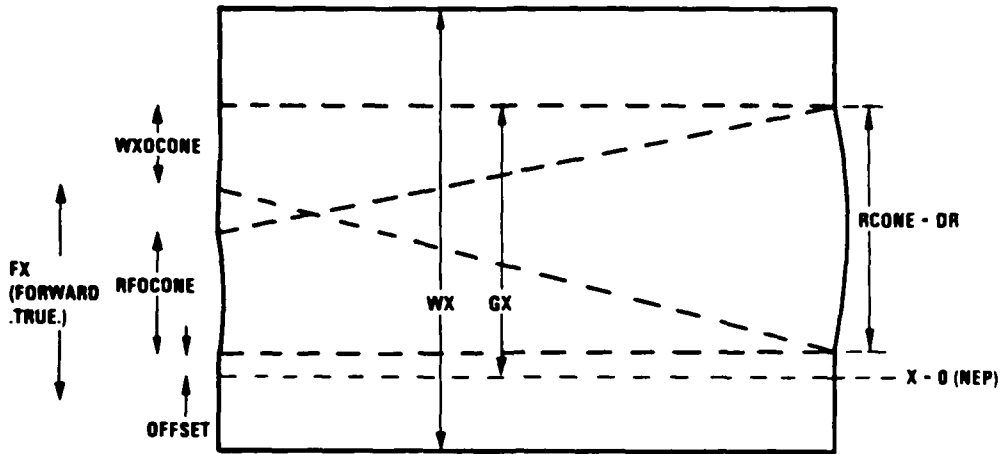


Figure 5-7a. Geometry of ALPHA2 "two-pass" amplifier in LFCM.

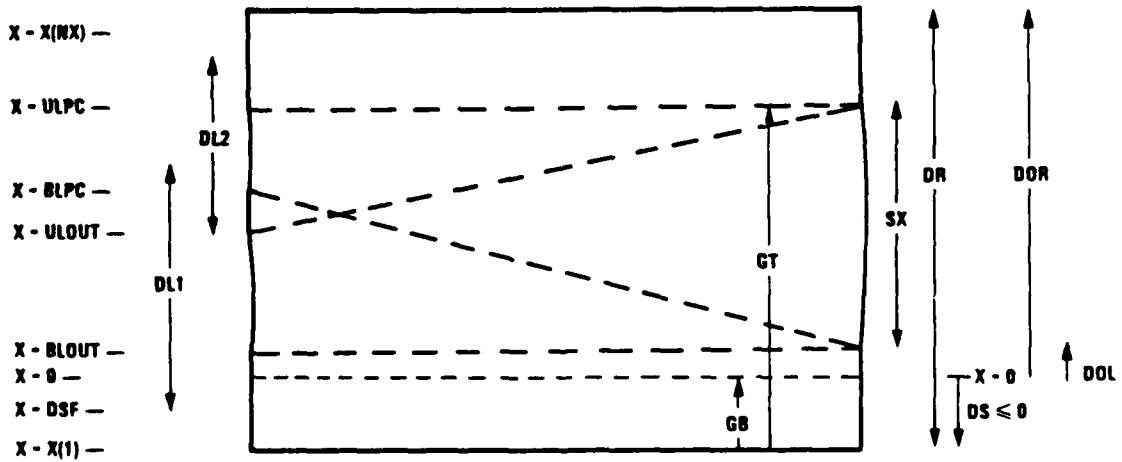


Figure 5-7b. Geometry in LFCM for ALPHA2=.TRUE. and forward =.FALSE..

5.2.3 Effect of SBS Shift on MOPA Extraction Efficiency

The objective of this task was to determine if the SBS frequency shift significantly affected bidirectional amplifier extraction efficiency caused by the offset of the return beam from the line center, and whether flowing the SBS medium along the direction of Stokes beam propagation to decrease the SBS shift would be necessary to improve the extraction efficiency. The analysis performed with the ANOM and CLAM codes demonstrates that decreasing the SBS frequency shift is not needed for xenon SBS to obtain the same extraction efficiency from a bidirectional MOPA as from a resonator.

The SBS frequency shift obtained from 40 atmospheres of xenon is 107 MHz, while the unsaturated gain has a full width at 1/e of 480 MHz (a unit Doppler width equals 240 MHz in the figures). The input to the amplifier model (CLAM code) is the output longitudinal-mode power spectrum from the resonator model for the master oscillator (ANOM code). The saturation level in the master oscillator has been adjusted so that the output bandwidth of the longitudinal mode spectrum provides optimal saturation and extraction of the gain in the power amplifier. Amplifier extraction was calculated for the case with the full SBS frequency shift (identified as shifted), and for the case where the SBS frequency shift was completely cancelled by Mach 1 flow of the SBS medium in the direction of Stokes propagation (unshifted). The output intensities for these two cases for two cascade connected lines are compared in Table 5-1. The output intensity as a function of longitudinal mode is shown in Figure 5-8, and the saturated gain is plotted in Figure 5-9. Since the oscillator can be designed to give a broad spectrum of longitudinal modes above threshold, the amplifier gain is well saturated in the wings, and parasitics and ASE should not be a problem.

5.2.4 Effect of Gain Distribution

The small signal gain distribution g_0 as a function of the flow coordinate, x , for the $P_2(7)$ line in the ALPHA device is shown in Figure 5-10.

TABLE 5-1. High-Speed Flow of SBS Xenon Medium Unnecessary.

| | Total Output (kW/cm ²) | |
|---|------------------------------------|-----------|
| | Shifted | Unshifted |
| P ₁ (8) | 6.3 | 6.7 |
| P ₂ (7) | 4.0 | 4.3 |
| SBS frequency shift | | 107 MHz |
| Unsaturated gain HW 1/e M (Unit Doppler width) | | 240 MHz |

Shifted Bidirectional Amplifier Output

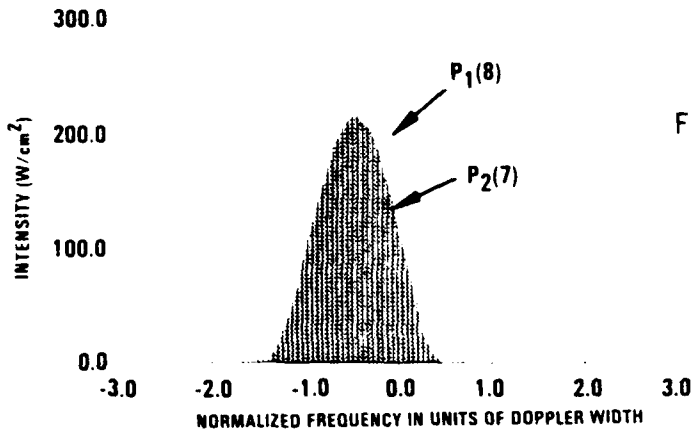


Figure 5-8 Output intensity as a function of longitudinal mode.

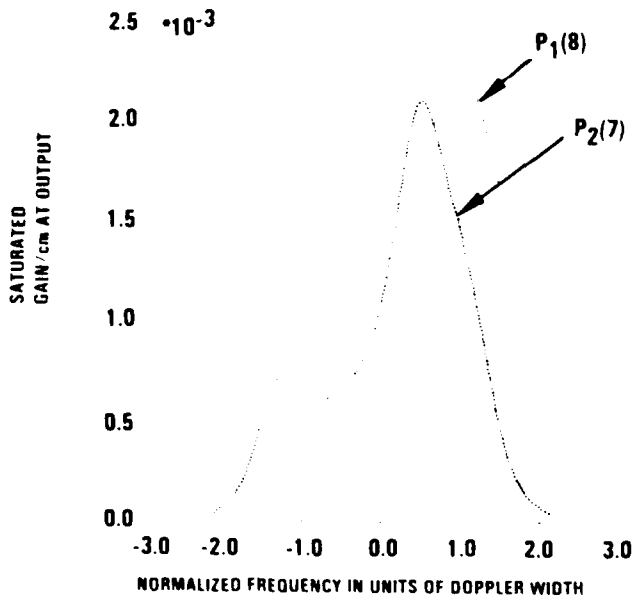


Figure 5-9. Saturated gain at output.

The zero crossing occurs at ~2.3 cm from the nozzle exit plane. In the current ALPHA design, the beam in the annular leg expands from 1.3 cm at the entrance to 2.6 cm at the rear cone with a 0.3 cm offset from the nozzle exit plane. Consequently, the gain profile significantly affects the output intensity distribution, producing the narrowed profile shown in Figure 5-11. The calculation was done for propagation through the annular leg only, assuming a uniform intensity beam as input to the annular leg. In the ALPHA amplifier configuration, the use of axicons to compact and expand the beam between the compact and annular legs produces a nonuniform intensity distribution as input to the annular leg. The appropriate choices of waxicons and/or reflaxicons and optimization of the beam widths in the annular leg should result in a reasonably uniform intensity distribution in the compact leg.

5.2.5 Interaction of Gain Saturation with Phase Conjugation

LFCM was used to determine the magnitude of the interaction between gain saturation and phase conjugation in amplifiers of 7, 9, and 11 m gain length. There was little difference in the output beam quality; all cases giving a beam quality of <1.02 . Preliminary calculations were also performed using a beam propagated through the optical train as input to the amplifier. These calculations also showed a small change in beam quality.

It is known that large phase variations that produce intensity variations in a saturable gain medium will not be completely corrected by phase conjugation. Instead of the usual plane wave input to LFCM, a field was read in containing a 180-degree phase jump, which was meant to simulate a large piston error. For high spatial resolution, 512 transverse x points were used. It was immediately found that the beam quality predicted by LFCM for the output beam was very poor, on the order of 5. The reason for this is that in the real device the output beam will go back through the source of the piston error and will be corrected, but the LFCM has no mathematical description of this. Instead, a new calculation of beam quality needs to be done when piston errors are present. The beam quality routine STREHL calculates the variance of the phase of the output beam amplitude $U_{OUT}(J)$. When piston errors are present, the same calculation is performed with the new vector $\sqrt{U_{INJ}(J) \cdot U_{OUT}(J)}$ which has the property that if U_{OUT} is the

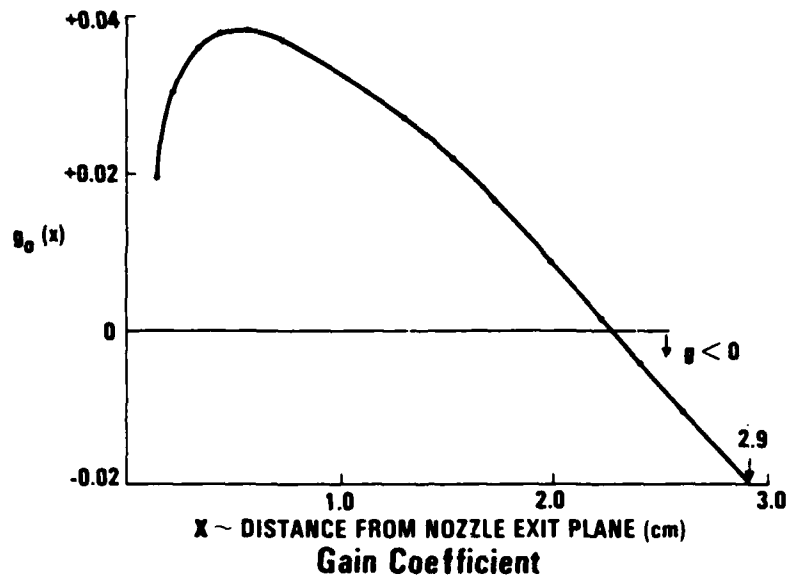


Figure 5-10. Small signal gain distribution as a function of flow coordinates.

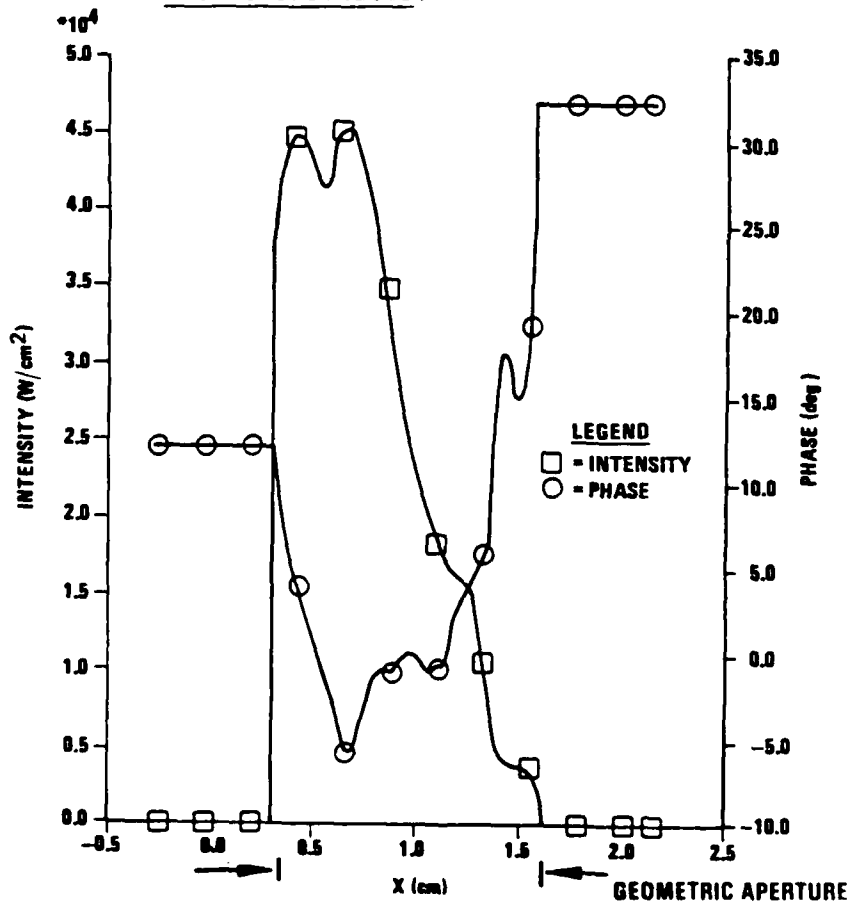


Figure 5-11. Gain profile affect on output intensity distribution.

conjugate of UINJ, the phase discontinuity is cancelled. The change works well for the simple input piston errors and can be used in the case of more realistic input beams.

Another problem with the Strehl calculation of beam quality was discovered when the new code option of a variable small signal gain was exercised. This option caused some low intensities in the output beam within the geometric aperture. A peculiarity of the phase angle calculations is that low intensities appear to yield large phase angles. These large angles lead to a large variance in phase in the Strehl calculation and, hence, poor beam quality. However, this result is unphysical, as regions of low beam intensity should obviously carry less weight than regions of high intensity. Therefore, it was decided to intensity-weight the sums used to calculate the average phase and variance in the Strehl routine. This simple process brought about a dramatic improvement in the beam quality when the small signal gain varies in space.

5.2.6 Phase Screens for the LFCM Code

In order to account for phase changes in the field propagating through a medium with an inhomogeneous index of refraction, the original LFCM code was modified to read phase screens, as input data, which may be applied at various positions in the direction of propagation. A separate screen generation code was written to accept either a numerical or functional description of the spatial variation of index of refraction. At each position at which a phase screen is required, a set of points identical to the sample points of the LFCM code is specified. Through each point the direction of the ray from the virtual source of the converging or diverging field is determined and the line integral of (index of refraction - 1.0) from the given point to the plane of the next phase screen is evaluated. This procedure is repeated for each sample point and each phase screen. Special consideration was required for ray paths which lie partially within the medium and partially outside. The calculated OPD values are then written in a format compatible with the LFCM code.

Preliminary data values for index of refraction have been provided by P. Lohn (Ref. 5.4 and 5.5), which were the result of previous flow calculations for the ALPHA configuration. The calculated index was averaged along the z direction (parallel to the axis of the cylindrical amplifier), leaving only a dependence on radial and azimuthal coordinate. Since the amplifier code models only radial variations, screens will be constructed for the two values of azimuthal coordinate which give the maximum and minimum index values. The first set of screens is being constructed.

5.2.6.1 Cavity Medium Aberrations

The preliminary PALS design concept for the amplifiers embodies the nozzle designs and configuration used for the ALPHA program. Flow-field calculations performed for ALPHA may be used to provide an estimate of the cavity medium index of refraction inhomogeneities. The results are then to be used to generate phase screens for the LFCM amplifier code in order to model the effect of the inhomogeneities on field propagation through the amplifier and on conjugation fidelity.

A report on the ALPHA calculations is given in reference 5.4. The results are summarized below.

The calculations are expressed as OPD variations attributable to each of numerous causes of density variations. If the i^{th} aberration produces an index variation of Δn_i over a distance ΔL_i in the z direction (the z axis being parallel to the axis of the cylindrical amplifier), then the OPD due to that source is, for convenience, written in the form

$$\text{OPD}_i = L (n-1) A_i$$

where

$$A_i = \frac{\Delta L_i}{L} \frac{\Delta n_i}{n-1}$$

-
- 5.4 "ALPHA OPD Map for PALS," P.D. Lohn, TRW IOC 86.K514.5-009, 12 Feb 1986.
5.5 "ALPHA I Cavity Medium Aberrations," P.D. Lohn, TRW IOC 81.4314.3-046, 28 Jul 1981.

and n is the index of refraction averaged over the length L of the device. Values of $n-1$ are shown in Figure 5-12 as a function of r , which is the radial coordinate measured outward from the nozzle exit plane. Values of A_i for a number of aberration sources are listed in Table 5-2. The nozzles are arranged in rings, with approximately 13 rings per meter of amplifier length.

The number of rings, which appear in the last column of several entries in Table 5-2, are therefore determined by the length of amplifier specified. The angle ϕ is the polar coordinate in cylindrical geometry. From Figure 5-12 and Table 5-2 and assuming a radial beam width of 2-3 cm and a gain length of 9 meters, an OPD difference across the beam of $\sim 10^{-3} \lambda$ is estimated for a complete trip through the amplifier, with a maximum OPD of about twice this amount for rays at different azimuthal positions. A potentially much larger OPD variation may arise from the ALPHA nozzle base purge blockage, discussed in reference 5.6. This contribution to the amplifier medium aberrations, and the manner in which it may be incorporated into the amplifier model, will be examined in detail in the next phase of the program.

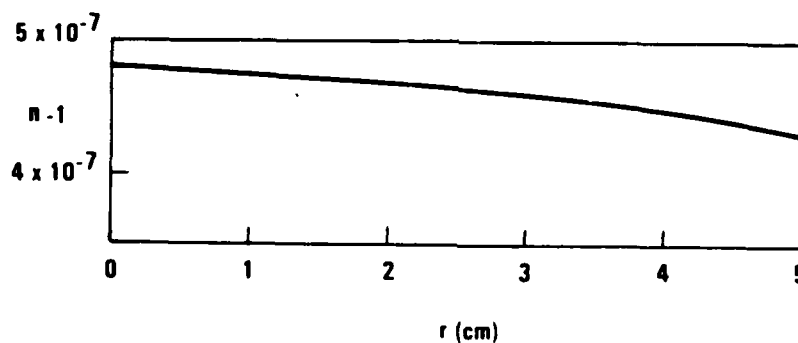


Figure 5-12. Average cavity index of refraction.

5.6 "Base Purge Blockage OPD," G.M. Harpole, TRW IOC 85.K514.3-041, 28 Jun 1985.

TABLE 5-2. GGA Cavity Medium Aberrations.

| Source | Disturbance | Symmetry or Correlation | Frequency (Hz) | Magnitude $(\Delta n/n-1)\Delta L/L^*$ |
|--|--------------------------------------|------------------------------|----------------|--|
| Primary nozzle throat size variations due to manufacturing tolerances | Azimuthal mass flow non-uniformities | Uncorrelated | 0 | $0.013 \cos 4\phi$ $\sqrt{\#rings}$ |
| Primary nozzle throat size and composition variations: thermally induced | Azimuthal mass flow non-uniformities | Correlated | 0 | $1/2 (0.00136) \cos 2\phi$ and $1/2 (0.00327) \cos 4\phi$ |
| Combustor noise based on (VAMP results) | Turbulence | | 4-400 | <0.005 (rms) |
| Combustor acoustic oscillation based on (VAMP results) | Natural acoustic modes | | | <0.005 (rms) |
| Secondary blade injection angle tolerance | | Period 1/6-inch uncorrelated | 0 | 0.01 (rms) $\sqrt{\#rings}$ |
| Secondary blade blade-to-blade fuel flow variation | | Period 1/6-inch uncorrelated | 0 | 0.01 (rms) $\sqrt{\#rings}$ |
| Secondary blade flow variation within blade | | Period 1/6-inch uncorrelated | 0 | 0.007 (rms) $\sqrt{\#rings}$ |
| Cavity isolation system | Shear layers | | | 4×10^{-3} P-V |

*L = 2 meters.

5.2.6.2 Phase Screen Calculations for Propagation in Amplifier

Electromagnetic wave propagation in weakly diffracting media may be approximated by employing the concept of geometric phase screens. This section describes the computer code that was developed to implement this concept. Four or more screens are typically used in the LFCM context for amplifier calculations.

5.2.6.3 Description of Phase Screen Geometry Used for Calculations

The wave(s) are assumed to emanate from an apparent source located at (X_S, Z_S) . The medium is contained within the boundaries delimited by (X_{MIN}, Z_{MIN}) , (X_{MIN}, Z_{MAX}) , (X_{MAX}, Z_{MIN}) , and (X_{MAX}, Z_{MAX}) (Figure 5-13).

The points labeled by a square (\square) are locations whose coordinates and values of refractive index are known. Only four phase screens are used in this example. The phase screens are to be located at the values of Z coordinates specified by $SCRNZS(1)$, $SCRNZS(2)$, $SCRNZS(3)$, and $SCRNZS(4)$. Note that a phase screen may be located outside the medium. The values of the x -coordinate for which the phase coefficients are to be computed are shown as dark circles (\bullet). The line PD joining the source point (X_S, Z_S) with a point on the phase screen is the ray for which the phase coefficient is sought. The values of the coefficients obtained can then be used to propagate the field to the next phase screen [$SCRNZS(2)$ in this case] and the procedure repeated to calculate the phase coefficients for propagation from this location to the next phase screen at the next position. The set of values of the x -coordinate is the same for all screen positions. Note that the rays may come from apparent sources at various locations, such as rays QA and RB . The location of the source (X_S, Z_S) may be anywhere outside the medium.

The propagation of waves from one phase screen position to a phase screen at another position may engender several cases. These are illustrated in Figure 5-14a-c. In each case the medium is denoted in simplified form by the rectangle and S indicates the screen phase position in the system.

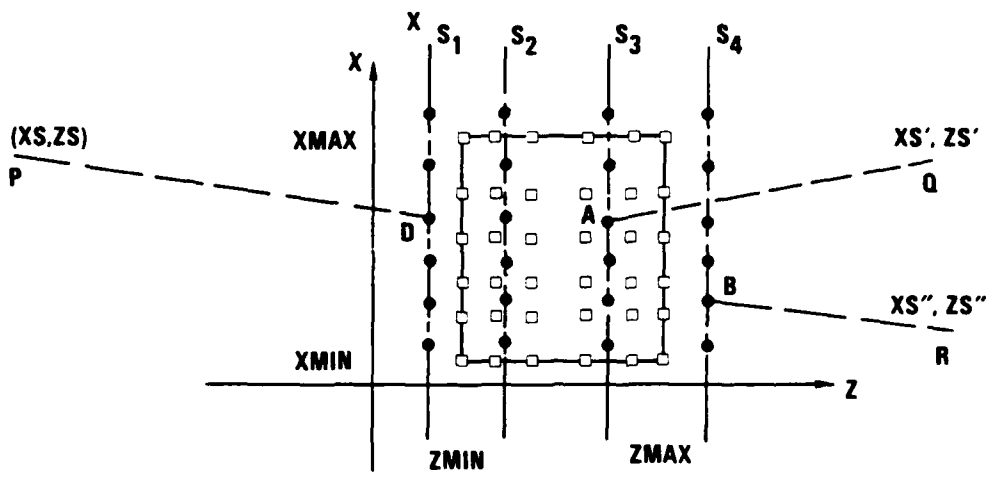
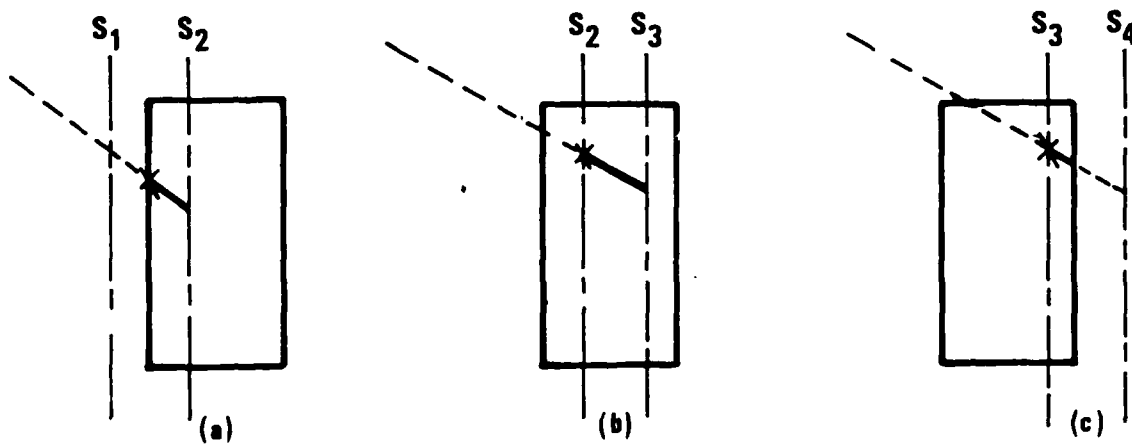


Figure 5-13. Various phase screen placements (S_1, S_2, S_3, S_4), locations of apparent sources (x_s, z_s), (x_s', z_s'), (x_s'', z_s''), given values of refractive index (\square), and positions on phase screens for which the phase factor is to be computed.



(a) Propagation from a point outside to a point inside the medium

(b) Propagation for points within the media

(c) Propagation from a point inside the medium to a point outside

Figure 5-14. Three principal cases of phase factor calculations for propagation from a point outside the medium into the medium.

For purposes of discussion, only apparent sources from the left are considered. Screen S_1 in Figure 5-14a and screen S_2 in Figure 5-14b, are then, respectively, the first phase screens encountered for each configuration. In the case of Figure 5-14a, the phase coefficient is to be calculated for a phase screen point outside the medium but the wave propagates to a screen point within the medium. The partially broken line, continued by the solid line, indicates the ray direction. Only the solid portion is used for physical length calculation. The refractive index is taken as the value at the point on the solid line marked by an X.

In Figure 5-14b, the phase coefficient is to be calculated for a screen located within the medium and the ray also propagates to a phase screen within the medium. The physical distance is given by the solid line and the refractive index taken again to be the value at the point marked by an X.

Figure 5-14c shows the wave propagating to a screen outside the medium. As before, X marks the point for which the refractive index is used and the physical path is the solid line.

Figure 5-15 is a simplified sketch of the phase screens and a given ray to be used for describing the computational procedure. Three screens are used for illustrative purposes. The direction of the ray is given by the slope of the line joining (XS, ZS) to (a, S_1) . The latter phase screen point is the one from which the field propagates. The point (X_1, S_2) is the intersection of the extended ray with the screen S_2 . This is the phase screen point to which the wave propagates. For this particular example, the phase factor is computed as

$$\phi_1(a) = [n(x) - 1] \cdot \Delta S \quad (5.1)$$

where $\phi_1(a)$ is the value of the phase coefficient on screen S_1 at the location (a) and the value of refractive index $n(x)$ is the value at the point

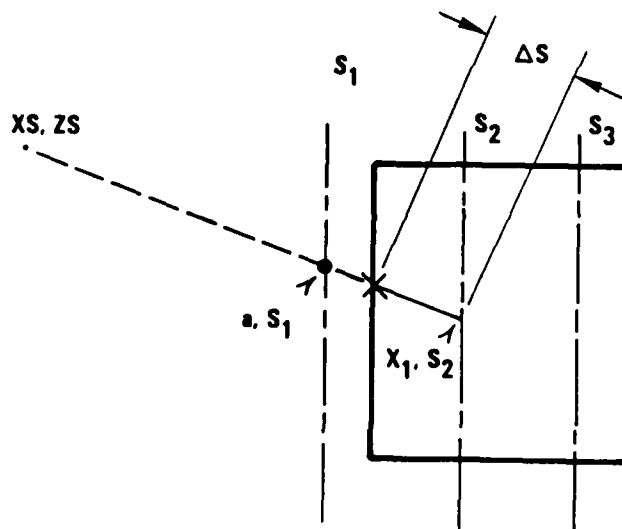


Figure 5-15. Sketch illustrating computational procedure for phase factor ($\phi(a) = [n(x) - 1] \Delta s$).

marked by an x . In this case ΔS is the physical distance between the two screens used in the phase factor calculation.

When the inhomogeneity of the medium varies rapidly it may be necessary to locate more phase screens in the propagation path. Consider Figure 5-16; the three previous screens are illustrated except now the source is assumed to be at a different location. Because more accuracy is required, additional intermediate phase screens have to be used in the calculation. In the figure, two intermediate screens are used. These are labeled σ_a and σ_b . The phase coefficient for this example will be computed as

$$\phi_1(a) = \sum_{p=1}^{N-1} (n(p) - 1) \Delta S p_x \quad (5.2)$$

where $\phi_1(a)$ is the value of the phase coefficient on phase screen S_1 at the point a ; $n(p)$ is the value of the refractive index at the p^{th} intersection of the phase screen and the ray. $\Delta S p_x$ is the physical distance between the

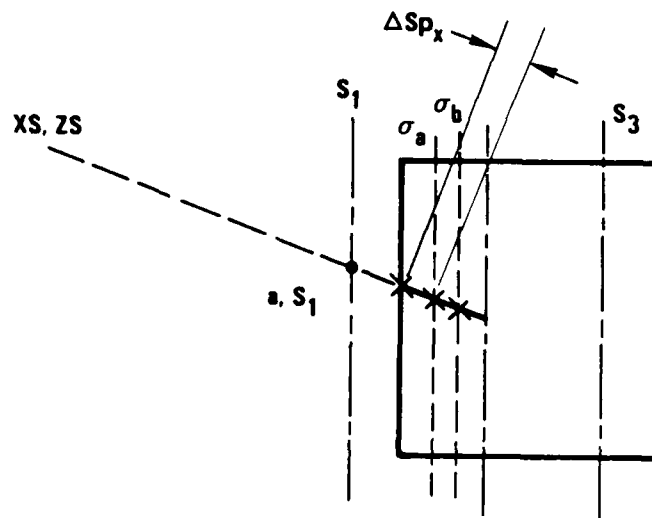


Figure 5-16. Computational procedure when inhomogeneity in medium requires more phase screens for better accuracy [result is given by Equation (5.2)].

point on the p^{th} screen to the point on the $(p+1)^{\text{st}}$ screen. N is the total number of screens; in this case, $N = 4$. The additional interpolating screens are evenly spaced between the given screens for which the phase coefficients are to be computed.

5.2.7 Extraction Efficiency

This section summarizes the results of an APACHE-oriented extraction efficiency study. These results were obtained using a line-center (Voigt profile) model. The codes used to obtain the results, ANOM and CLAM, and their anchoring, are also described.

5.2.7.1 ANOM Code

The ANOM code, developed under the Advanced Chemical Laser Optics Study (ACLOS) program, is a one-dimensional oscillator model. It follows intensity and predicts gain along a one-dimensional path through the oscillator, modeling the feedback process with a reflectivity factor. Two cascade-connected transitions are modeled. The gain model predicts $v = 2, 1,$ and 0 vibrational level populations ($N_2, N_1,$ and N_0) via a kinetics

model described below. Either multiple longitudinal modes, or line-center (Voigt profile) operation, may be modeled.

Gain Model

As the HF medium flows from the nozzle exit, mixes, reacts, and lases, the vibrational state (V) number densities as a function of flow coordinate x, $N_V(x)$, are given by:

$$v(x) \frac{d}{dx} [N_V(x)] = \begin{aligned} &\text{Area change term} \\ &+ \text{Chemical reaction pumping term} \\ &+ \text{Collisional supply terms} \\ &- \text{Collisional depletion terms} \\ &+ \text{Lasing terms} \end{aligned}$$

where $v(x)$ is the flow velocity. In the one-dimensional model, there is no flow coordinate; the concentrations are calculated at one value of x. Therefore, the term on the left side of the equation becomes part of the depletion term, and can be written:

$$\begin{aligned} 0 &= \text{Chemical reaction pumping term} \\ &+ \text{Collisional supply terms} \\ &- \text{Collisional depletion, area change, and } d/dx \text{ terms} \\ &+ \text{Lasing terms} \\ &= F_V + R_V - Q_V N_V + \text{lasing terms.} \end{aligned}$$

In an HF gain medium, the vibrational level populations are given by:

$$N_1 = \frac{F_1 + R_1 + C_1' (F_2 + R_2)/(Q_2 + C_1') + C_0 (F_0 + R_0)/(Q_0 + C_0)}{Q_1 + C_1 Q_2/(Q_2 + C_1') + C_0' Q_0/(Q_0 + C_0)}$$

$$N_0 = (F_0 + R_0)/(Q_0 + C_0) + N_1 C_0'/(Q_0 + C_0)$$

$$N_2 = (F_2 + R_2)/(Q_2 + C_1') + N_1 C_1/(Q_2 + C_1')$$

where

$$C_0 = \sum_J B_{J+1} \frac{B(0, J+1)}{4\pi^{3/2} \Delta v_D} \left[\sum_k I_{1, J+1, v_k} \right]$$

$$C_0' = \sum_J \frac{2J+3}{2J+1} B_J \frac{B(0, J+1)}{4\pi^{3/2} \Delta v_D} \left[\sum_k I_{1, J+1, v_k} \right]$$

$$c_1 = \sum_J B_J \frac{B(1,J)}{4\pi^{3/2} \Delta\nu_D} \left[\sum_j I_{2,J,v_j} \right]$$

$$c_1' = \sum_J \frac{2J+1}{2J-1} B_{J-1} \frac{B(1,J)}{4\pi^{3/2} \Delta\nu_D} \left[\sum_j I_{2,J,v_j} \right]$$

in which the I's are intensities, $\Delta\nu_D$ is the Doppler-broadened linewidth, $B(V,J)$ is the Einstein B coefficient for transition $P_{V+1}(J)$, and

$$B_J = (hc B_e/kT) \exp [-J(J+1) hc B_e/kT]$$

the equilibrium statistical weight of rotational state with quantum number J.

The ANOM gain model was anchored to CROQ code results at a flow coordinate of 1.3 cm. The F, R, and Q parameters were adjusted until the ANOM code vibrational level populations N_0 , N_1 , and N_2 matched those predicted by the CROQ code. (CROQ is a three-dimensional annular laser model, whose gain model has a detailed kinetics and a simple flow model.) Fitting was done at gain lengths of 200, 518, and 916 cm. The parameters are a function of gain length (GL, cm) as follows:

$$F_0 = 0.$$

$$F_1 = 1.0 \times 10^{20}$$

$$F_2 = 7.0 \times 10^{20}$$

$$R_0 = (8.19 - 4.73 \times 10^{-3} GL) \times 10^{20}$$

$$R_1 = (4.81 + 4.73 \times 10^{-3} GL) \times 10^{20}$$

$$R_2 = 11.0 \times 10^{20}$$

$$Q_0 = 3.0 \times 10^5$$

$$Q_1 = (2.94 + 7.77 \times 10^{-3} GL) \times 10^5$$

$$Q_2 = (13.17 - 1.66 \times 10^{-16} GL - 1.74 \times 10^{-5} GL^2) \times 10^5.$$

Further details of the gain model (e.g., how rotational and velocity level populations and gain are calculated) are given in the ACLOS final report (Ref. 5.7)

5.7 "Advanced Chemical Laser Optics Study (ACLOS)," Final Report, AFWL-TR-82-54.

Oscillator Model

ANOM models a one-dimensional path through the oscillator. There is one "gain sheet." For a standing-wave resonator (as opposed to a ring resonator), the intensity at the back mirror is multiplied by $\exp(G CL)$ (CL being the cavity length and G the gain) to "propagate" to the scraper; this intensity is then multiplied by R , the feedback ratio, and again multiplied by $\exp(G CL)$ to "propagate" back to the back mirror. The resulting intensity is compared to the starting intensity for self-consistency; if they are not equal to within the convergence criterion, the intensity is updated according to:

$$I_{\text{new}} = (I_{\text{old}})^{(1-d)} \times [(I_{\text{old}}) \exp(G CL) R \exp(G CL)]^d$$

where d is a user-specified damping factor. The intensity used to calculate the gain G is the sum of the average intensities for each pass:

$$I_{\text{avg}}(\text{pass 1}) = I [\exp(G CL) - 1] / (G CL)$$

and

$$I_{\text{avg}}(\text{pass 2}) = I \exp(G CL) R [\exp(G \cdot CL) - 1] / (G CL).$$

Formulae for the gain calculation are given in reference 5.7. When the intensity at the back mirror has converged, the output intensity at the scraper is calculated as:

$$I_{\text{out}} = I \exp(G CL) (1 - R).$$

Although the ALPHA resonator is a ring, it is modeled as a standing wave resonator because the photons pass through the gain medium in both directions. The resonator length is input to the ANOM code as half of its actual value, so that the proper longitudinal mode spacing for the ring is simulated. Longitudinal mode spacing is approximated as that of a "closed cavity" resonator.

The ANOM code output intensities are used as input to the amplifier model, CLAM. A multiple-longitudinal-mode output from an ANOM run

simulating a 200-cm gain length ALPHA resonator is given in Figures 5-17a through 5-17d.

5.2.7.2 CLAM Code

CLAM predicts the amplification of the oscillator intensity by the amplifier. The CLAM gain model is the same as that of the ANOM code.

Amplifier Model

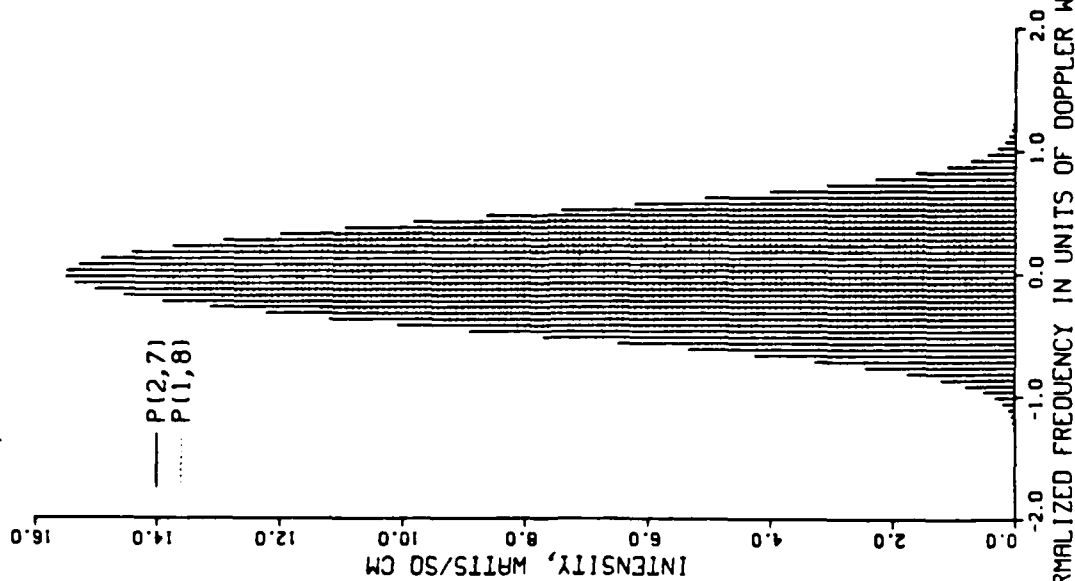
The CLAM amplifier model is an adaptation of the amplifier model in the code PSTAR. It was modified so that it would model an ALPHA-like device. A schematic of this device is shown in Figure 5-18.

If the logical parameter FORWARD is true, the beam from the oscillator enters at the waxicon inner cone, is annularized to the waxicon outer cone, then expands as it passes through the gain medium to the rear element; it then gets smaller as it passes back through the gain medium to the reflaxicon outer cone, is compacted to the reflaxicon inner cone, and is sent to the phase conjugation device; upon return from the phase conjugator (PC), the beam retraces itself and exits the amplifier from the waxicon inner cone. If FORWARD is false, the beam enters and exits at the reflaxicon inner cone, and the phase conjugator is on the "waxicon side." Note that an actual ray in this amplifier would have its upstream and downstream passes through the gain medium on opposite sides of the gain generator. However, since our model follows a one-dimensional path through the amplifier, and since it is assumed that the intensity is cylindrically symmetric, the intensity path in CLAM will be the one shown in the figure.

The logical variable ALPHA2 (for 2 passes through the gain medium from input to the PC) controls whether or not this model is used. There is also an ALPHA1 (1 pass) option, which would model the case of a device with one axicon on either end of the annular leg. This option was rejected for the ALPHA resonator device because of the extreme sensitivity to axicon tip-to-tip alignment; when the axicon inner cones are back-to-back and the outer cones are in one piece, this sensitivity is ameliorated. It may be, however, that the amplifier would not have such extreme sensitivity, and that the 1-pass configuration may have a greater extraction efficiency. It

Q. HF MOLECULE, STANDING WAVE

CAVLENG - 12.500 M GNLENG - 1.000 M T - 578.0 DEG K R - .120
 P - 4.50 TORR FLOWVEL - 1.900E+05 CM/SEC FLOWANG - 0.0 DEG
 (2P7,1P8) - (298.4, 254.1) WATTS/50 CM (FLUX EACH WAY)



D. HF MOLECULE, STANDING WAVE

CAVLENG - 12.500 M GNLENG - 1.000 M T - 578.0 DEG K R - .120
 P - 4.50 TORR FLOWVEL - 1.900E+05 CM/SEC FLOWANG - 0.0 DEG
 (2P7,1P8) - (298.4, 254.1) WATTS/50 CM (FLUX EACH WAY)

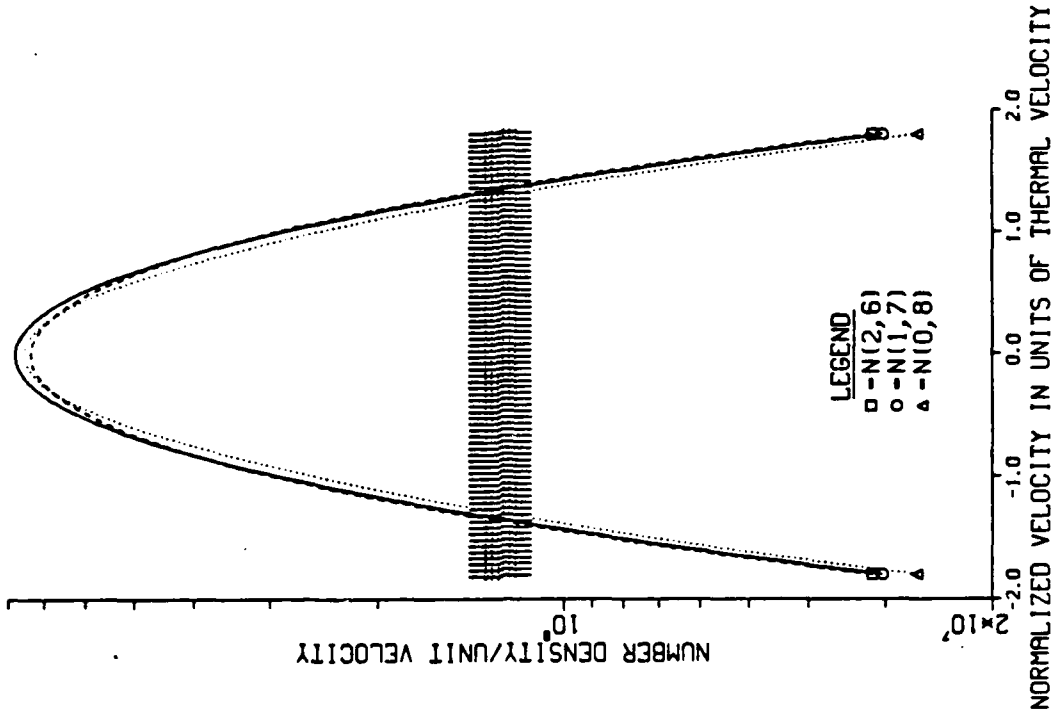
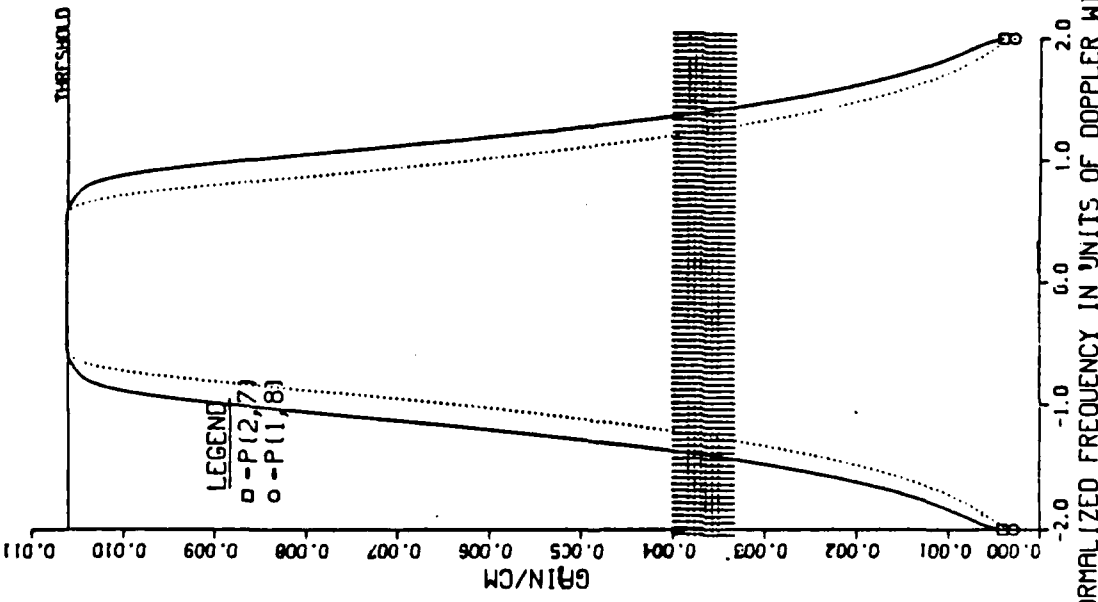


Figure 5-17. ANOM multiple-longitudinal-mode output.

C. HF MOLECULE, STANDING WAVE

CAVLENG - 12.500 M GNLENG - 1.000 M T - 578.0 DEG K R - .120
 P - 4.50 TORR FLOWVEL - 1.900E+05 CM/SEC FLOWANG - 0.0 DEG
 (2P7,1P8) - (298.4, 254.1) WATTS/50 CM (FLUX EACH WAY)



d. HF MOLECULE, STANDING WAVE

CAVLENG - 12.500 M GNLENG - 1.000 M T - 578.0 DEG K R - .120
 P - 4.50 TORR FLOWVEL - 1.900E+05 CM/SEC FLOWANG - 0.0 DEG
 (2P7,1P8) - (298.4, 254.1) WATTS/50 CM (FLUX EACH WAY)

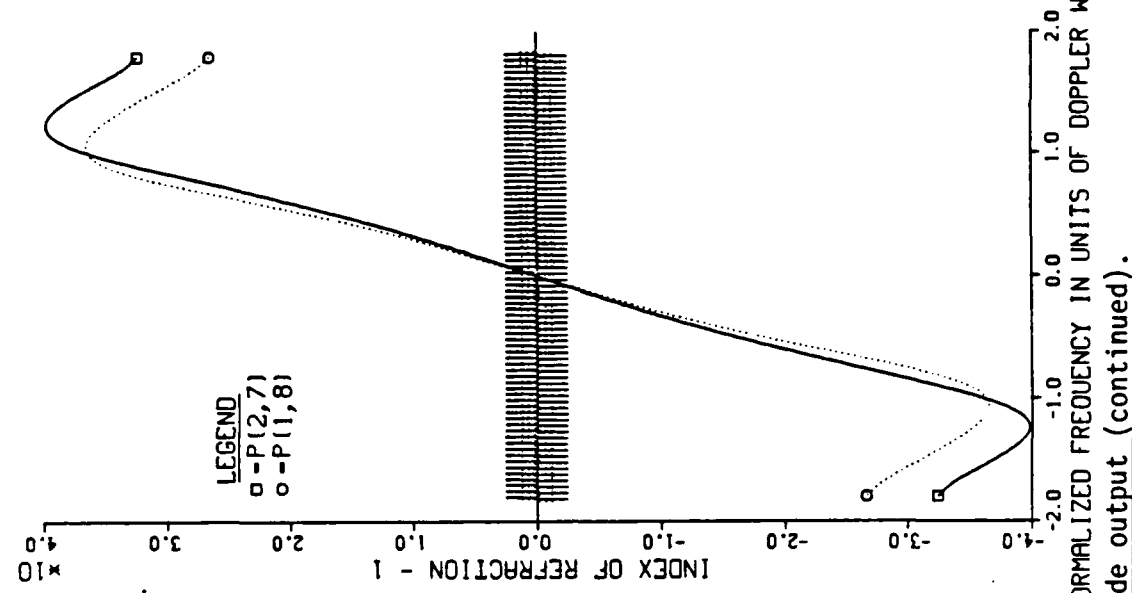


Figure 5-17. ANOM multiple-longitudinal-mode output (continued).

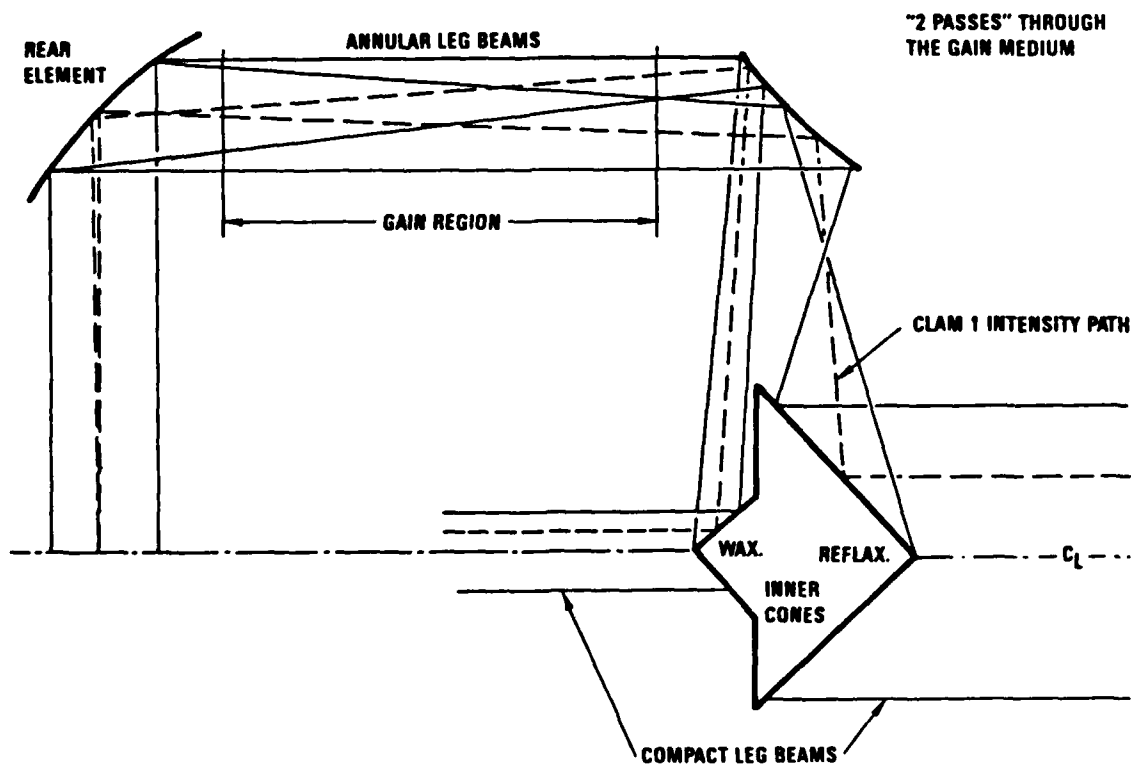


Figure 5-18. CLAM amplifier model.

is recommended that 1-pass extraction efficiency, alignment sensitivity, and polarization implications be investigated by the APACHE program.

The input intensities are scaled from the compact beam size to the annular beam size upon entering the annular region, and scaled conversely when leaving the annular region. Furthermore, as the beam passes through the annular region, the intensities and beam overlap are scaled according to the area change and the proper geometry, as shown in the figure. In the runs made to date, a compact beam radius of 12.5 cm was used, in order to have a uniform set of intensity results. However, in "real life" the axicon inner cone sizes will be dictated by engineering considerations. In the ALPHA2 configuration, the beam sizes have been: rear element, 2.6 cm; waxicon outer cone, 1.0 cm; reflaxicon outer cone, 1.3 cm (as in the ALPHA resonator). It is assumed that these will be the best values for use with the nominal ALPHA flow conditions; if the flow is changed, these values will have to be reoptimized.

There is an arbitrary (user-specified) number of "gain sheets." The gain at each "sheet" is calculated using the average intensity there. This average intensity is made up of contributions from the appropriate intensity going to and coming from the PC (the "two-way intensity"), and the overlap factor times the "two-way intensity" of the opposing annular leg beam. As in ANOM, the average intensity is

$$I_{ave} = I [\exp(G DL) - 1]/(G DL)$$

where DL is the gain length represented by one gain sheet.

Because the gain at a particular gain sheet is determined by all of the intensities passing through the gain sheet, there needs to be an initial guess for all of the intensities. CLAM subroutine GUESS supplies these initial intensity guesses. GUESS solves a one-gain-sheet amplifier (in a way analogous to that in which the ANOM code solves a one-gain-sheet oscillator), then defines the intensity at gain sheet i to be

$$I_i = I_{i-1} \exp(G DL).$$

The PC is modeled by a reflectivity, R_{PC} . Thus

$$I \text{ (after PC)} = I \text{ (before PC)} \times R_{PC}.$$

The CLAM code also has a logical parameter, ONEWAY, which allows modeling of a "one-way" pass through the amplifier; i.e., the beam enters at one axicon, goes through the gain medium, then leaves at the other axicon. This allows the code to simulate one pass through an oscillator; this oscillator simulation is used in the intensity-to-power calibration described below.

Intensity/Power Calibration and Consistency Checks

a. ANOM/CLAM Consistency Check

The ALPHA device has an outcoupling fraction of 0.88 and a feedback fraction of 0.12 (as predicted by the CROQ code). Thus the ANOM code was run with $R = 0.12$ in order to model the ALPHA resonator. Since the ANOM code output assumes the 0.88 outcoupling fraction, if the ANOM intensity output is multiplied by $0.12/0.88 = 0.136$, that intensity should represent

the amount of intensity fed back into the oscillator on each pass. If the CLAM model is configured as an oscillator (ONEWAY true) with the same gain length, then this input intensity should be amplified by a factor of $1.0/0.12 = 8.33$, the same as the one-pass amplification of the oscillator.

Since the ANOM code does not scale the annular intensities to the compact beam area, the CLAM code was set up to give the same area for both the compact beam and the beam entering the annular leg. The lines modeled were $P_2(7)$ and $P_1(8)$. Table 5-3 gives the results of the CLAM runs for both line center and multiple longitudinal mode models. The probable reason that the results are not exactly 8.33 is that ANOM does not have the ALPHA device annular leg geometry.

TABLE 5-3. ANOM/CLAM Consistency Check.

| Line | Line Center Model | Multiple Mode Model |
|-----------------------------------|-------------------|---------------------|
| $(I_{out}/I_{in}$ should be 8.33) | | |
| $P_2(7)$ | 8.32 | 8.38 |
| $P_1(8)$ | 8.29 | 8.35 |

b. ANOM/CROQ Consistency Check

Since the ANOM "kinetics parameters" have been adjusted so that the ANOM-predicted values of N_0 , N_1 , and N_2 match those of CROQ, the consistency check must involve the predicted intensities.

The CROQ code predicts that the lines $P_2(7)$ and $P_1(8)$ are two of the most powerful lines in the resonator output for gain lengths ranging from 200 to over 900 cm. Therefore, these lines were modeled with ANOM and CLAM. ANOM calls the upper level intensity I_1 and the lower, I_0 . If ANOM correctly models the gain medium response, then I_1/I_0 is expected to be the same as that of CROQ and I_1+I_0 to be proportional to that of CROQ (with the same proportionality constant for all gain lengths).

Table 5-4 gives the results of these tests, and shows the details of the anchoring results for vibrational level populations. The intensity

TABLE 5-4. ANOM/CROQ Consistency Check.

| Gain Length (cm) | 204 (ALPHA I) | 518 (ALPHA II) | 705 ("APACHE7") | 916 ("APACHE9") |
|--|------------------|-------------------|--------------------|--------------------|
| Gain Model Anchoring | | | | |
| N_0 (CROQ) $\times 10^{-15}$ | 3.1 | 3.3 | | 3.4 |
| N_0 (ANOM) $\times 10^{-15}$ | 3.0 | 3.2 | | 3.4 |
| N_1 (CROQ) $\times 10^{-15}$ | 1.9 | 1.8 | | 1.8 |
| N_1 (ANOM) $\times 10^{-15}$ | 1.9 | 1.8 | | 1.8 |
| N_2 (CROQ) $\times 10^{-15}$ | 1.1 | 1.0 | | 1.0 |
| N_2 (ANOM) $\times 10^{-15}$ | 1.2 | 1.1 | | 1.0 |
| Intensity Ratio | | | | |
| I_1/I_0 (CROQ) | 1.4 | 1.0 | 0.8 | 0.9 |
| I_1/I_0 (ANOM) | 1.1 | 1.2 | 1.3 | 1.3 |
| $\frac{P_{CROQ}^{out}}{I_1+I_0}$ / (Ann. Area) (ANOM) | 2.0 | 2.5 | 2.3 | 2.4 |

results are only fair. The result at the 200 cm gain length is somewhat different from those at the other gain lengths due to the much larger power fraction on $P_2(7)$ -- 33% at 200 cm; 22% to 24% at the longer gain lengths.

c. Scaling ANOM-Predicted Intensity to CROQ Power

The ANOM code models only the annular leg of the ALPHA resonator. It does not model the actual annular leg geometry, but assumes total overlap of both passes through the gain medium, and a constant beam width. If the annular leg were modeled properly in ANOM, the annular output intensity to the compact intensity could be simply scaled by the ratio of the areas. However, there is no way of knowing the "effective gain width" (W_{eff}) for the ANOM run.

If W_{eff} were known, then the ALPHA I device (gain length 200 cm) output power P_1 would be represented by the intensity

$$(I1 + I0) \text{ (from ANOM)} \times (\text{AREA}_{annular}) / (\text{AREA}_{compact})$$

where

$$\text{AREA}_{annular} = 2 \pi R_{avg} W_{eff}$$

$$\begin{aligned} R_{avg} &= R \text{ (gain generator)} + \text{Mode Offset} + 1/2 W_{eff} \\ &= \text{approximately } 56.6 \text{ for ALPHA I; thus} \end{aligned}$$

$$\text{AREA}_{annular} = 356 W_{eff}$$

$$\text{AREA}_{compact} = \pi R_{compact}^2 = \pi (12.5)^2 = 491.$$

Since W_{eff} could reasonably be anything between 1.3 and 2.6, the ratio $\text{AREA}_{annular} / \text{AREA}_{compact}$ is expected to be between 0.94 and 1.89.

In order to actually scale the intensities, the fact that the one-pass amplification of the oscillator is 8.33 was used. The oscillator intensities were adjusted (by multiplying by the scaling factor IMULT) until the CLAM output intensities for the 200 cm gain length (ALPHA2 true, FORWARD true, ONEWAY true) were 8.33 times the input intensities. The IMULT value needed to give this result was 0.15, very close to the expected value of 0.136 (see ANOM/CLAM Consistency Check, above). The CLAM output intensity sum represents 1.0/0.88 of P_1 , since CLAM does not subtract any of its output for feedback as ANOM does. Thus

$$(I1 + I0) \text{ (CLAM output)} \times 0.88 \text{ represents } P_1.$$

The actual numbers were:

$$(I1 + I0) \text{ (CLAM output)} \times 0.88 = 1889$$

$$(I1 + I0) \text{ (ANOM output)} = 1136$$

$$\text{Ratio (Scaling Factor)} = 1.66$$

which gives a reasonable number for W_{eff} , 2.3 cm.

Thus, in order to simulate an amplifier input power $P_i = f P_1$, the ALPHA I ANOM output should be scaled by $\text{IMULT} = f 1.66$; the output power P_o is determined by

$$P_0 = (I1 + I0) \text{ (CLAM output)}/1889 \times P_1.$$

Extraction Efficiency for Line Center (Voigt Profile) Model

a. Amplifier Size Choices

The following assumptions were made:

1. The goal for power output per amplifier is $P_A = 4.1667 P_2$, where P_2 is the ALPHA II output power goal.
2. The "nominal ALPHA flow conditions" are used.
3. The power predicted by CROQ for an oscillator is approximately the same as the power output of an amplifier.

With these assumptions, the curve for the required gain generator radius as a function of gain generator length is shown in Figure 5-19.

The actual curve will be similar to this one. If the extraction is more efficient than this curve predicts, then the actual curve will be lower and to the left of the curve shown.

There are a number of factors which put an upper limit on the gain generator radius. These include: vehicle size limitation, mirror manufacture capability, and alignment tolerance. The vehicle size limitation on gain generator radius is about 150 cm.

Also, a number of factors put an upper limit on the gain generator length. These are amplified spontaneous emission (ASE), gain generator structural stability and alignment tolerance (which get worse as the length-to-diameter ratio gets larger), diffraction loss, the "gain-phase effect," and vehicle size limitation. The upper limit on gain generator length is not yet clear.

Because the CROQ code has only one gain sheet, the code is not very stable at gain lengths above 9 m. For that and the above reasons, amplifier extraction efficiency in the gain generator length range of up to 9 m was chosen for study.

Also it was assumed that the annular leg mirror configuration is the same as that in the ALPHA device, since that configuration was shown to produce the best extraction. Thus the geometric mode is assumed to be 2.6 cm wide and be offset from the gain generator by 3 mm. The waxicon

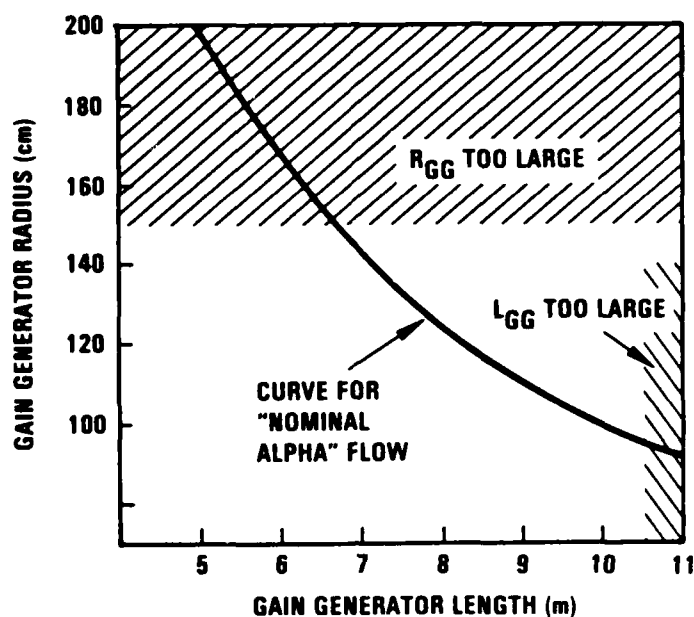


Figure 5-19. Gain generator radius versus length.

outer cone is assumed to be 1.0 cm wide, and the reflexicon outer cone is assumed to be 1.3 cm wide.

b. ALPHA I-Sized Amplifier -- Comparison with g_0 - I_{sat} Model

Before proceeding to the APACHE-sized device studies, CLAM was used to duplicate the PALS MOPA system model (Ref 5.8). This study looked at power to the phase conjugator as a function of power input to the amplifier.

The model assumed

$$g = g_0 / (1 + I / I_{sat}),$$

where I is the two-way intensity. The model originally did not account for overlap of the annular leg passes, however it was subsequently modified and the new results are presented in Section 5.2.8.

The CLAM calculation was done both with and without annular leg overlap. Figure 5-20 shows the results. (The numbers by the symbols are the

5.8 "PALS MOPA System Model," V.W. Chai, TRW IOC 86.K325,VWC-001, 15 Jan 1986.

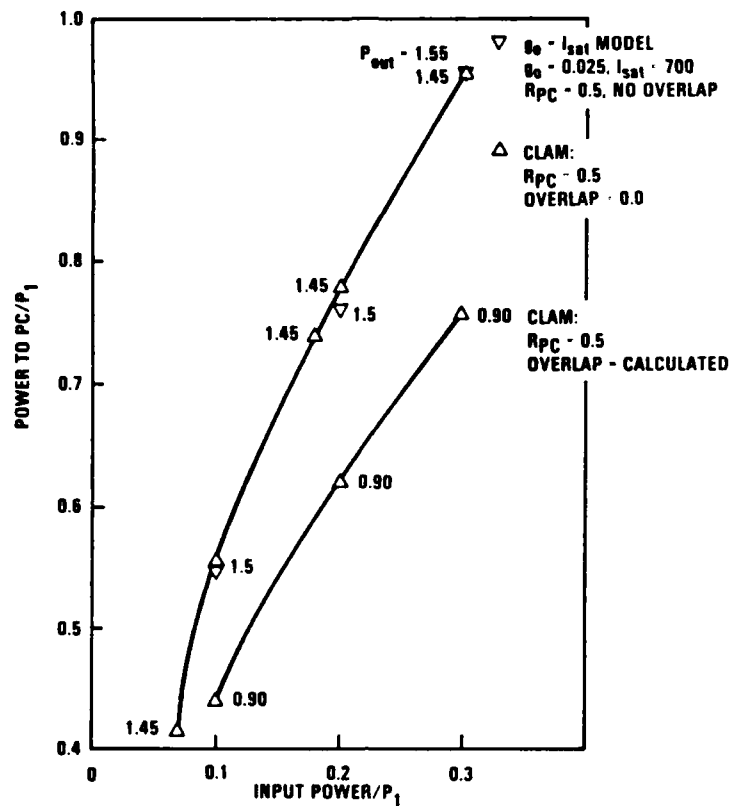


Figure 5-20. Extraction for ALPHA I-size amplifier.

output powers. All powers have been normalized to P₁.) The results obey the approximate algorithm

$$P_{PC} = (P_{in} P_{out} / R_{PC})^{1/2}$$

where R_{PC} is the effective pulse conjugator reflectivity.

It is seen that the annular leg overlap leads to about 20 percent lower power to the phase conjugator than if no overlap were present. Also, it appears that g₀ and I_{sat} values of 0.025 and 700, respectively, would give gain model results similar to those of CLAM. (These are lower than the values of 0.03 and 1100 based on numbers predicted by the CROQ code.)

c. Extraction Efficiency at 5, 7, and 9 m Gain Lengths

Figure 5-21 shows the line-center-model predictions of CLAM for the power out and power to the phase conjugator of 5, 7, and 9 m amplifiers.

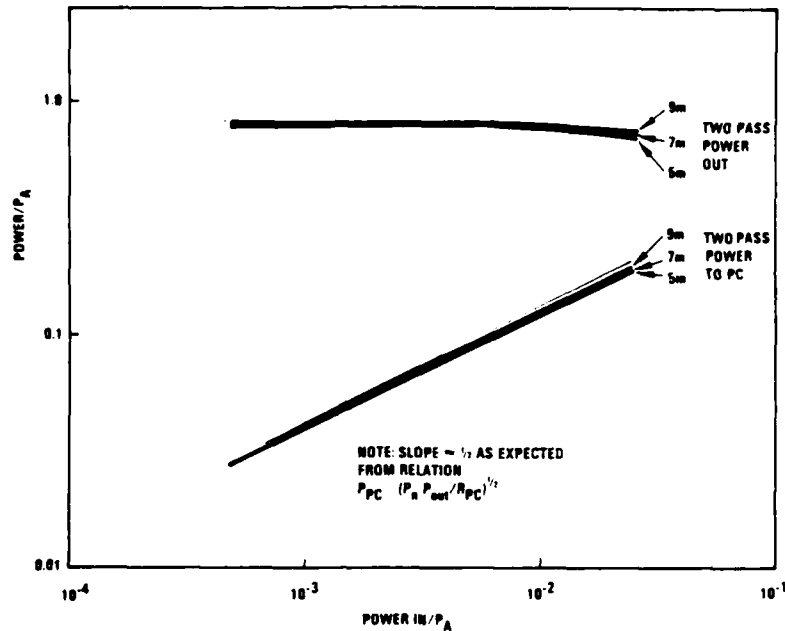


Figure 5-21. P_{PC} and P_{OUT} as a function of P_{in} (CLAM, Voigt profile model).

The gain generator area was kept constant. Powers shown are normalized to $P_A = 4.1667 P_2$. The gain length does not seem to have a significant effect on extraction efficiency.

The output power appears to be a weak function of input power. Thus, the requirement for input power will be determined by the requirement for power to the phase conjugator and possibly by ASE considerations.

5.2.8 PALS MOPA System Model Upgrade

The PALS MOPA system model documented in reference 5.8 is a simple microcomputer model that has been modified to incorporate the beam overlap as the beam travels back and forth through the ALPHA-like gain generator. This section describes the changes made to the model and shows the effects of the beam overlap to the power delivered to the SBS cell and the system output power.

5.2.8.1 Background

The model documented in reference 5.8 assumed that there is no overlap between the annular leg passes through the gain generator, for a first order assessment of the PALS system performance. This led to an optimistic

prediction of the power produced by the amplifier. The effort described here includes the beam overlap to obtain a better estimation of the power out of the amplifier. The upgraded model also simulates the beam size (which was assumed to be constant in the previous effort), as it propagates from the waxicon outer cone to the rear cone and back to the reflexicon outer cone, using the ALPHA configuration.

5.2.8.2 Simulation of the Beam Size

The size of the annular leg determines the effective annular area and thus the intensity in the gain medium. Figure 5-22 shows the mirror configuration used in the model with a variable gain generator length. The beam expands linearly from 1.0 cm at the waxicon outer cone to 2.6 cm at the rear cone mirror and contracts linearly from 2.6 to 1.3 cm at the reflexicon outer cone. The model ignores the curvatures of the mirrors since they have a negligible effect on the total length. A typical example of the annular area is shown in Figure 5-23 as a function of the position in the gain generator.

5.2.8.3 Modeling of the Beam Overlap

The model first determines where the overlap occurs within the gain generator. The inception of the overlap is calculated when the summation of the annular thicknesses of the passes amounts to an arbitrary value of 2.7 cm. Note that the annular leg passes are bounded between 2.6 cm at the rear cone mirror and 2.8 cm at the waxicon/reflexicon outer cone. The overlap factor then varies linearly from zero at the inception point to 1.0 at the rear cone mirror. The calculated overlap factor is shown in Figure 5-24 as a function of the position in a 7-meter gain generator. It is shown that there is no overlap at the waxicon/reflexicon end of the gain generator.

As described in reference 5.8, the equivalent gain at any position, x , is calculated by

$$g_x^n = g_0 / (1 + ITOT/I_{sat})$$

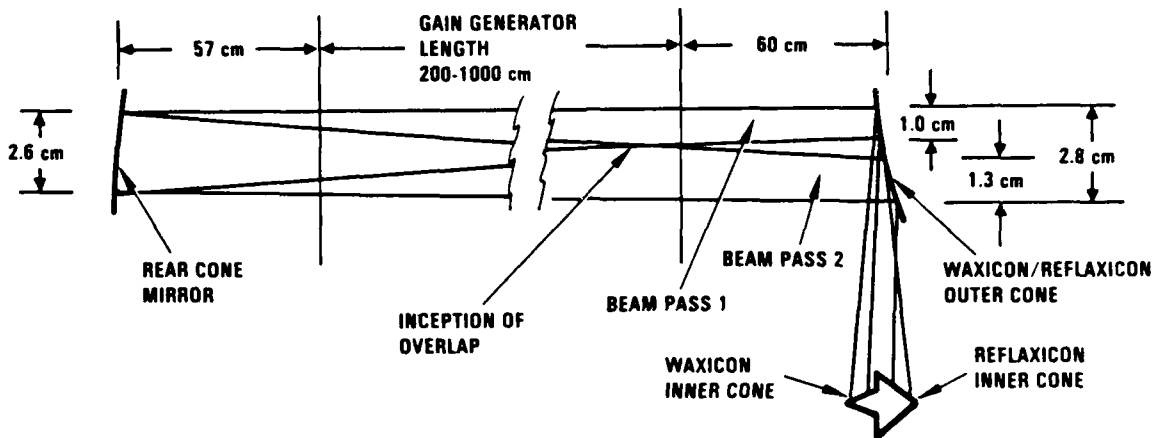


Figure 5-22. Beam passes through amplifier.

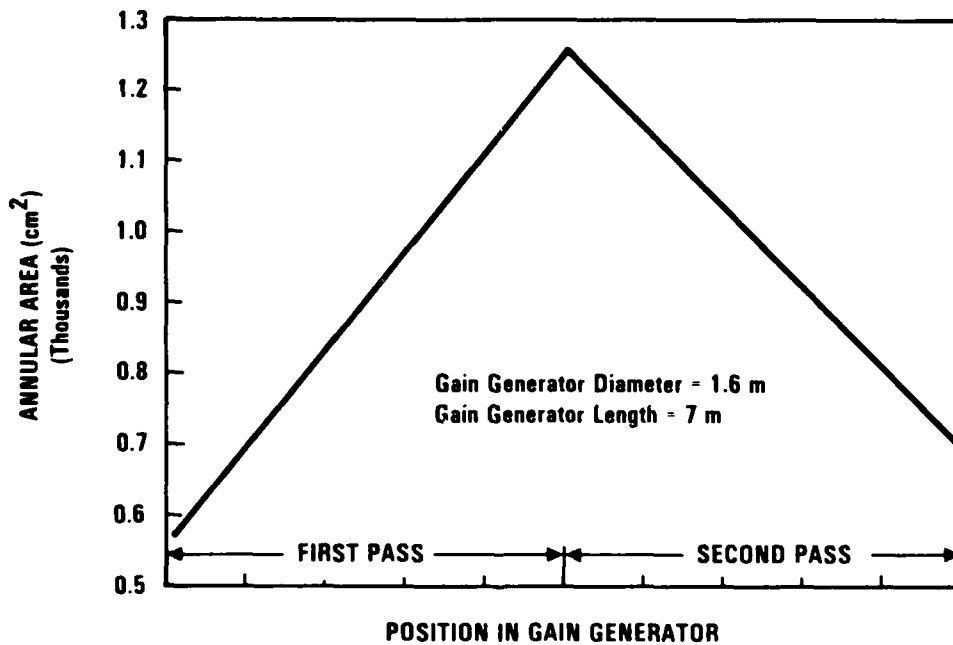


Figure 5-23. Typical annular area at any point in gain generator.

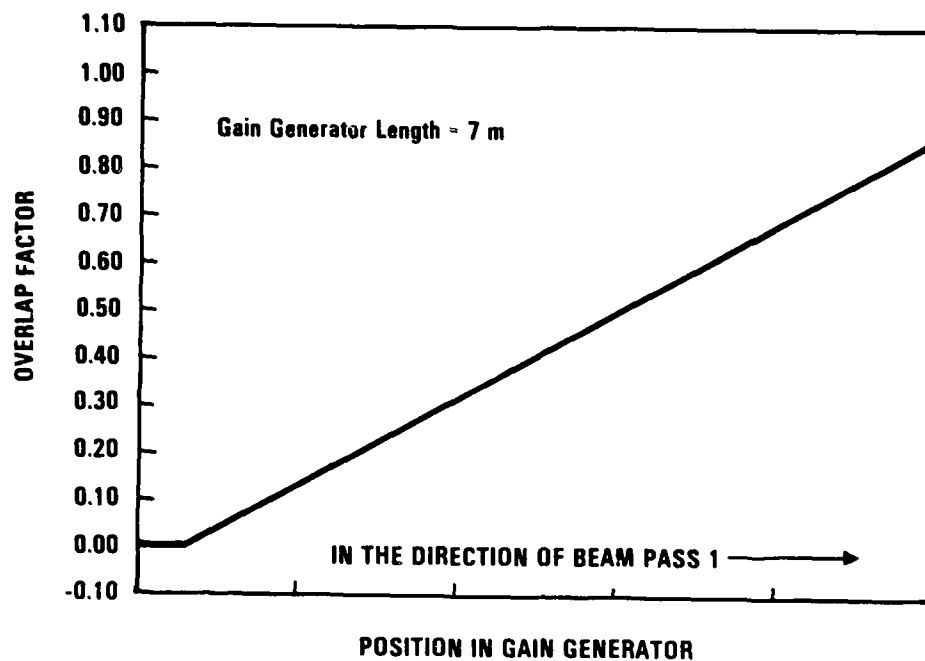


Figure 5-24. Typical beam overlap factor.

where x and n denote the position being calculated and the current iteration, respectively. The ITOT, the total intensity present at any point x , is calculated according to the following algorithms:

For the first pass, unconjugated beam,

$$ITOT = I_{f_{x-1}}^n |_{p1} + I_{b_x}^{n-1} |_{p1} + \left(I_{f_x}^{n-1} |_{p2} + I_{b_x}^{n-1} |_{p2} \right) \times F_x$$

For the second pass, unconjugated beam,

$$ITOT = I_{f_{x-1}}^n |_{p2} + I_{b_x}^{n-1} |_{p2} + \left(I_{f_x}^n |_{p1} + I_{b_x}^{n-1} |_{p1} \right) \times F_x$$

For the second pass, conjugate beam, . . .

$$ITOT = I_{f_x}^n |_{p2} + I_{b_{x+1}}^n |_{p2} + \left(I_{f_x}^n |_{p1} + I_{b_x}^{n-1} |_{p1} \right) \times F_x$$

For the first pass, conjugate beam,

$$ITOT = I_{f_x}^n |_{p1} + I_{b_{x+1}}^n |_{p1} + \left(I_{f_x}^n |_{p2} + I_{b_x}^n |_{p2} \right) \times F_x$$

where F represents the overlap factor and the subscripts f, b, and p denote the forward nonconjugated beam, backward conjugated beam, and beam pass (first or second) respectively.

The instantaneous intensity at any point is then calculated as follows:

For the forward-going, unconjugated beams,

$$I_{f_x}^n = I_{f_{x-1}}^n (1 + g_x^n \Delta x) (\text{area}_{x-1} / \text{area}_x)$$

For the backward-going, conjugate beams,

$$I_{b_x}^n = I_{b_{x+1}}^n (1 + g_x^n \Delta x) (\text{area}_{x+1} / \text{area}_x)$$

5.2.8.4 Results

Figure 5-25 shows the equivalent gain through the gain generator for the conditions stated. The equivalent gain for the case without beam overlapping was also included for comparison. It is shown that the gain is lower with beam overlapping during the second pass compared to that without beam overlap. The lower gain translates to lower amplification, resulting in lower power produced by the amplifier.

Figure 5-26 shows the power delivered to the SBS cell as a function of the gain generator length (using the space-based laser normalization factor). The beam overlap resulted in 15-22 percent lower power delivered to the SBS cell. This finding is in good agreement with that documented in

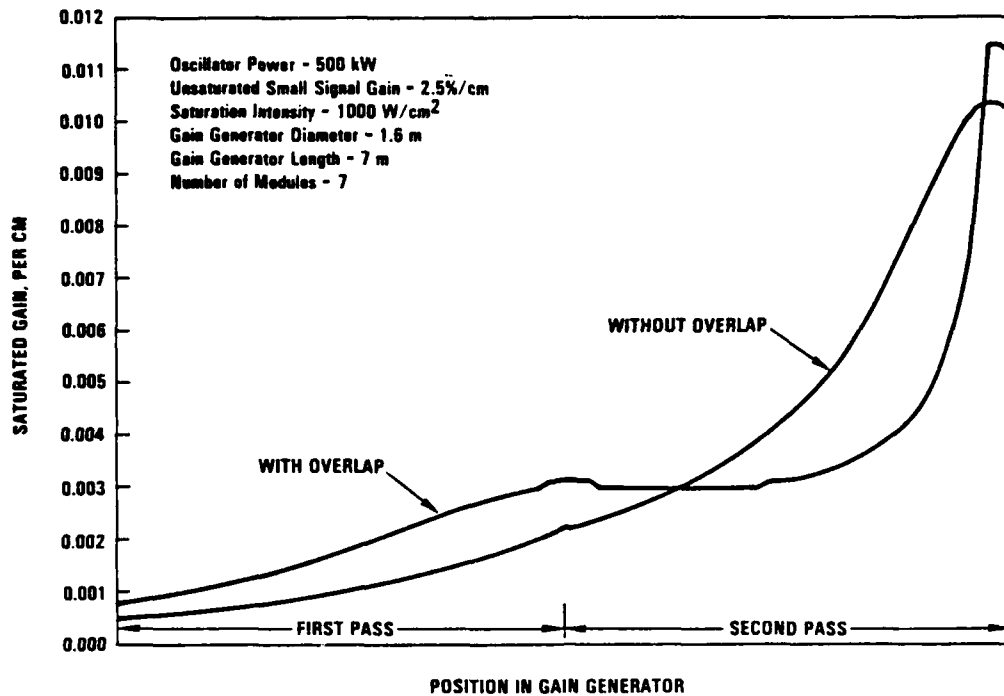


Figure 5-25. Equivalent gain in gain generator.

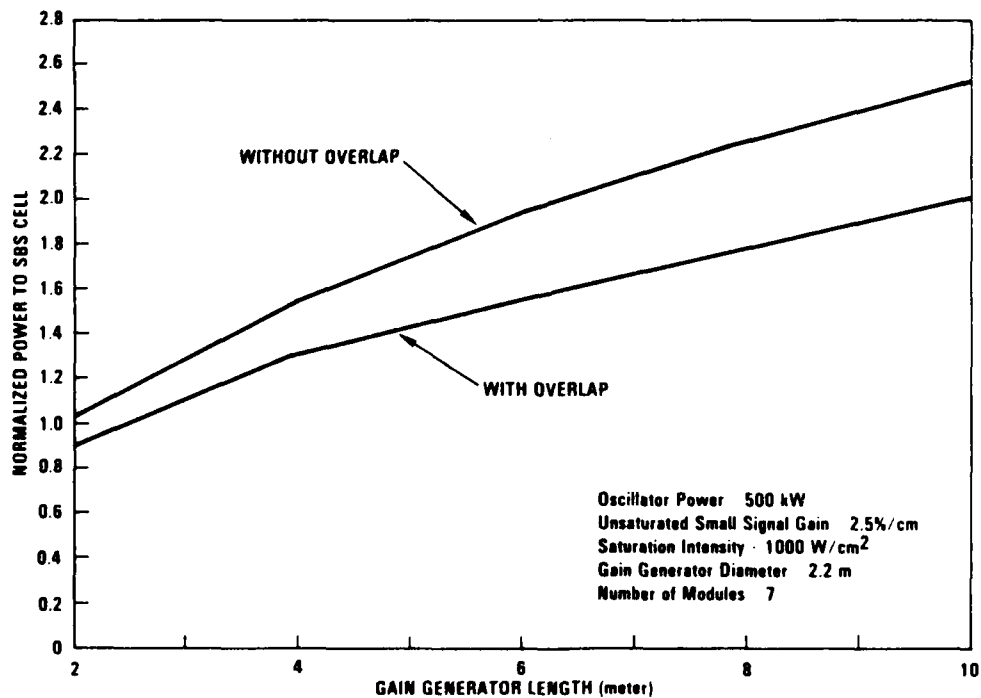


Figure 5-26. Power delivered to SBS.

reference 5.9. Figure 5-27 illustrates the system output power as a function of the gain generator length. The beam overlap leads to 25-35 percent lower system output power.

5.2.8.5 Conclusions

The MOPA system model has been modified to incorporate the capability to simulate the beam size as it travels through the gain generator and to study the effect of the beam overlap on the power produced by the amplifier. For the range of gain generator length studied, the MOPA system model predicts a 15-22 percent lower power delivered to the SBS cell and a 25-35 percent lower system output power with the beam overlap compared to those without beam overlap.

5.3 LOW/HIGH POWER BEAM SEPARATION GRATING RHOMB ISOLATION STUDY

An analytical and subscale fabrication study was undertaken to assess performance and fabrication issues associated with using a grating rhomb which, when properly configured, serves to couple the low power beam from the APACHE oscillator to the amplifier/phase conjugation subsystem, extract the return phase conjugated high power APACHE beam, and also isolate the APACHE oscillator from the high power return beam.

A representative grating rhomb configuration which illustrates the objective is shown in Figure 5-28. A low-power oscillator beam is specularly reflected onto the secondary of the grating rhomb which possesses very high efficiency in the TE first order polarization. The TE first order is then reflected off the grating primary and propagates to the system amplifier. The high-power phase conjugated return beam with its polarization rotated by 90 degrees is outcoupled via the high efficiency TM zeroth-order polarization of the primary. The TM first order is designed to have very low efficiency so that only a small percentage of the high power beam is fed back to the oscillator subsystem. Further isolation of this fed-back beam with a separate element may be necessary.

5.9 "Extraction Efficiency I," D. Dee, TRW IOC 85.K323-78, 31 Dec. 1985.

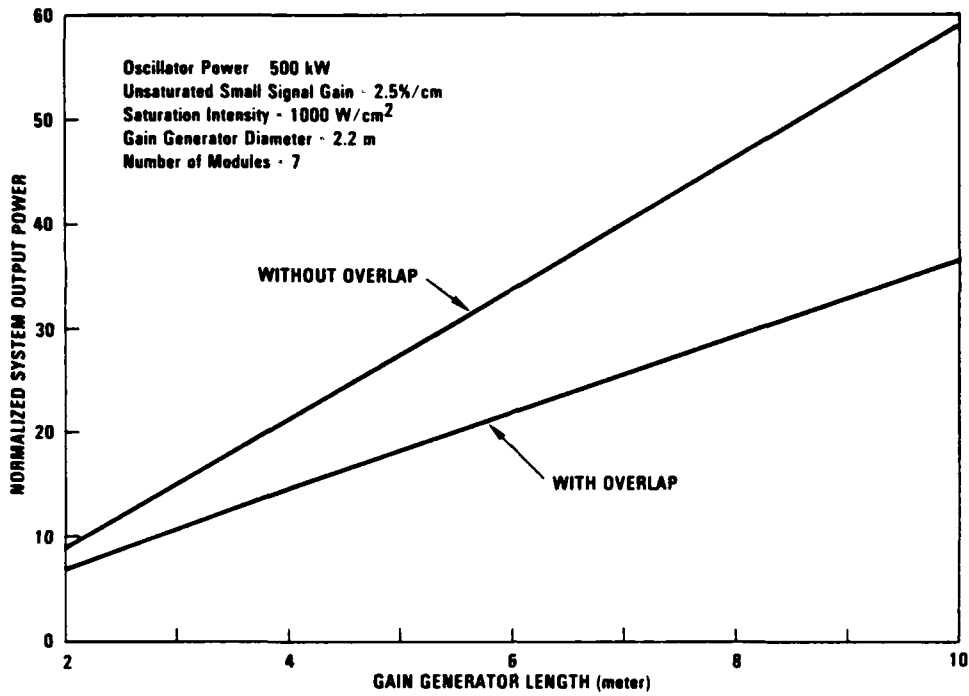


Figure 5-27. System output power.

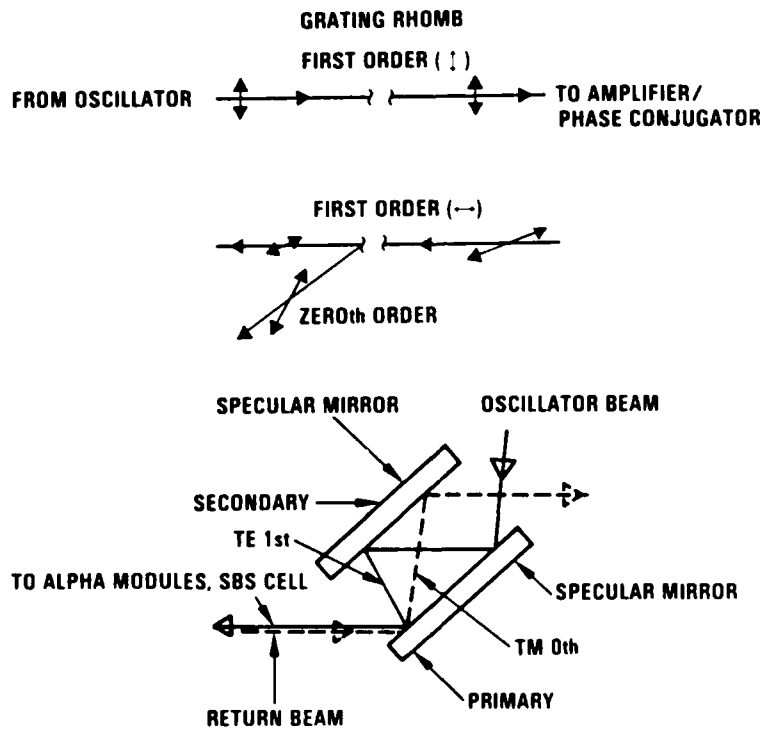


Figure 5-28. Grating rhomb configuration.

The primary analytical tool used in this study was the in-house French Grating Code which accepts input design parameters (wavelength, incident angle, grating reflection coefficient, groove depth, period, duty cycle, and contour) and predicts grating efficiencies for possible orders in both polarizations.

The grating subscale effort was to explore fabrication methods by which deep grooves could be milled into subscale samples using the existing ALPHA grating master. Controlling groove depth and groove contour and measuring the effect on TE, TM, and zeroth order efficiencies were initial goals.

5.3.1 Grating Rhomb Design Goals

The design goals as set forth in the PALS Preliminary Requirement Review (PRR) of 23 October 1985 were:

1. Grating rhomb efficiency for the incoupled oscillator beam to be greater than 90 percent
2. Grating rhomb efficiency for the outcoupled high power beam to be greater than 95 percent
3. Grating rhomb efficiency for the high power orthogonal polarization return beam to be less than 5 percent.

These design goals were arbitrarily set pending more mature system studies.

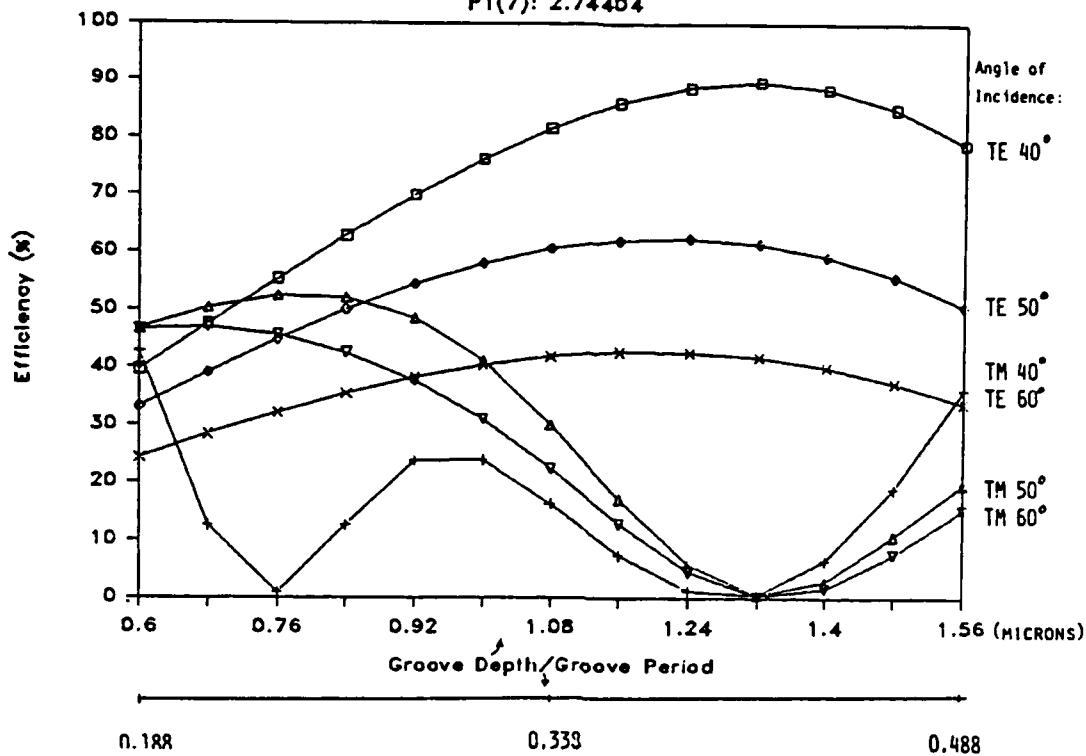
5.3.2 French Grating Code Results

Early modeling of a lamellar (square-groove) grating with deep grooves showed:

1. At an incident angle of 40 deg and using a lamellar (square groove) groove depth of 1.32 microns with a groove period of 3.2 microns, it was possible to in-couple 81 percent of the oscillator beam power (Figure 5-29, TE-first order) and outcouple 81 percent of the high power beam (four power weighted ALPHA strong lines) while allowing only 0.04 percent of the orthogonal polarized high power beam to return. (Figure 5-29 TM-first order).
2. Higher angles of incidence significantly reduced oscillator in-coupling efficiencies (Figure 5-29).

TE/TM Efficiencies

P1(7): 2.74404



TE/TM Efficiencies

P1(8): 2.78256 Microns

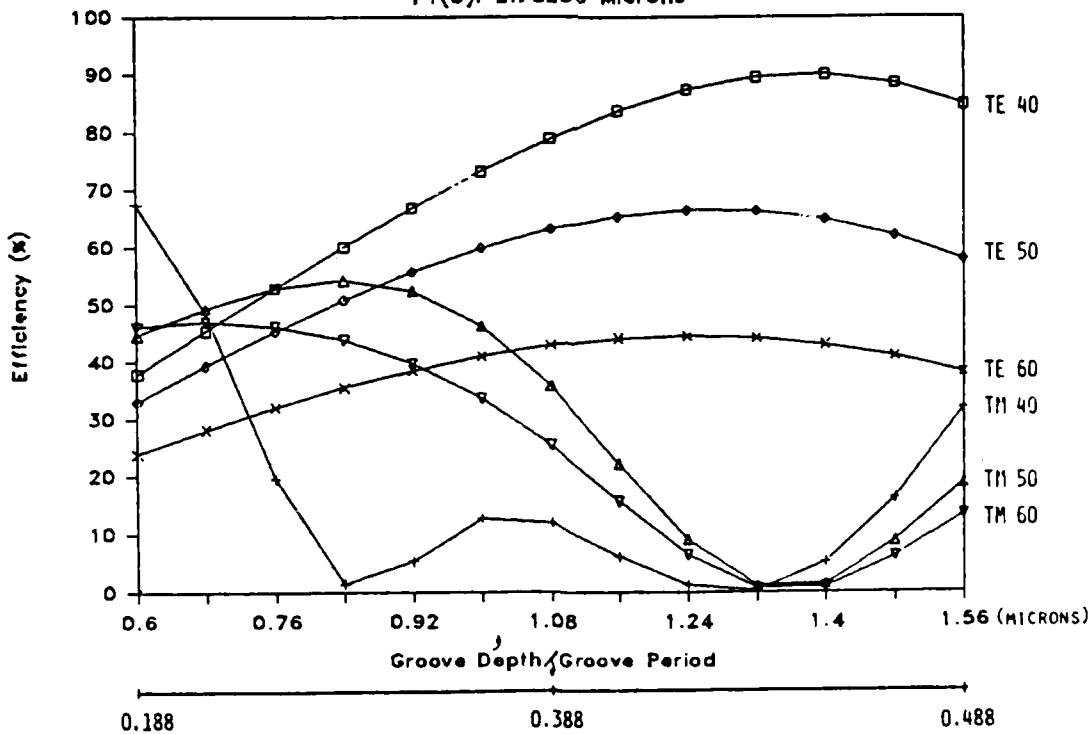


Figure 5-29. Lamellar groove first order grating efficiencies.

From these results it was necessary to address the problem of increasing the high power beam outcoupled efficiency. Study of the code outputs suggested that outcoupled efficiency could be enhanced by decreasing the angle of incidence. Also, earlier work for lamellar gratings plotting zeroth order TM versus the quantity $\lambda/\text{groove period}$ suggested that optimal output coupling could be achieved for a spread of wavelengths by keeping the quantity $\lambda/\text{groove period}$ between 0.64 and 0.71 (the results presented in the PALS PRR used $\lambda/\text{groove period}$ values between 0.86 and 0.91).

Therefore, a groove period value of 4.1 microns was chosen which yields a $\lambda/\text{groove period}$ between 0.67 to 0.71 for the four strong ALPHA lines and code runs for 20-degree incidence were performed. Figure 5-30 shows that a groove depth of 1.34 microns yields a high-power out-coupling efficiency off the TM zeroth order of 92 percent, an oscillator incoupling efficiency off the TE first order of 79 percent, and a TM first order return efficiency of 0.04 percent.

It is to be noted that the efficiency curves vary somewhat drastically with groove depth. This imposes strict fabrication tolerances on uniformity of groove depth over the active area of the grating.

In the course of choosing a grating for the CLPCT Oscillator Sub-system, a sinusoidal groove holographic grating (American Holographic) was found which was purported to have very high TE zeroth order efficiency (95%) and low TE first order efficiency on the grating code. Using a groove period of 1.67 microns (6001/mm) and incident angles of 55, 60, and 62 degrees (reasonable grating rhomb angles), the results shown in Figures 5-31 through 5-33 were obtained. For clarity, only the $P_1(7)$ and $P_2(8)$ line efficiencies are plotted; the $P_1(8)$ and $P_2(7)$ plots lie within the efficiency bands shown. First, it is noticed that the curves do not drop or rise precipitously as a function of groove depth as in the case of the lamellar curves. This is very desirable from the standpoint of fabrication tolerancing. Second, the angular alignment tolerance is large, on the order of several degrees. Third, shallow groove depths in these runs

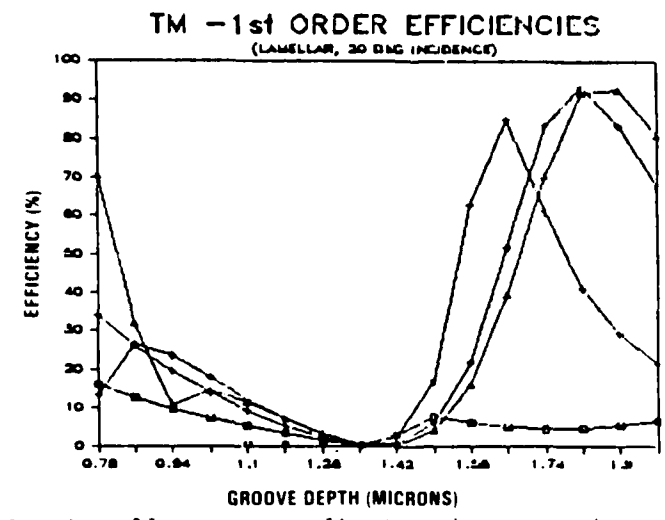
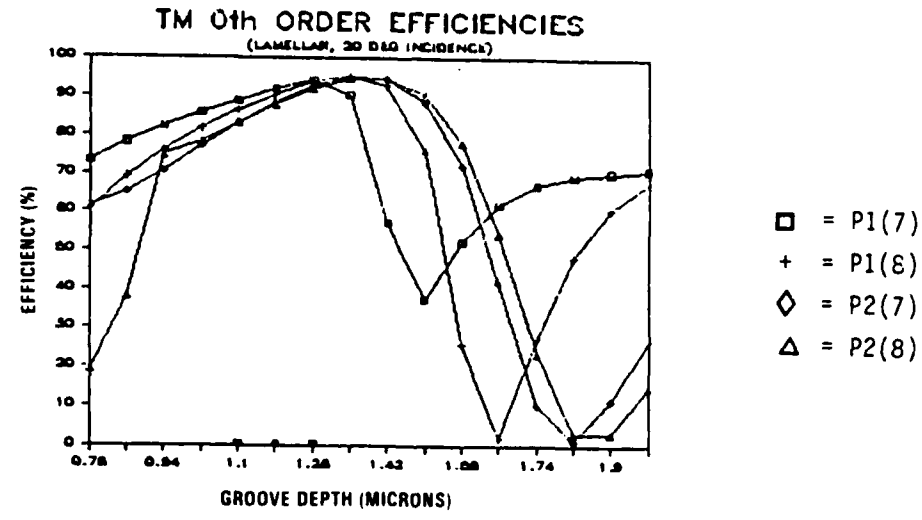
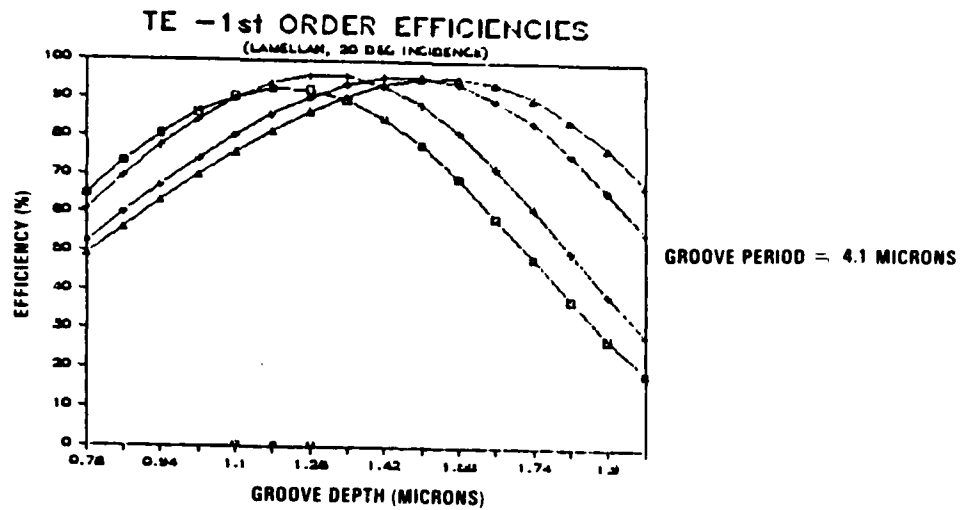


Figure 5-30. Lamellar groove first and zero order efficiencies.

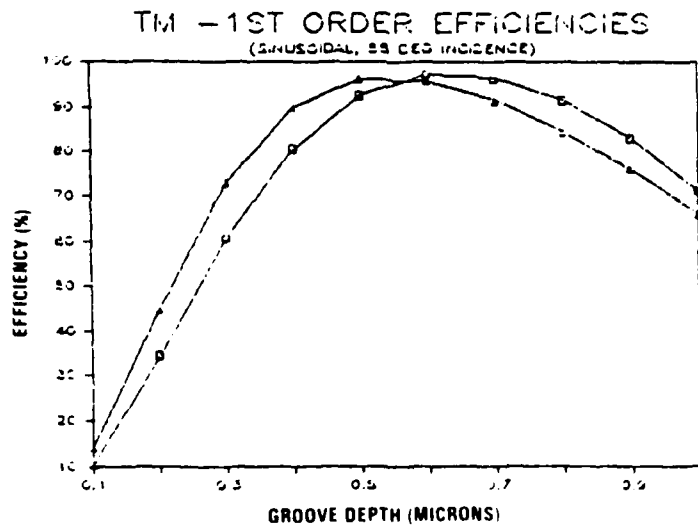
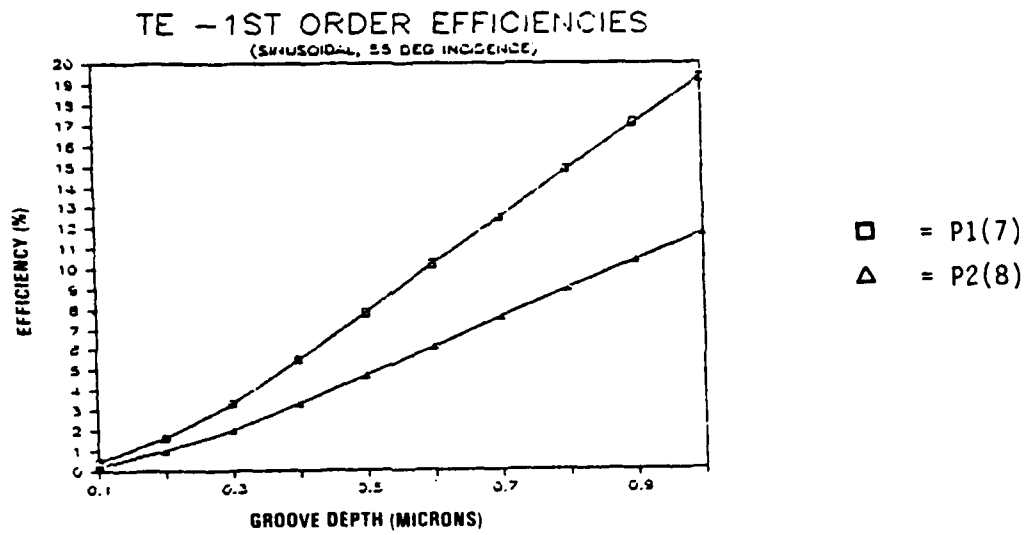
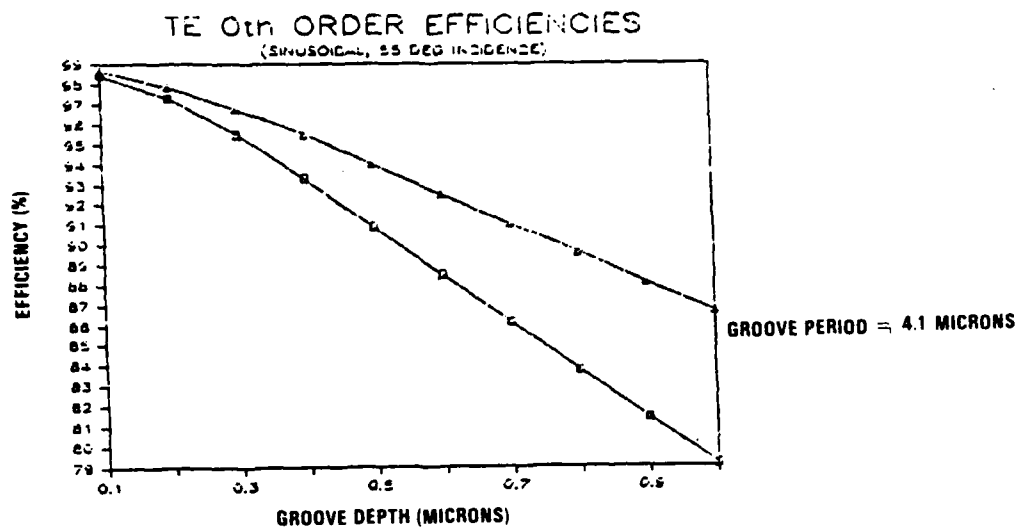


Figure 5-31. Sinusoidal groove first and zero order efficiencies.

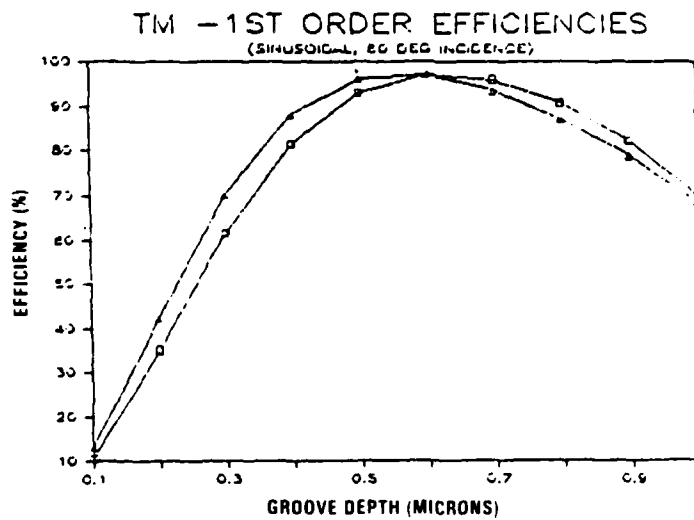
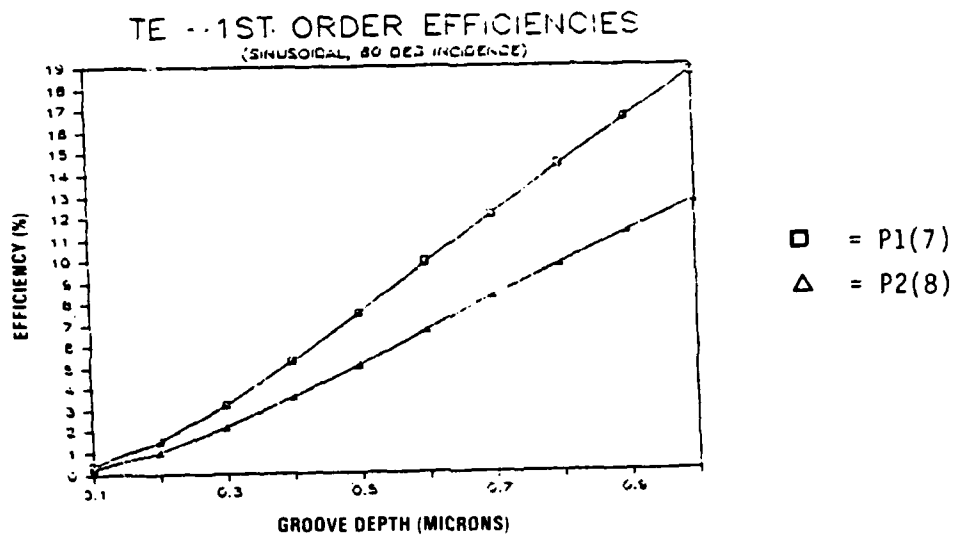
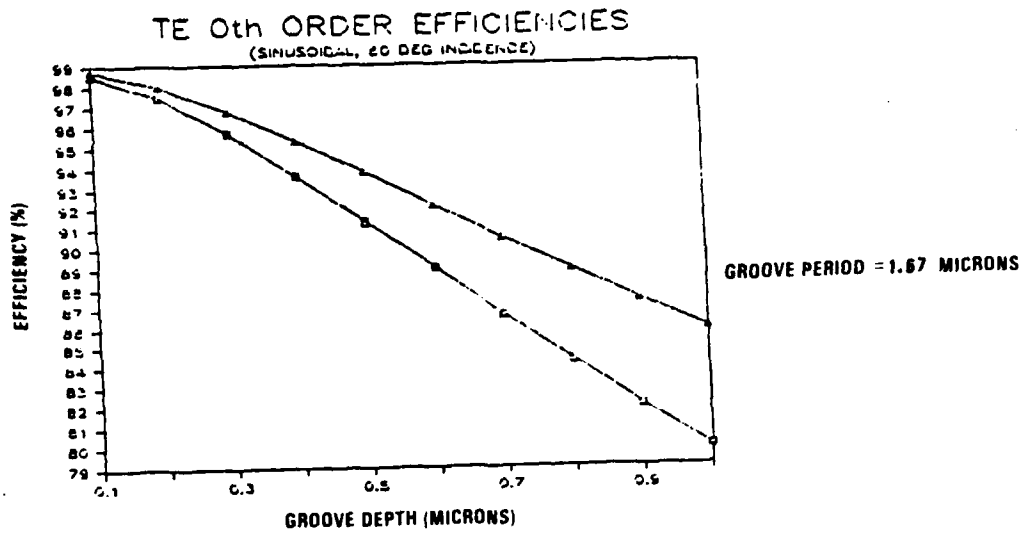


Figure 5-32. Sinusoidal groove first and zero order efficiencies.

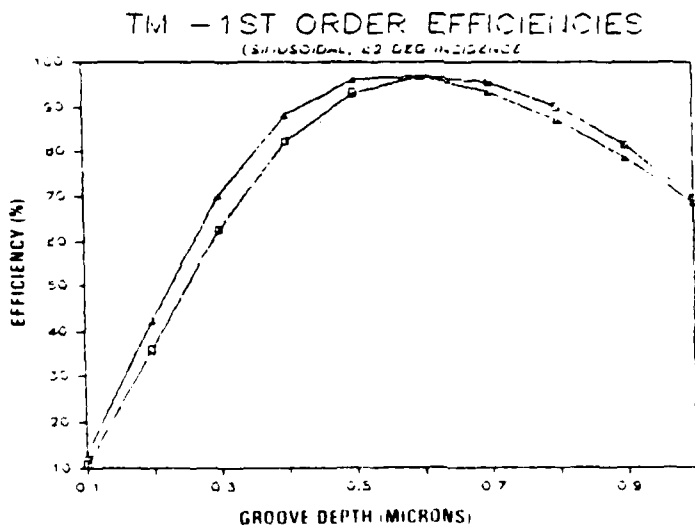
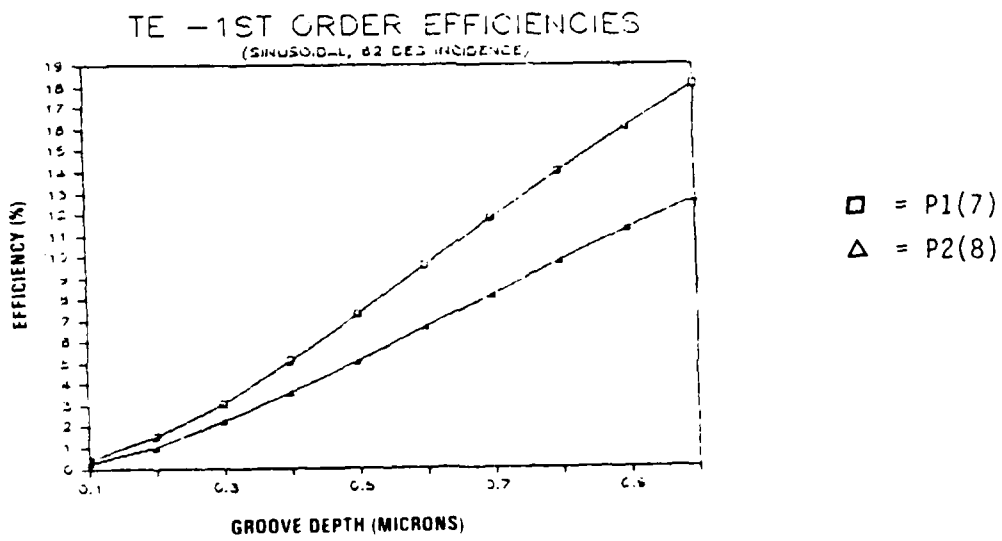
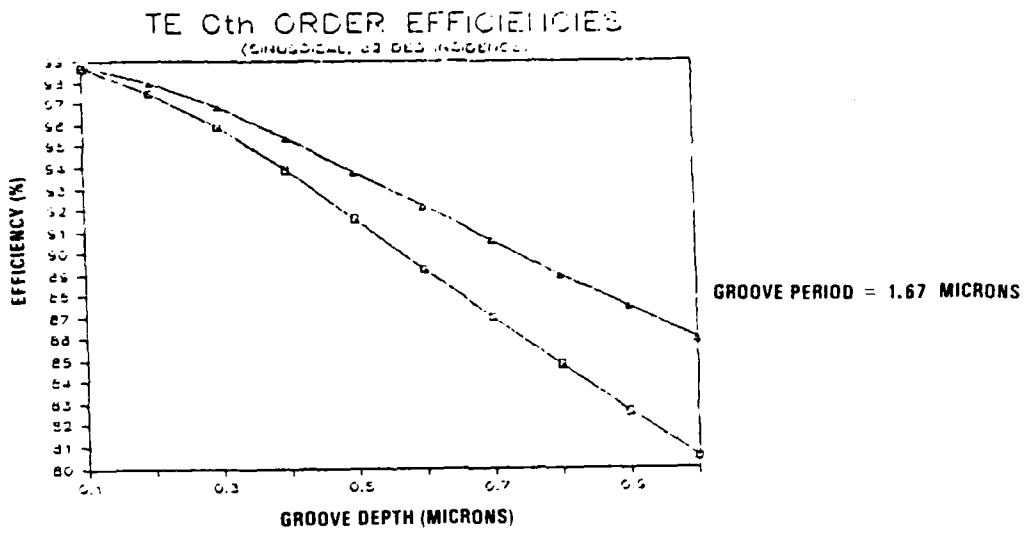


Figure 5-33. Sinusoidal groove first and zero order efficiencies.

enhance TE zeroth order outcoupled efficiency and minimize TE first order efficiency for the return beam, but at the expense of lower efficiency TM first order efficiency for the incoupled oscillator power (the remainder of the oscillator power being diverted to the TM zeroth order).

Table 5-5 shows expected rhomb performance for both lamellar and sinusoidal groove gratings. Values of grating efficiency have been squared to account for the rhomb configuration. The only exception is the high-power outcoupled beam which outcouples via the zeroth order of primary only.

An inexpensive sinusoidal test grating will be procured and characterized to verify the grating code predictions.

5.3.3 Grating Subscale Results

The basic materials procedure stated in the PALS PRR was used to study the effects of argon ion milling bare molybdenum, and nickel and gold coated substrates using the ALPHA master. The groove period of the master is 3.2 microns.

Deep ion etching bare molybdenum of nominal and good stock revealed an undesirable surface crazing. Previous work by others in deep-groove milling suggested that there would be processing problems with whisker formation, and this was found to be the case in working with nickel-coated substrates. Suggestions on how to remove the whiskers included ultrasoneration, ion milling the sample at grazing angle, and stripping the surface with a thin film setting agent (ex. collodian). Finally, several efforts were made to ion mill pure and 1 percent cobalt doped gold coated samples. In both cases, it was found that as groove depths of about 1 micron were approached, a surface mottling appeared indicating nonuniform surface milling.

5.3.4 Summary

The results of the study to assess performance and fabrication issues associated with use of a grating rhomb are summarized below.

1. The grating efficiency curves for the lamellar groove design vary precipitously with groove depth. This sets tight fabrication tolerances in groove depth uniformity. In addition, the subscale

TABLE 5-5. Requirements Versus Capabilities.

| Design Requirement | Design Goal | Lamellar Rhomb Capabilities (PRR) | Lamellar Rhomb Capabilities (PCR) | Sinusoidal Rhomb Capabilities (PCR) |
|--|---|-----------------------------------|-----------------------------------|--------------------------------------|
| Rhomb efficiency for incoupled oscillator beam | Greater than 90% (or sufficient to saturate the amplifier output) | 81% | 79% | 38% (must saturate amplifier output) |
| Rhomb efficiency for outcoupled high-power beam | Greater than 95% | 81% | 92% | 96% |
| Rhomb efficiency for orthogonal polarization return beam | Less than 5% | 0.04% | 0.04% | 0.09% |

effort in ion milling deep grooves (1-micron depth) indicates that there are materials control problems (surface crazing, whiskering, uneven milling) which need to be overcome.

2. The grating efficiency curves for a sinusoidal shallow groove design vary slowly with groove depth and incident angle. This translates into less stringent demands on fabrication of groove depth uniformity and system angle tuning. A sinusoidal test grating will be procured to verify efficiency performance over the spectral band of interest.

5.4 QUARTER-WAVE RETARDER STUDY

The objective of this effort was to evaluate coatings for the $P_1(7)$, $P_1(8)$, $P_2(7)$ and $P_2(8)$ laser lines that yield single-pass phase retardance of 90 degrees. The approach investigated was a double-bounce reflection per pass (Figure 5-34). The analyses studied were results from the McLeod Code (University of Arizona), and a propriety code of OCLI. The overarching physical requirements throughout this investigation were the use of phase retarding materials of proven high optical fluence damage, high reflectance at the wavelengths of interest, high resistance to

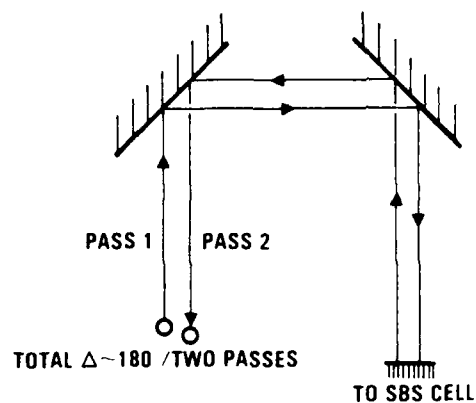


Figure 5-34. 90-deg retardance coating system.

abrasion, good adhesion characteristics, and good process controllability for uniform deposition, nominally 1 percent random thickness error per layer.

It should be noted that work is ongoing for 0-deg phase retardance coatings for ALPHA II under the NWC HF coatings program.

5.4.1 Discussion

Figure 5-35 shows a typical curve of phase shift versus wavelength for an incident angle of 45 degrees using a multilayer approach. "L" represents a relatively low refractive index materials such as sapphire; "H" represents a high refractive index material such as zinc sulfide; and "m" represents the number of layers of films, usually number 4-5. Both s and p polarizations have their own characteristics signatures. The high dispersion of the curves make this unacceptable for broadband applications.

Figure 5-36 shows the effect of changing the outermost layer to a low refractive index material on the phase retardance curve: the slope of the dispersion turns negative. When used together with a "positive" design such as in a double-bounce configuration, the net dispersion over the spectral band of interest can be significantly decreased.

Phase retardance curves for net 0-degree phase as a function of angle of incidence are shown in Figure 5-37. Curve A (angle of incidence = 50 degrees) is equivalent to what might be expected of a 90-degree phase

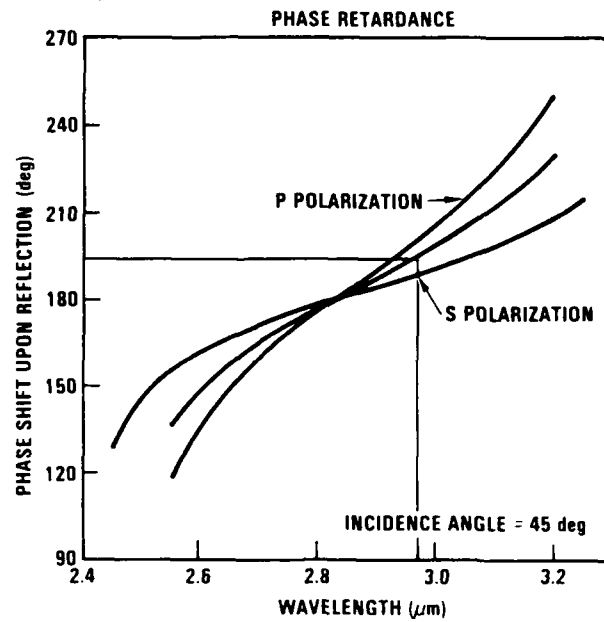


Figure 5-35. Phase shift upon reflection of a typical $(LH)^m$ enhanced reflector.

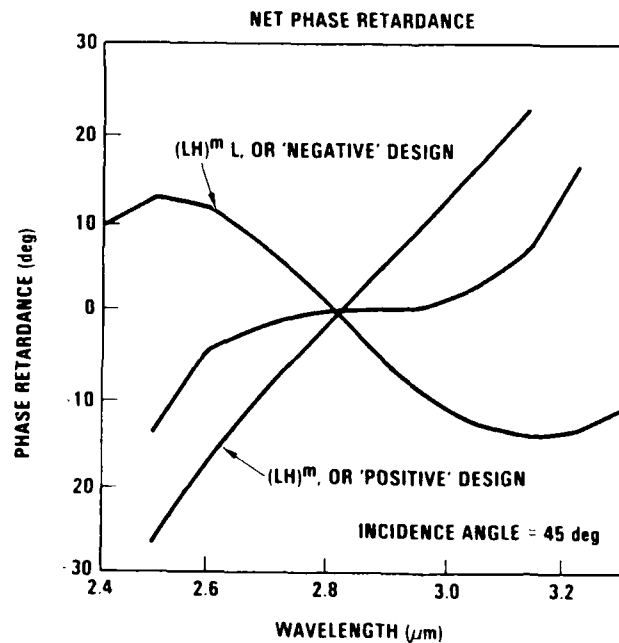


Figure 5-36. Phase compensating coatings.

AL2O3 AND ZNS: A01 40 deg, 45 deg, 50 deg

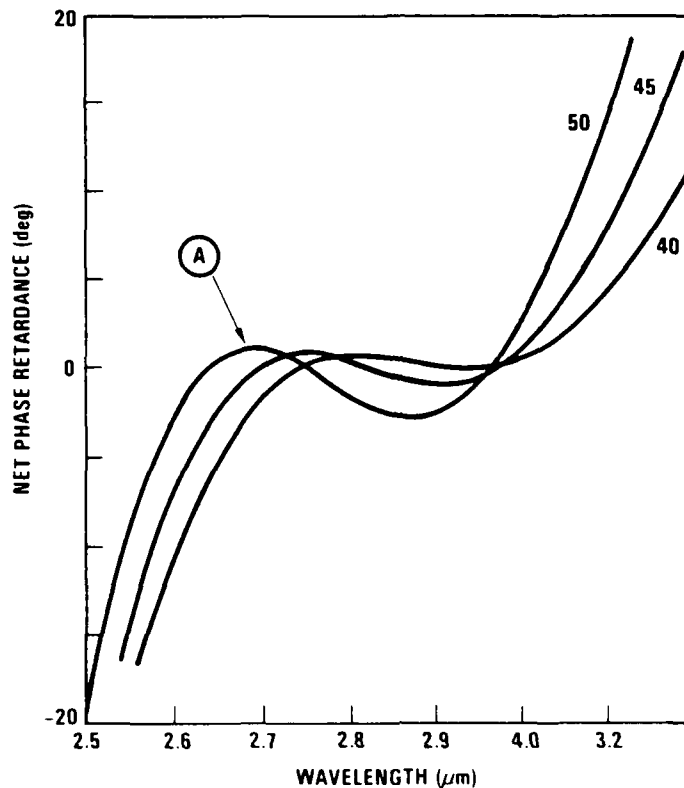


Figure 5-37. Preliminary results.

retardance curve. Thus, it is estimated that the bounce retardance error for a double-bounce single-pass retarder set would be about 6 degrees, or a round-trip retardance error of 12 degrees; that is, the return beam to the beam polarization isolator would be slightly elliptical with a power component in the orthogonal direction of about 1 percent back-propagating to the oscillator subsystem.

For the material currently used for the films, the mechanical coating resistance was rated to be moderate, and adhesion characteristics would conform to MIL-C-48497A (slow tape pull). The damage threshold for power fluence is TBD, however the estimate by material type indicates that it would be on the order of ALPHA I damage threshold. The average reflectance was estimated to be 0.992.

5.4.2 Summary

Practical 90-degree phase-retardance coating systems can be made with small dispersion. Damage threshold needs to be experimentally verified for high-power systems. Design goals for reflectance can be optimized for specific geometries and systems, i.e., angle of incidence and bandwidth. Coating designs are applicable to most HEXs by standard evaporation methods which will make the component lower risk.

6. BEAM DIRECTOR SUBSYSTEM

6.1 BEAM DIRECTOR PRELIMINARY CONCEPT AND TRADE ISSUES

6.1.1 Objective and Approach

The objective of the beam director design effort is to develop the analytical tools and approaches with which to generate a preliminary configuration that satisfies all the mission requirements and guidelines with minimum design complexity.

The approach was to first use geometrical ray traces for the initial beam director configuration, which would result in several candidate design approaches. Then the CODE V computer program was to be used to more accurately model and calculate the wavefront error induced by the candidate design approaches. This would allow selection of the design approach with lowest overall OPD for the required small angle pointing.

Another activity is to address the piston and tilt tolerances on the primary mirror segments by using a computer code to propagate the primary mirror piston and angular errors through the amplifier and SBS cell to determine allowable segment misalignment. Results from both analyses are presented in the following sections of this report.

The Beam Director Subsystem (BDS) represents a challenging design task because of the conflicting requirements for this subsystem. The BDS must provide the beam to targets within a single field of view with rapid retargeting capabilities, and yet must contribute small OPDs in the necessary off-axis pointing modes. Also, the BDS contribution to overall system jitter must be within budgeted requirements, and the beam obscuration must not exceed the required value. Also, the requirement affecting almost all aspects of the BDS design is the minimum brightness required of the overall system, which in addition to the issues just mentioned also affects aperture diameter, wavefront error, and mirror power handling requirements.

6.1.2 Beam Director Major Trade Issues

Several areas have been identified that require trade studies of candidate design approaches to meet the requirements. These issues are presented below.

6.1.2.1 Trade Issue: Primary Mirror f/Number

Relevant issues and comments: Separation distance between the secondary and primary mirrors affects structural and optical considerations. A longer secondary support structure is less stable than a shorter one, but primary mirror segment error requirements become easier at greater f/numbers. The baseline is 1.0-1.25.

6.1.2.2 Trade Issue: Beacon Separation Distance

Relevant issues and comments: The separation distance between the free-flying beacon mirror and the primary mirror affects both optical and pointing considerations. Larger separation distances result in easier primary mirror segment alignment tolerances, but the pointing accuracy and station keeping requirements are relaxed as the separation distance is decreased.

6.1.2.3 Trade Issue: Small-Angle Pointing Optics

Relevant issues and comments: Using a spherical primary and concentric (zero field) optics allows small-angle pointing with minimum OPD and obscuration. Actual pointing is accomplished by moving the secondary and tertiary mirrors around a common center of curvature, and removing the resulting tilt and decentration with two movable relay optics. The alternative is a wide field of view system that has significant off-axis pointing errors.

6.1.2.4 Trade Issue: Single or Dual Secondaries

Relevant issues and comments: The high and low power beams each must reflect off a secondary mirror, and this may be a common mirror or separate mirrors. A single secondary reduces obscuration and allows conjugation of secondary mirror jitter. Dual secondaries produce more obscuration and do not allow conjugation of jitter, but may yield more optical design flexibility. The baseline is a single secondary.

6.1.2.5 Trade Issue: Multisegment or Membrane Primary Mirror

Relevant issues and comments: A membrane mirror composed of lightweight material would offer weight and scaling advantages, but has not yet been proven feasible. A multisegmented glass mirror is the baseline

design, using identical segments no larger than the anticipated state-of-the-art manufacturing capability.

6.1.2.6 Trade Issue: Phase Conjugation of the Primary Mirror

Relevant issues and comments: Tolerances on primary mirror alignment error are reduced by two orders of magnitude through use of phase conjugation. Therefore this is the baseline approach, which has the added advantage of a beacon mirror that drastically improves the beam quality of the oscillator beam without spatial filters, since it must propagate a relatively long distance to reach the beacon. Figure 6-1 shows the significant relaxation of primary mirror segment alignment requirements as a result of phase conjugation as a function of beacon distance and f/number.

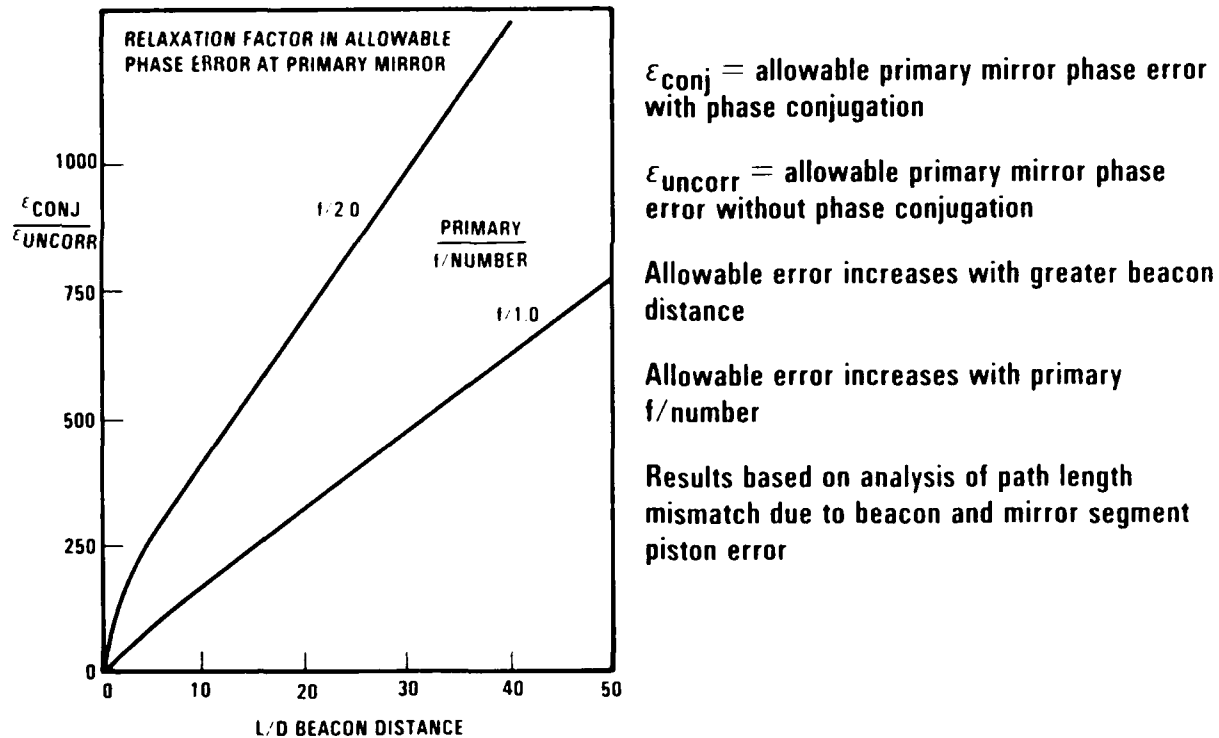


Figure 6-1. Conjugated primary yields significant relaxation of allowable primary segment error.

6.1.3 Beam Director Preliminary Configuration Summary

The beam director preliminary configuration, Figure 6-2, shows the schematic side view, the front view, and a view of the beacon. Initial CODE V analysis has shown that in order to keep off-axis pointing aberrations low, the magnification of the high power beam should be less than or equal to 10. The magnification is defined as the ratio of the output high power beam diameter to the diameter of the high power beam at the secondary mirror. Also, the f/number of the primary mirror should be greater than or equal to 1.0 to reduce off-axis pointing aberrations; beacon-to-primary separation distance of 20 times the primary diameter shows reasonable OPDs.

6.2 GEOMETRIC OPTICS MULTISEGMENT BEAM DIRECTOR SUBSYSTEM

6.2.1 Introduction to MICROCODE

The design, analysis, and tolerancing of phased array systems require the ability to accurately model large segmented optical surfaces composed of elements that may be individually tilted and decentered.

The primary lens design tool currently used at TRW is CODE V, a software package leased from Optical Research Associates. CODE V has the capability to analyze only systems containing monolithic continuous surfaces. It is a leased, fully protected program which cannot be modified by the individual user for unique situations. Because of this constraint, it was determined that TRW would have to develop its own analysis capability to accurately model optical systems containing segmented surfaces.

This software package is MICROCODE, a Modifiable Interactive Code for Research in Optics by Computer Optical Design and Evaluation. Its purpose was to provide an accurate, modifiable, analysis tool that could grow as needed. Currently MICROCODE consists of five main sections: (1) main program, (2) ray tracing, (3) analysis, (4) segmentation, and (5) wavefront calculation, which are described below.

6.2.1.1 Main Program

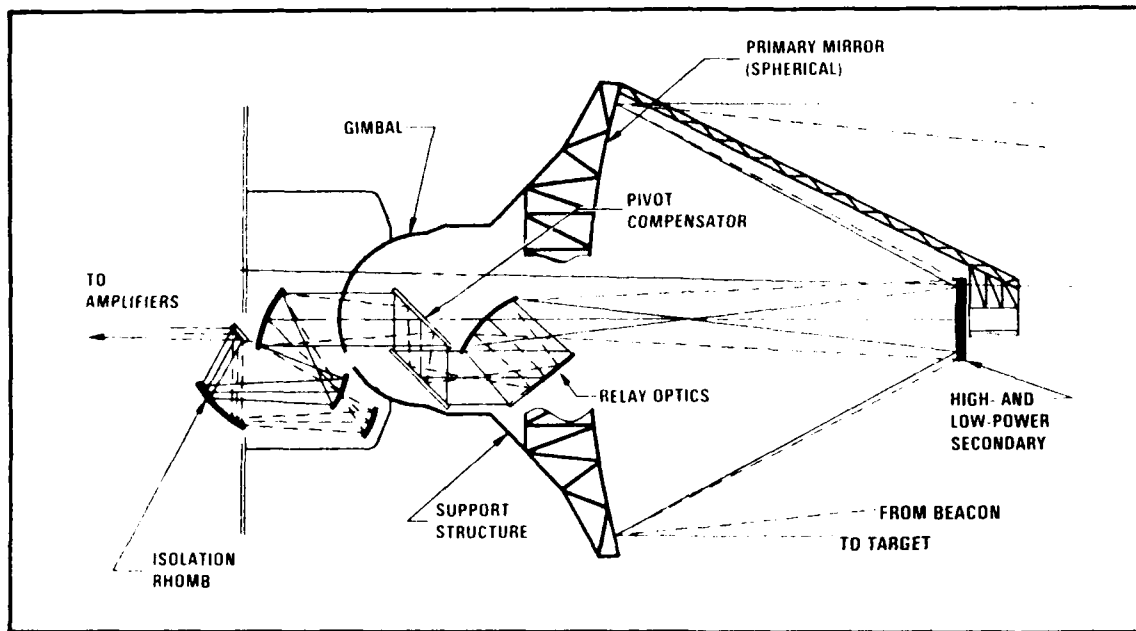
The syntax of MICROCODE has been kept as consistent as possible with CODE V. MICROCODE consists of a main program with many subroutines that carry out specific tasks. MICROCODE is a bottom-heavy code, that is complexity builds further down the program. Essentially top subroutines call more complex subordinate subroutines. The main program includes:

1. Data base and its management. There are two main data arrays: LENS and IPTR. LENS is the information array. While reading in surface information the indirect address of the value is saved in IPTR, with the actual value being stored in LENS. When working in optical design, information has to be readily accessed and modified. Indirect addressing was chosen because of the additional flexibility it provides.
2. Parser. This interprets user input for the program's use. The input is parsed for character and numerical information. MICROCODE can read information from terminal or disk.
3. System Setup. In this area of the program the optical system is set up. Refractive indices are determined for each surface of the system. MICROCODE has the capability of accepting either known glasses or special glass runs. This allows the user to exactly identify the refractive index in question. Also, if exact refractive index information is not available for a specific wavelength, MICROCODE can interpolate the given data to get the unknown index information.

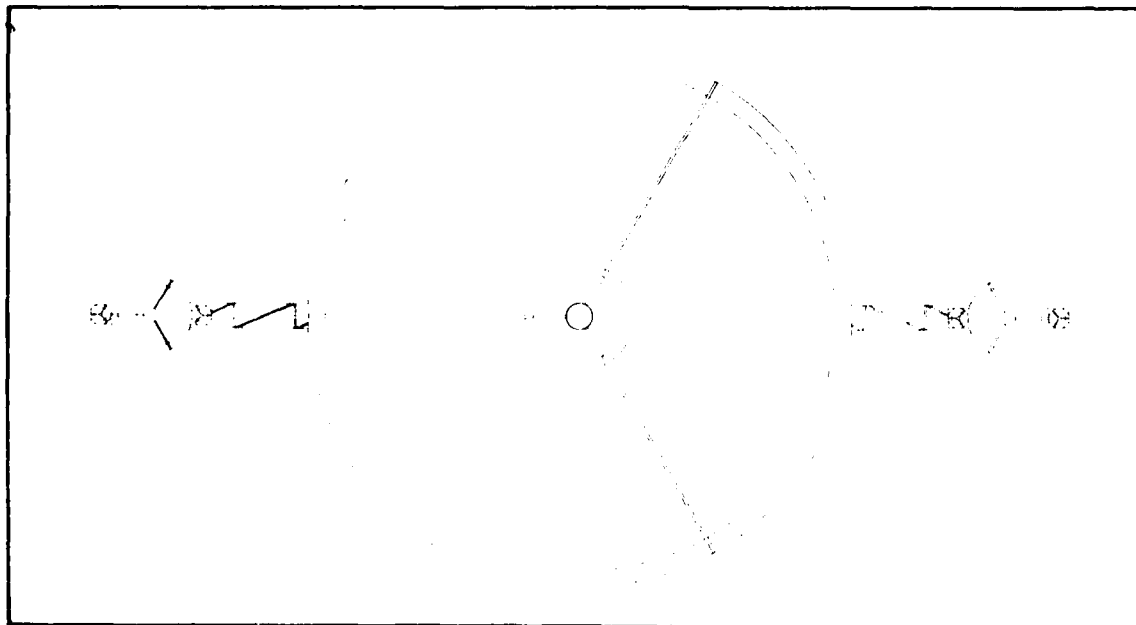
In setup the unknown parameters of the system are resolved. Any solves or pickups are numerically resolved and the determined information is placed in the LENS data array. Solves allowed in MICROCODE include marginal and chief ray angle solves; marginal and chief ray angle of incidence solves; marginal and chief ray aplanatic solves, paraxial chief and axial ray height solves; paraxial marginal ray solves at known thickness; and center of curvature solves. First order characteristics of the system are also determined, through a paraxial ray trace.

6.2.1.2 Real Raytracing

MICROCODE's real ray trace follows a general skew ray through the system. MICROCODE has the capability of ray tracing through the following types of surfaces: spherical, conic, toric (cylindrical), aspheric, anamorphic aspheres (nonrotationally symmetric), and phase conjugation assemblies.

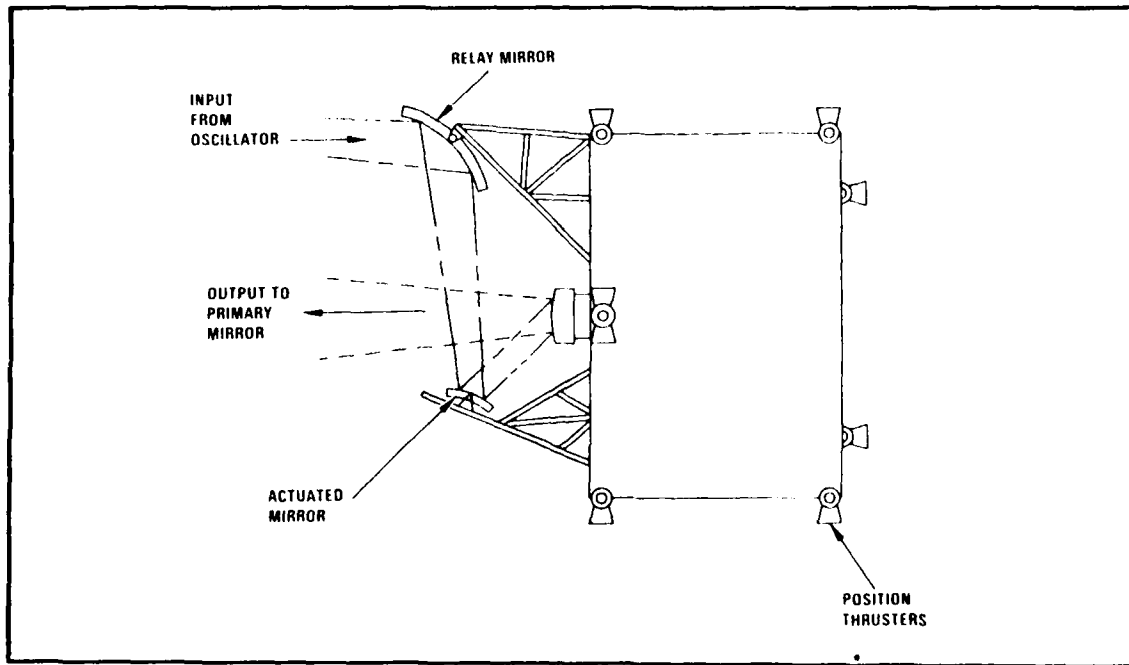


A. BEAM DIRECTOR - SIDE VIEW



B. BEAM DIRECTOR - FRONT VIEW

1072



C. BEAM DIRECTOR BEACON MIRROR

Figure 6-2. Beam director concept.

272

MICROCODE can also handle individual surface tilts and decenters. Each surface can have any combination of decenters in the x direction, x; decenters in the y direction, y; yz plane tilts, α ; xz plane tilts, β ; and xy plane tilts, γ .

Normally MICROCODE tilts and decenters in the following order (x,y, α , β , γ), following CODE V's convention. The user can determine how the tilts and decenters happen by specifying whether or not the coordinate system of the ray trace should change relative to the surface, and in what order the tilts and decenters should occur. Allowed forms of decentering are

1. The coordinate break to start a new coordinate system
(DECENTER)
2. The local coordinate breaks for one surface only
(DECENTER and RETURN)
3. The coordinate break to start a new coordinate system with operations in reverse order and sign (- γ , - β , - α , -y, -x)
(Ref. 6.1). (REVERSE DECENTER)

6.2.1.3 Analysis

The analysis section controls the geometrical performance evaluation of an optical system. The analysis section can give any or all of the following information: first order system properties, single ray traces, ray traces of "fans" of rays, paraxial aberration data, and surface-by-surface printouts of real ray coordinates and angles.

6.2.1.4 Segmentation

At this time the user can define up to two segmented surfaces per optical system. Each of these segmented surfaces can have up to 100 individually defined segments. Each segment is defined by its radius, x and y coordinates, and its tilts and decenters. Tilts and decenters are defined the same as in the main real ray tracing subroutines, except now there is the freedom to include piston errors, or z direction decenters. Editing of the segment information can occur interactively as the program runs.

The segmented surface ray trace controls the matrix transformations necessary to accurately ray trace through a segmented surface and is fully integrated into the real ray tracing algorithm. The procedure to ray trace through a segmented surface includes identifying with which segment a ray will intersect, applying the necessary coordinate transforms to perform that element's tilts and decenters, ray tracing through the element, and, finally, reestablishing the coordinate system of the rest of the optical train.

6.2.1.5 Wavefront Calculation

The optical path difference algorithm is based on work originally done by H. H. Hopkins in 1952, and later modified by Josef Meiron. This OPD calculation is fully integrated into the ray trace routines, and is done automatically for every ray traced. At this time MICROCODE only performs single ray OPD calculations.

6.2.1.6 Future Plans

The planned expansion for MICROCODE includes adding further wave optical evaluation tools: OPD wavefront mapping, rms wavefront error calculations, determination of the Strehl ratio, calculation of the diffraction based image of a point object (point spread function), and calculation of the frequency response of an optical system (MTF).

6.2.1.7 Summary

When complete, MICROCODE will enable accurate prediction of the performance of systems containing segmented surfaces and phase conjugation assemblies.

6.2.1.8 System Modeled

The system modeled consisted of an elliptical primary and two independent aspheric secondary mirrors. There was a 12 to 1 ratio of the diameters of the secondaries and the primary mirrors. The wavelength used was 2.8 microns.

Light fills the elliptical primary from a point source located 12 times the diameter of the primary away, it is then reflected down to an aspheric low-power secondary mirror, and enters the phase conjugation

assembly. After exiting the phase conjugation assembly, the light impinges on the high power secondary where it expands to once again fill the primary mirror, and then exits the system collimated.

6.2.1.9 System Results

Phase conjugation improves the system's performance. However, when the same point is not struck twice on the primary mirror, degradation in performance occurs, simply because piston error has not been fully cancelled by phase conjugation. The results support and reinforce results found through the use of IPAGOS and CODE V. Phase conjugation will improve the performance of the systems under study but only to the point of ray matching on the segmented primary mirror.

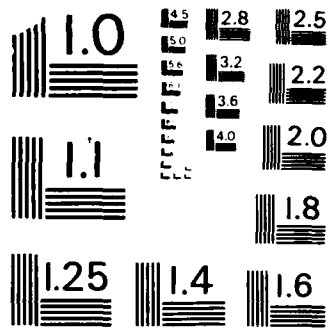
Using MICROCODE three-dimensional plots of the OPD, Figures 6-3 and 6-4, were created for the case in which one segment has a piston error of one wavelength. Figure 6-3 shows the plot with the phase conjugation mirror in place, while Figure 6-4 shows the plot with a plane reflecting mirror instead.

6.3 WAVE OPTICS ANALYSES OF MULTISEGMENT BEAM DIRECTOR SUBSYSTEM- MULTISEGMENT BEAM DIRECTOR MISALIGNMENT ANALYSIS

This analysis was performed to determine the sensitivity of beam quality of the beam director output to misalignment of the primary mirror segments, as a function of beacon location and telescope f/number, using a three-dimensional wave optics calculation. The sources of beam quality degradation are assumed to be solely from the beam director telescope itself and optical path differences between the low- and high-power beams. In addition, a two-dimensional wave optics code was to be used to provide a simulation of actual fields at the entrances to the amplifiers and phase conjugator. These fields, used in conjunction with other codes which model amplifier and SBS cell operation, determine additional limits on segment misalignments based on conjugation fidelity.

6.3.1 The Model

The source of the field into the telescope is assumed to be a point source (beacon) located at a variable distance from the primary and along its axis. The field from the beacon is intercepted by the segmented



MICROCOPY RESOLUTION TEST CHART
NATIONAL BUREAU OF STANDARDS-1963-A

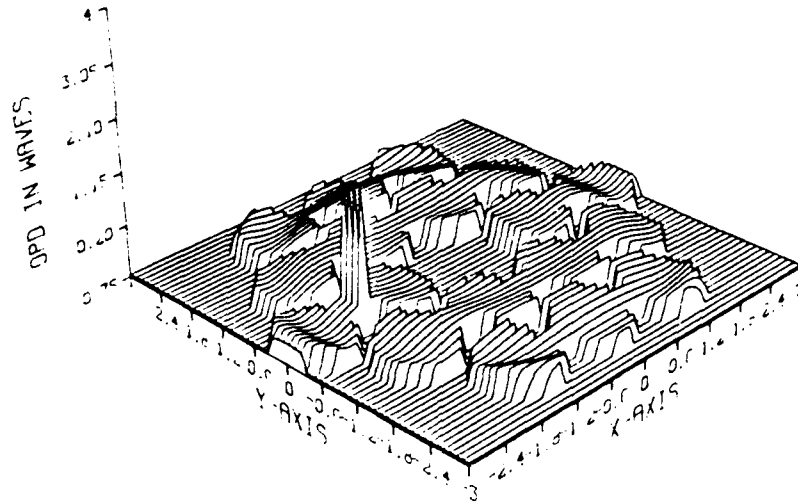


Figure 6-3. Wavefront plot at far field with one segment having piston error of 1 wavelength - phase conjugation mirror.

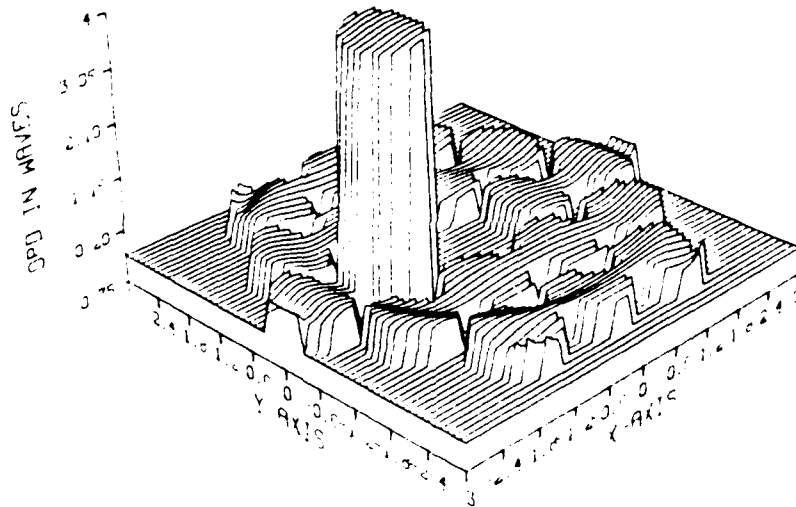


Figure 6-4. Wavefront plot at far field with one segment having piston error of 1 wavelength - ordinary mirror.

primary, focused, and then is collimated by the low-power secondary and passed into the optical system behind the primary mirror. The entire optical train from the secondary to the phase conjugator is assumed, in this model, to add no aberrations to the field and to contain no limiting apertures. Wave optics propagation through all the optical elements in the train can then be described by a single equivalent propagation step through an effective distance dependent on the magnifications and separation of the elements in the train. The phase conjugator itself is assumed to be perfect with no clipping of the field. A second optical train - not necessarily identical to the first - is traversed from the phase conjugator to the high power secondary where the beam is remagnified to fill the misaligned primary and produce a collimated output beam. At this point the beam quality is evaluated by focusing the output beam and integrating the intensity over a square bucket of width equal to the distance between the first nulls at the focus of a uniform field filling a perfectly aligned primary mirror. The ratio of the power in the bucket of the ideal system to that of the misaligned system is the beam quality number.

The primary and secondary mirrors are assumed to be circular paraboloids. While the actual mirrors will probably not be exactly paraboloidal, the differences are not expected to be of great importance in affecting segment misalignment sensitivity. Using the Fresnel-Kirchhoff integral representation of the physical optics field, together with the preceding assumptions, allows the (high-power) field leaving the primary to be evaluated analytically. Were this not the case, numerical integrations would be required to propagate the field through the optical system and, considering the very large Fresnel numbers involved in the propagation steps, would result in a problem much more difficult to solve to the required degree of accuracy. (A numerical propagation method would, however, have the advantage of greater flexibility - for example, in permitting arbitrary aberrations to be introduced within the optical system.) Mathematical details of the model and the derivation of the equations may be found in Section 6.3.1.1.

The primary mirror is represented by an array of contiguous segments whose projections in the x-y plane (i.e., the plane normal to the optic

axis) are squares. The array is truncated at the corners so as to have an approximately circular projection. The present "standard" configuration is an array of seven rows and columns with three segments removed from each corner, for a total of 37 segments. The permitted misalignments of each segment are any combination of independent tilts about each of two perpendicular axes through its center and a piston error, or rigid displacement parallel to the normal to the surface. For perfectly aligned mirror segments and a hypothetical optical system for which low- and high-power beams travel identical paths, the output beam will be collimated and the beam quality, by definition, will be 1. That is, the phase conjugator will return a field to each segment which precisely reverses all diffraction effects suffered on the in-bound path, and a perfect output beam results. (In the Fraunhofer zone each of the segments has a diffraction-limited spot size of λ/w , where w is the width of a segment, but with a phase dependent on the position of each segment. For the perfect system, however, the phases of the segment fields are such that the net field has a much smaller diffraction-limited spot size of approximately λ/D , where D is the diameter of the primary mirror. The energy within the smaller spot is used as the measure of beam quality.) In general, however, the beacon will be a finite distance from the primary mirror and the low- and high-power secondaries will be located at different distances from the primary; in addition, the paths in and out of the remaining optics may not be quite identical. Thus the field returning to the primary from the phase conjugator will not quite reverse the diffraction effects suffered on the inward path, and the high-power field returning to a particular segment will experience some diffractive spreading and "spillover" onto adjacent segments. If there are no misalignments of the segments, the field lost to one segment is precisely compensated by a gain from the diffractive spillover onto it from adjacent segments, except, of course, for segments at or near the outer edge of the primary which suffer a net loss. Accordingly, the intensity at the focus of the primary will be reduced and the beam quality number will be somewhat greater than 1.0, even for perfectly aligned segments. The diffraction effects are characterized by a propagation Fresnel number dependent on a net effective propagation distance related to the differences in optical paths of the low- and high-power

beams. Thus if the paths were identical, this Fresnel number is infinite, implying that the diffraction effects vanish.

Suppose now that the segments have random tilt misalignments. The phase-conjugated field which returns to the particular segment that it encountered on its inbound path will have a phase which compensates for the tilt of that segment. The diffractive spillover onto adjacent segments will be uncorrelated in phase with the actual tilt of the adjacent segment, resulting in a nonzero net tilt of the portion of the field diffracted onto adjacent elements. This field, when focused, then shifts away from the axis and the beam quality number increases. As the segment tilt increases, the value of BQ increases until all the diffracted spillover fields are effectively removed from the central focal spot, at which point the curve of BQ versus tilt angle becomes relatively flat.

Another effect of segment tilt is simultaneously occurring, however, due to the difference in optical paths of the low- and high-power beams. Since the phase-conjugated field of a segment travels a different distance than the incoming field, there will be a net displacement of the beam. Once again, a spillover of the field to neighboring segments occurs and that portion of the field is lost to the focal spot in the far field. In contrast to the diffraction effect, the beam quality degradation caused by the geometric shifting of the beams continues to increase with increasing segment tilt angle.

Quite similar behavior occurs for the case of segment piston error. The portion of the field leaving a segment that becomes diffractively coupled to adjacent segments on its return path has a conjugated phase which is uncorrelated with the piston error of the segment it actually encounters. The resulting phase aberration will quickly remove the spillover field from the central focal spot as segment piston error increases from zero. In addition, even the phase conjugated field which returns to its segment of origin will incompletely compensate for the segment piston error. This is because the phase change in the field reflected from a segment displaced in the direction of its normal depends on the direction of the ray reaching the surface. As long as the beacon is at a finite distance from the mirror the low-power input field and the

phase-conjugated output field will reach a point on the segment at different angles, with the result that a net uncompensated piston error and a consequent degradation in beam quality will remain. Consideration of the relative positions of the beacon and the low- and high-power secondaries suggests that beam quality will worsen for shorter beacon distance from the primary and for lower f/numbers. In contrast, the diffractive spillover effect on beam quality degradation will diminish with lower f/number.

6.3.1.1 Three-Dimensional Propagation Equations

Equations are developed in this section describing the propagation of a field, originating as a point source at the beacon position, to the segmented primary, the low-power secondary, through an optical train to the phase conjugator; the return path from the phase conjugator is through a second optical train, not necessarily identical to the first, to the high-power secondary, the segmented primary, and then out of the system as a collimated beam. Figure 6-5 is a schematic diagram indicating an equivalent lens train for the round trip path. The direction of propagation is taken to be the z direction and the x and y axes lie in a plane transverse to z. Each propagation step is described by the Fresnel approximation to the Fresnel-Kirchhoff equation. The operations to be performed at each step are enumerated below.

Step 1. Field at primary mirror due to point source a distance L_0 from the primary

$$E_{PM}(x,y) = \frac{jk}{2\pi L_0} \int_{-\infty}^{\infty} dx' \int_{-\infty}^{\infty} dy' \exp\left\{-\frac{jk}{2L_0} [(x-x')^2 + (y-y')^2]\right\} \delta(x',y') E_0$$

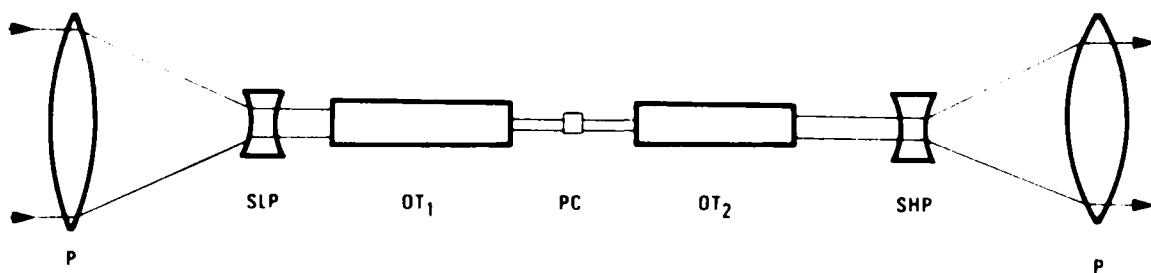


Figure 6-5. Equivalent lens train.

where E_0 is an arbitrary constant amplitude of the source, $\delta(x,y)$ is the Dirac delta function, $k = 2\pi/\lambda$, and $j = \sqrt{-1}$. Thus the field at the primary is

$$E_{PM}(x,y) = \frac{jkE_0}{2\pi L_0} \exp\left\{-j \frac{k}{2L_0} (x^2 + y^2)\right\}.$$

Note that the sign convention being used corresponds to an $\exp(+j\omega t)$ time dependence to the field.

Step 2. Apply the primary mirror aberration function $S(x,y)$. The function S represents the OPD variations due to the misalignments (tilt, piston error) of the primary mirror segments. This function multiplies E_{PM}

$$E'_{PM}(x,y) = E_{PM}(x,y) S(x,y)$$

The explicit form of S will be described later.

3. Reflect off the primary mirror. The primary mirror is assumed, for purposes of the misalignment sensitivity study, to be a portion of a circular paraboloid. Thus the field E'_{PM} , when reflected by the mirror, is multiplied by a phase factor to give E''_{PM} :

$$E''_{PM}(x,y) = E'_{PM}(x,y) \exp\left\{j \frac{k}{2F_p} (x^2 + y^2)\right\}$$

where F_p is the focal length of the primary.

Step 4. Propagate a distance L_1 to the low-power secondary

$$E_S(x,y) = \frac{jk}{2\pi L_1} \iint E''_{PM}(x',y') \exp\left\{\frac{-jk}{2L_1} [(x-x')^2 + (y-y')^2]\right\} dx' dy'$$

where the integration extends over the area of the primary projected onto the x,y plane.

Step 5. Reflect from the low-power secondary.

$$E_S'(x,y) = E_S(x,y) \exp \left\{ \frac{jk}{2F_{SLP}} (x^2 + y^2) - jk(\theta_{SLP}^x x + \theta_{SLP}^y y) \right\}$$

where the secondary (assumed to be paraboloidal with focal length F_{SLP}) is allowed to have small tilts of θ_{SLP}^x , θ_{SLP}^y about the y and x axes, respectively. F_{SLP} is to be chosen so that the field leaving the secondary is collimated; thus it is determined by F_p , L_1 , and L_0 . According to the sign convention $F_p > 0$, $F_{SLP} < 0$.

Step 6. Propagate through an optical train to the phase conjugator. The optical train may be made up of many elements whose total effect on any ray is assumed to be representable by a ray matrix of the form

$$\begin{pmatrix} A & B \\ C & D \end{pmatrix} = \begin{pmatrix} M_T & B_T \\ 0 & M_T^{-1} \end{pmatrix}.$$

In other words, the collimated input beam is also collimated at the phase conjugator, and the beam is magnified by M_T on passing through the train. The same ray matrix is assumed to apply to both x and y coordinate variables. Physical optics propagation through such an optical train is described by the integral

$$E_{PC}(x,y) = \frac{jk}{2\pi B_T} \iint_{-\infty}^{\infty} E_S(x',y') \exp \left\{ -j \frac{kM_T}{2B_T} [(x' - x/M_T)^2 + (y' - y/M_T)^2] \right\} dx' dy'$$

provided there are no limiting apertures in the optical train. It is assumed that the system would be designed with minimal beam aperturing in order for the output field to most closely represent the conjugate of the input field.

Step 7. Phase conjugate. For purposes of this model the phase conjugator is assumed to be perfect, so that its effect is simply

$$E'_{PC}(x,y) = E_{PC}^*(x,y).$$

Step 8. Return to the high-power secondary through an optical train described by the ray matrix

$$\begin{pmatrix} A & B \\ C & D \end{pmatrix} = \begin{pmatrix} 1/M_T & B'_T \\ 0 & M_T \end{pmatrix}$$

M_T is the same magnification as for the optical train in step (6); the effective propagation distance, B'_T , may be different from B_T . The propagation integral for this step is

$$E_S(x,y) = \frac{jk}{2\pi B_T} \iint_{-\infty}^{\infty} E'_{PC}(x',y') \exp\left\{-j \frac{k}{2B_T M_T} [(x'-M_T x)^2 + (y'-M_T y)^2]\right\} dx' dy'$$

Step 9. Reflect off high-power secondary as in step (5),

$$E'_S(x,y) = E_S(x,y) \exp\left\{j \frac{k}{2F_{SHP}} (x^2 + y^2) - jk(\theta_{SHP}^x x + \theta_{SHP}^y y)\right\}$$

where $F_{SHP} < 0$ and is determined by the magnification of the beam director telescope and the condition that the output beam be collimated.

Step 10. Propagate from the high-power secondary to the segmented primary. If the two mirrors are separated in z by a distance L_2 , then

$$E_{PM}(x,y) = \frac{jk}{2\pi L_2} \iint_{-\infty}^{\infty} E'_S(x',y') \exp\left\{-\frac{jk}{2L_2} [(x-x')^2 + (y-y')^2]\right\} dx' dy'$$

Step 11. Reflect from the primary and apply the primary mirror aberration function

$$E_{PM}'(x,y) = E_{PM}(x,y) S(x,y) \exp \left\{ \frac{jk}{2F_p} (x^2 + y^2) \right\}$$

This last function, E_{PM}' , represents the field leaving the beam director. Since the objective is to evaluate beam quality, this field is to be focused and power-in-the-bucket in the focal plane calculated. This procedure will be described later.

Now consider the primary mirror segment aberration function $S(x,y)$. Figure 6-6 is a diagram of the projection onto the x-y plane of the mirror segments. The mirror is made up of an array of segments in, for example, seven rows and columns, with three segments in each corner removed so that the entire array is roughly circular. (The actual number of segments is an input variable to the code.) To simplify the calculations the segments are assumed to have identical square projections on the x-y plane, each square having a side of length w . The center of each square has coordinates (x_{oi}, y_{oi}) , $i = 1, \dots, NS$, where NS is the number of segments. If the m^{th} segment suffers small tilts about the y axis through its center of θ_{Tx}^m and of θ_{Ty}^m about the x axis through its center, then the OPD change of a field reflected from the segment corresponds approximately to multiplying the field by

$$S_m^T(x,y) = \exp \left\{ -jk2 \left[\theta_{Tx}^m (x - x_{om}) + \theta_{Ty}^m (y - y_{om}) \right] \right\}$$

where (x,y) is a point on the m th segment.

For the case of a piston error of the m th segment the OPD change suffered by a field reflected from the segment depends on the direction of the ray onto (or leaving) the surface (Figure 6-7). The path length change ΔL is

$$\Delta L = 2p_m \cos \theta$$

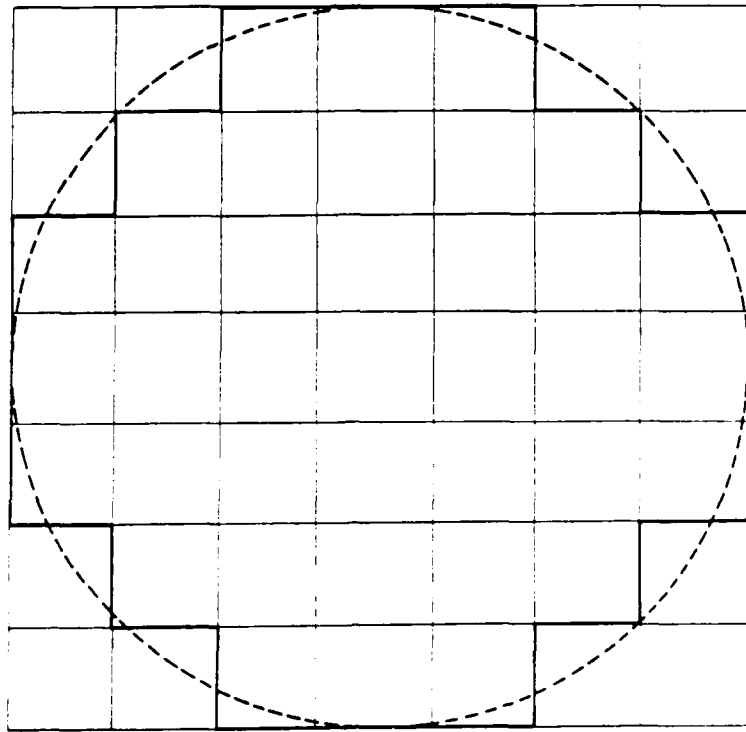


Figure 6-6. Projection of segmented primary.

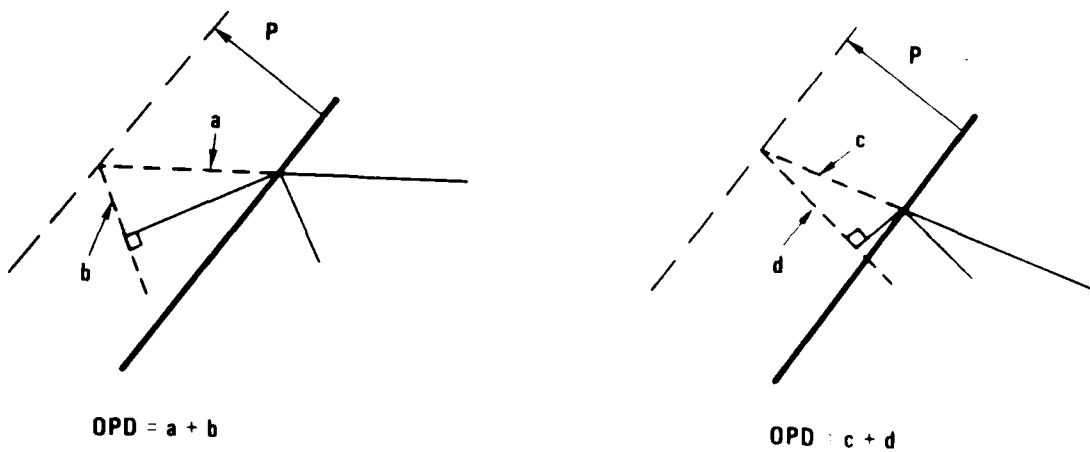


Figure 6-7. Ray angle dependence of OPD due to piston error.

where p_m is the displacement of segment m and θ is the angle between the surface normal and the ray onto, or leaving, the surface. If the ray direction is specified by the line joining the point (x,y) with a point on the z axis a distance L in front of the mirror, then for a paraboloidal mirror of focal length F_p , it may be shown that

$$\cos\theta = 1 - (x^2+y^2)/8F^2$$

where

$$F = F_p/(1 - 2F_p/L).$$

To account for the phase change in a field reflected from a segment with piston error, multiply by the factor

$$S_m^P(x,y) = \exp\{-jk2p_m[1 - (x^2+y^2)/8F^2]\}$$

where (x,y) is a point on the m th segment. The total aberration function for the surface is

$$S(x,y) = \sum_m S_m(x,y)$$

where the sum is over all segments, and

$$S_m(x,y) = \begin{cases} S_m^T(x,y) S_m^P(x,y), & \text{if } (x,y) \text{ is on the } m\text{th} \\ & \text{segment} \\ 0, & \text{otherwise.} \end{cases}$$

This function $S(x,y)$ is the function that appears in Steps 2 and 11 above, although its value differs in the two cases. In Step 2 the source point for a ray is at $L = L_0$ (the beacon position) while in Step 11 the rays

leaving the primary are collimated so that $L = \infty$. In the former case the quantity \bar{F} appearing in $S(x,y)$ is $\bar{F} = F_p/(1-2F_p/L_0)$ while in the latter case it is $\bar{F} = F_p$. Note also that the function $S_m(x,y)$ is separable in x and y , although $S(x,y)$ is not.

The operations as prescribed in Steps 1 through 11 may now be carried out. At each step an interchange in order of integration is required; each integrand contains complex exponentials whose exponents are at most quadratic in the integration variables so that the integrals may be evaluated explicitly. After considerable algebra the field leaving the primary mirror from the ℓ th segment is obtained in the following form:

For (x,y) on segment ℓ local coordinates (ξ_ℓ, η_ℓ) are introduced relative to an origin at the center of the segment; i.e., $x = x_{0\ell} + \xi_\ell$, $y = y_{0\ell} + \eta_\ell$, where $-w/2 \leq \xi_\ell, \eta_\ell \leq w/2$. The field leaving the primary from segment ℓ is

$$E_p^{(\ell)}(x,y) = CR_{1x}^\ell R_{1y}^\ell \sum_{i=1}^{NS} R_{2x}^{\ell i} R_{2y}^{\ell i} \exp \left[jk \left(\Omega_x^{\ell i} \xi_\ell + \Omega_y^{\ell i} \eta_\ell \right) \right] \\ \times \phi_x^{i\ell}(\xi_\ell) \phi_y^{i\ell}(\eta_\ell)$$

where all superscripts are indices and not exponents. The terms appearing in this expression are

$$R_{1x}^\ell = \exp \left\{ -jk \left[\frac{1}{M_S} (\theta_{SHP}^x - \theta_{SLP}^x) x_{0\ell} + p_\ell (1 - x_{0\ell}^2 / 4F_{p0}^2) \right] \right\}$$

$$R_{2x}^{\ell i} = \exp \left\{ jk \left[p_i (1 - x_{0\ell}^2 / 4F_p^2) + 2(x_{0\ell} - x_{0i} - q_x) \theta_{Tx}^i \right] \right\}$$

$$\left[1 - \frac{M_S}{M_T} (\alpha_1 - \alpha_2) p_i / 2F_p^2 \right] \left\{ \right.$$

$$\Omega_x^{\ell i} = \frac{p_\ell x_{0\ell}}{2F_{p0}} - 2\theta_{Tx}^\ell - \frac{1}{M_S} (\theta_{SHP}^x - \theta_{SLP}^x) + \left[-\frac{p_i x_{0\ell}}{2F_p} + 2\theta_{Tx}^i \right] /$$

$$\left[1 - \frac{M_S}{M_T} (\mathcal{L}_1 - \mathcal{L}_2) p_i / 2F_p^2 \right]$$

$$\phi_x^{i\ell}(\xi^\ell) = (w^2/4A_i)^{1/2} \{ \mathcal{E}[A_i^{1/2}(1 + B_x^i(\xi_\ell))] + \mathcal{E}[A_i^{1/2}(1 - B_x^i(\xi_\ell))] \}$$

$$A_i = \frac{kw^2}{4\pi} \left[\frac{M_T}{M_S(\mathcal{L}_1 - \mathcal{L}_2)} - \frac{p_i}{2F_p^2} \right]$$

$$q_x = L_2 \theta_{SHP}^x + (\mathcal{L}_1 - \mathcal{L}_2) \theta_{SLP}^x / M_T$$

$$\mathcal{L}_1 = M_T L_1 + M_S B_T$$

$$\mathcal{L}_2 = M_T L_2 + M_S B_T^i$$

$$B_x^{i\ell}(\xi) = \alpha_x^{i\ell} + \beta^i \xi$$

$$\alpha_x^{i\ell} = \frac{2}{w} \left\{ x_{O\ell} - x_{Oi} - q_x + M_S(\mathcal{L}_1 - \mathcal{L}_2) \left(\frac{p_i x_{Oi}}{2F_p^2} - 2\theta_{Tx}^i \right) \right\} /$$

$$\left[1 - \frac{M_S}{M_T} (\mathcal{L}_1 - \mathcal{L}_2) p_i / 2F_p^2 \right]$$

$$\beta^i = \frac{2}{w} \left[1 - \frac{M_S}{M_T} (\mathcal{L}_1 - \mathcal{L}_2) p_i / 2F_p^2 \right]^{-1}$$

plus a similar set of quantities with x and ξ replaced by y and n everywhere. In addition, C is a constant amplitude factor, NS is the number of segments in the mirror, M_S the magnification (>1) of the primary

telescope, F_{p0} the focal length of the primary, and $F_p = F_{p0}/(1 - 2F_{p0}/L_0)$. Finally, the function $\mathcal{E}(Z)$ is the complex Fresnel integral

$$\mathcal{E}(Z) = \int_0^Z \exp\{j \frac{\pi}{2} u^2\} du.$$

As written above, the quantity A^i is assumed to be positive. If it is negative, A^i is replaced by $|A^i|$ and the function \mathcal{E} by its complex conjugate.

The quantity of primary interest for assessing the effects of misalignment is not the output field itself but the beam quality number. In order to calculate beam quality the output field must be focused and the field in the focal plane evaluated. To within a phase factor, the focal plane field is the Fourier transform of the field out of the primary. Using the Shifting Theorem this transform may be written as the sum of the transforms of the field leaving each segment. Each transform can be evaluated analytically. The result for the field in the focal plane is

$$F(x_F, y_F) = C \sum_{\ell=1}^{NS} R_{1x}^{\ell} R_{1y}^{\ell} \exp\{jk(x_F x_{0\ell} + y_F y_{0\ell})/f\} \times$$

$$\sum_{i=1}^{NS} R_{2x}^{\ell i} R_{2y}^{\ell i} G_x^{\ell i} \left[k \left(\frac{x_F}{f} + \Omega_x^{\ell i} \right) \right] G_y^{\ell i} \left[k \left(\frac{y_F}{f} + \Omega_y^{\ell i} \right) \right]$$

where (x_F, y_F) is a point in the focal plane of a focusing lens with focal length f , and

$$G_r^{\ell i}(z) = \int_{-w/2}^{w/2} \phi_r^{\ell i}(\xi) \exp\{j z \xi\} d\xi$$

with $r = 'x'$ or $'y'$. The integral for $G_r^{\ell i}$ can be evaluated, with the result

$$G_x^{\ell i}(kx_F/f) = \frac{-jfw}{2k(A_i)^{1/2}x_F} \{ \phi_1(x_F) H_{1x}^{\ell i} - \phi_1^*(x_F) H_{2x}^{\ell i} + \phi_{3x}^{\ell i}(x_F) [\phi_2^i(x_F) H_{3x}^{\ell i}(x_F) + \phi_2^{i*}(x_F) H_{4x}^{\ell i}(x_F)] \}$$

where

$$\phi_1(x_F) = \exp\{jkwx_F/2f\}$$

$$\phi_2^i(x_F) = \exp\{jkx_F/f\beta^i\}$$

$$\phi_{3x}^{\ell i}(x_F) = \exp\{-jkx_F/(f\beta^i)[\alpha_x^{\ell i} + kx_F/(2\pi A_i f\beta^i)]\}$$

$$H_{1x}^{\ell i} = \mathcal{E}[(A_i)^{1/2}(1 + \alpha_x^{\ell i} + t^i)] + \mathcal{E}[(A_i)^{1/2}(1 - \alpha_x^{\ell i} - t^i)]$$

$$H_{2x}^{\ell i} = \mathcal{E}[(A_i)^{1/2}(1 + \alpha_x^{\ell i} - t^i)] + \mathcal{E}[(A_i)^{1/2}(1 - \alpha_x^{\ell i} + t^i)]$$

$$H_{3x}^{\ell i}(x_F) = \mathcal{E}[(A_i)^{1/2}(1 - \alpha_x^{\ell i} + t^i - kx_F/(\pi A_i f\beta^i))] - \mathcal{E}[(A_i)^{1/2}(1 - \alpha_x^{\ell i} - t^i - kx_F/(\pi A_i f\beta^i))]$$

$$H_{4x}^{\ell i}(x_F) = \mathcal{E}[(A_i)^{1/2}(1 + \alpha_x^{\ell i} - t^i + kx_F/(\pi A_i f\beta^i))] - \mathcal{E}[(A_i)^{1/2}(1 + \alpha_x^{\ell i} + t^i + kx_F/(\pi A_i f\beta^i))]$$

$$t = \beta^i w/2$$

and the remaining functions and constants have been defined previously. As before, if $A_i < 0$, $(A_i)^{1/2} + (-A_i)^{1/2}$ and $\mathcal{E} + \mathcal{E}^*$. Identical equations are found for $G_y^{\ell i}(ky_F/f)$ by replacing $'x'$ by $'y'$ everywhere in the preceding equations.

Note that diffraction effects are represented by the presence of the Fresnel integral functions whose behavior is determined by the constant A_i . This constant (times 0.5) plays the role of a propagation Fresnel number; i.e., for small A_i diffraction effects are large, while if $A_i \rightarrow \infty$ geometric optics applies. The value of A_i depends inversely on $x_1 - x_2$, the difference in effective propagation path lengths between the ingoing (to the phase conjugator) and outgoing fields.

To calculate beam quality, a 'Q=1 bucket' size is found by finding the first null in the x or y directions at the focus of a uniform field which fills the primary mirror. The power in a square bucket of this size, for the uniform field, is defined to be the ideal, or reference, power. The power in the same bucket for an actual field is then found by integrating numerically the absolute square of the field $F(x_F, y_F)$. The ratio of the reference to actual powers is the beam quality number.

6.3.1.2 Two-Dimensional Model

A two-dimensional wave-optics model was also formulated which is similar to the three-dimensional model, but simpler in the sense that the field from the beacon is traced only part way through the optical system, to the position of the amplifier entrance and to the SBS cell. A two-dimensional formulation is used because the codes which model the amplifier (LCFM code) and the phase conjugator (BOUNCE code) are themselves two-dimensional models. The objective is to assess conjugation fidelity under conditions of primary mirror segment misalignment. For a system containing, say, seven amplifiers, the fields into any one amplifier would originate from five or six primary mirror segments. Thus, in a linear dimension, the field from only two or three segments would form the beam into one amplifier. Because of the small number of segments per beam, segment misalignment values are simply assigned as input data to the code, rather than generating their values by sampling a random distribution as is done in the three-dimensional code. The equations for the two-dimensional wave optics model are developed in the following section.

6.3.1.3 Two-Dimensional Propagation Equations

Two-dimensional fields which model, in the physical optics approximation, the effects of beam director segment misalignment and passage through an optical train are required. The procedure for development of the equations follows closely Steps 1 through 6 of Section 6.3.1.1, with the exception, of course, that the dependence on one of the coordinate variables is dropped. In addition, since there are multiple amplifiers the field off the primary mirror will be divided at some point so that the beam into a particular amplifier will originate from only a few segments. The model therefore traces the field from a line source to a few (typically two or three) misalignment segments located at a specified position on the primary mirror, and then to the secondary mirror and through an optical train. Setting up the equations and carrying out the required integrations is straightforward though somewhat tedious. The resulting expression for the complex field is

$$E(x) = (j/\lambda r_1)^{1/2} C \exp\{-jk\theta_{SLP}x/M_T\} \sum_{i=1}^N Q_i(x)U_i(x)$$

where

$$Q_i(x) = \exp\{jk[p_i r^2 x^2 / 4F_p^2 - 2((\theta_T^i - b_0 p_i / 4F_p^2)rx - \theta_T^i x_{oi}) - 2p_i - p_i b_0 (b_0 + 2x_{oi}) / 4F_p^2]\}$$

$$U_i(x) = A_i^{-1/2} \{e^{*}[A_i^{1/2}(w/2 + B_i)] + e^{*}[A_i^{1/2}(w/2 - B_i)]\}$$

$$A_i = \frac{2}{\lambda r_1} \left(1 - \frac{p_i r_1}{2F_p^2} \right)$$

$$B_i = rx \left(1 + \frac{p_i r_1}{2F_p^2} \right) - x_{oi} - r B_T \theta_{SLP} - 2\theta_T^i r_1$$

$$r = M_S/M_T$$

$$\chi_1 = M_T L_1 + M_S B_T$$

$$F_P = F_{P0}/(1 - 2 F_{P0}/L_0)$$

and the remaining quantities, except for b_0 , are as defined in Section 6.3.1.1. The quantity b_0 is the distance from the axis of the primary mirror to the center of the group of N segments whose effect is being considered. The x coordinate of the propagated field is measured with respect to the point in the final plane which is the geometric mapping through the aligned telescope and optical train of the center of the segment group.

6.3.2 Calculations and Results

A computer code was written to evaluate equations derived for the far-field intensity of the collimated high-power output beam, and beam quality evaluated. For purposes of the preliminary calculations the optical paths from the primary to the phase conjugator, and from the phase conjugator back to the primary, were assumed to differ only in the locations of the low- and high-power secondaries. The segment misalignment tilt angles in both directions and segment piston error were assumed to be independent random variables with a normal distribution. Specific values for the misalignments of each segment were selected by specifying the variance of each variable (tilts in the x and y directions were always assigned equal variance) and then selecting values randomly from a zero-mean normal population with the prescribed variance. For clarity in showing trends and avoiding excessive scatter of points, this procedure was used for one variance value; for other values of the variance the same set of misalignment values was then used but scaled in magnitude to provide the new variance value. An indication of the spread in beam quality values for different random samples having the same variance is shown in the numerical results.

RMS tilt angles up to $10 \mu\text{rad}$ were considered. It is assumed that jitter frequencies lower than about 200 Hz are mechanically compensated; higher frequencies are estimated to have a most probable value of around $0.4 \mu\text{rad}$. RMS piston errors up to several hundred wavelengths were considered. Two values of beacon distance were used - 10 and 100 times the primary mirror diameter. In most cases three values of the primary mirror f/number were used as parameters - $f/8$, $f/4$, and $f/2$. While $f/1$ would be of interest, the model would be of doubtful validity for this case, principally because of the paraxial assumption. For the case of a beacon distance of 10 mirror diameters, only $f/4$ and $f/2$ cases were considered, since at $f/8$ the low power secondary would be outside the beacon - a situation of little interest.

The results of the computations are summarized in a set of beam quality versus misalignment plots, and are shown in Figures 6-8 through 6-11. They may be used to estimate the contribution to the beam quality budget of segment misalignment for different values of beacon distance and f/number parameters. It is expected that the results may be somewhat optimistic, however, because of the simplifying assumptions made in the model. For example, imperfect phase conjugation caused by nonlinear gain effects in the amplifiers, beam aperturing within the optical train, or the operation of the SBS cell itself would increase the sensitivity of beam quality to beam director misalignments.

For the two-dimensional model, the results to date are only in the form of plots of "typical" fields which might exist at the amplifier and phase conjugator positions assuming a particular set of misalignments and optical train elements. Figures 6-12a through 6-12f show intensity and phase plots for two-dimensional fields entering the amplifier and SBS cell, for the segment misalignments shown in Table 6-1. Since the field profiles depend on the magnifications and path lengths of the optical train, the results shown should be taken as merely suggestive; these calculations may be repeated as the actual optical elements, and their positions, become better defined. It appears likely, however, that because of the large demagnifications required, the propagation Fresnel numbers will tend to be rather low. For low Fresnel numbers the spreading of the beam beyond its

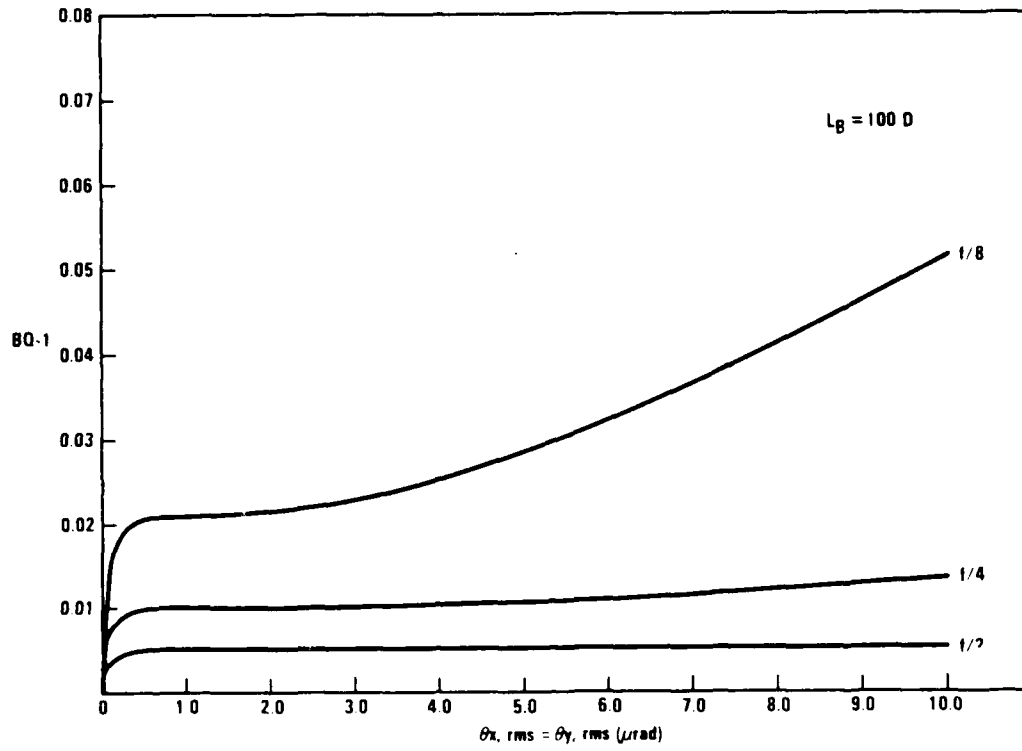


Figure 6-8. Beam quality versus segment tilt ($L_g = 100 D$).

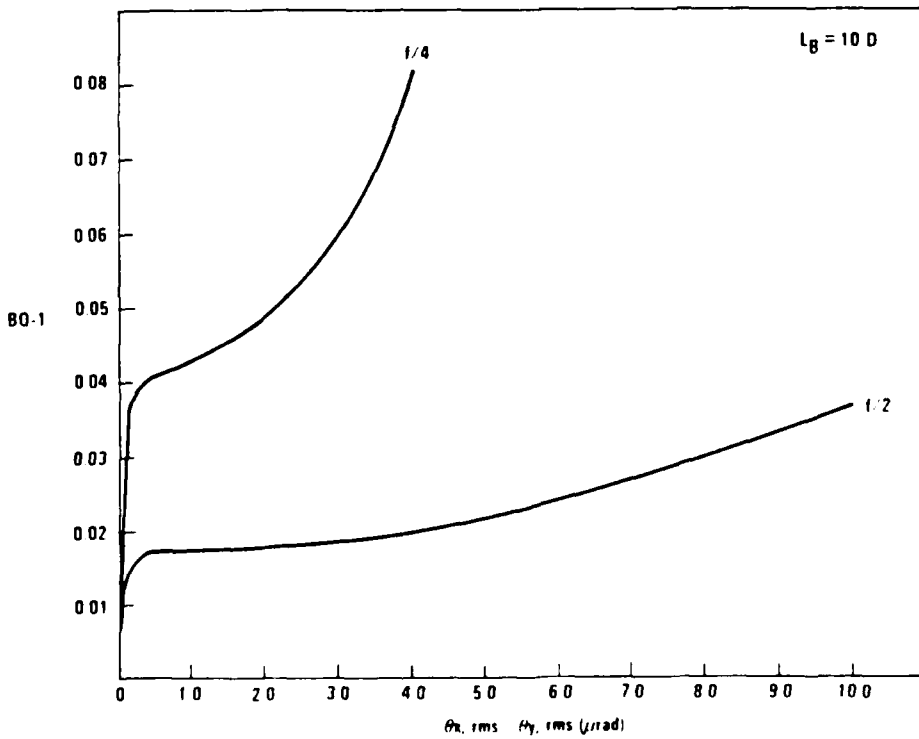


Figure 6-9. Beam quality versus segment tilt ($L_g = 10 D$).

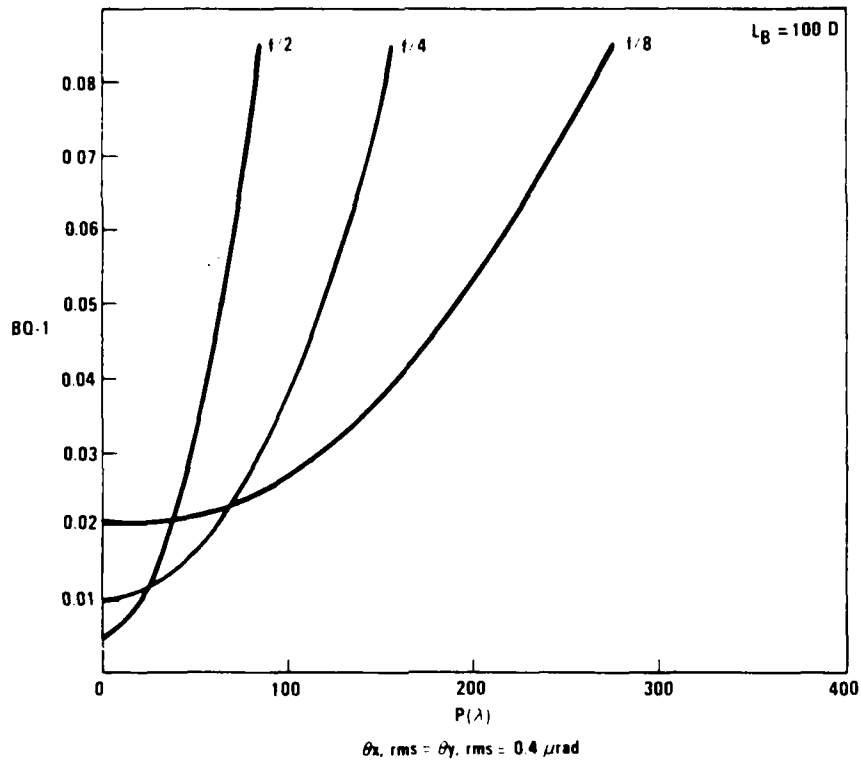


Figure 6-10. Beam quality versus piston error ($L_B = 100 D$).

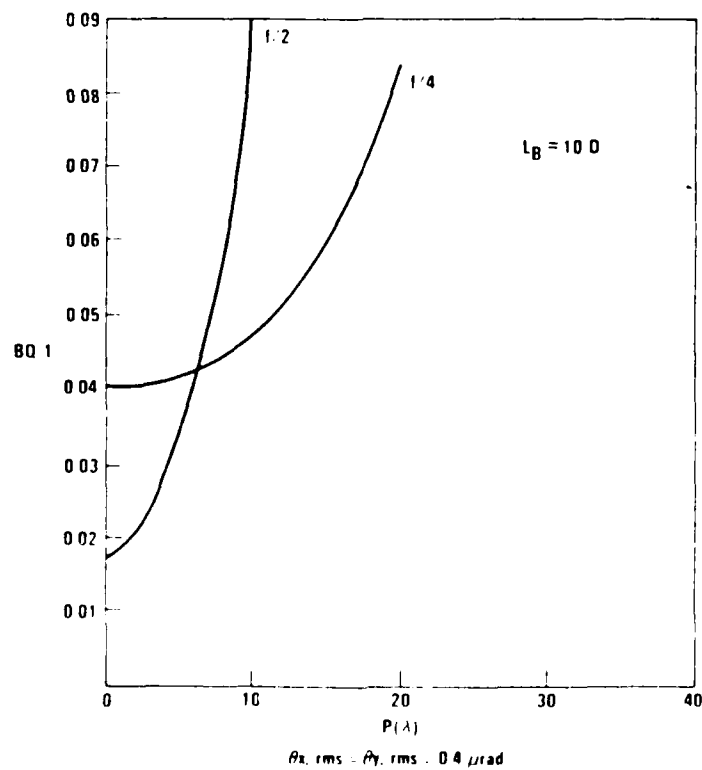
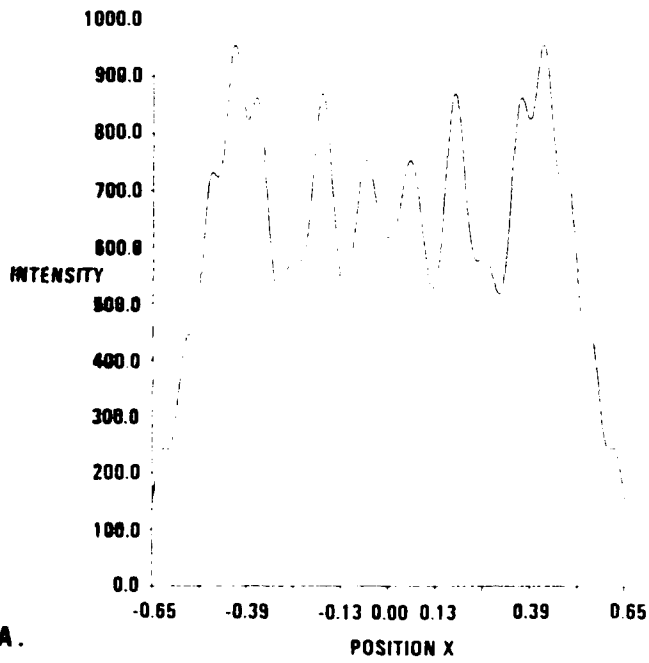


Figure 6-11. Beam quality versus piston error ($L_B = 10 D$).

NSEG 2
 SEG FRNL NO 1.340
 BMCEN 0.00
 NX 512

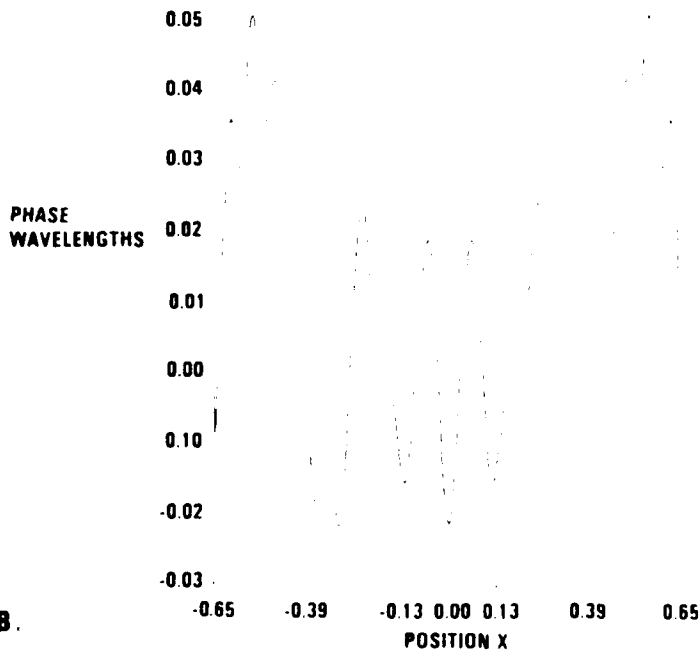
| SEGMENT NUMBER | TILT ERROR | PISTON ERROR |
|----------------|------------|--------------|
| 1 | 0.00 | 0.00 |
| 2 | 0.00 | 0.00 |



A.

NSEG 2
 SEG FRNL NO 1.340
 BMCEN 0.00
 NX 512

| SEGMENT NUMBER | TILT ERROR | PISTON ERROR |
|----------------|------------|--------------|
| 1 | 0.00 | 0.00 |
| 2 | 0.00 | 0.00 |

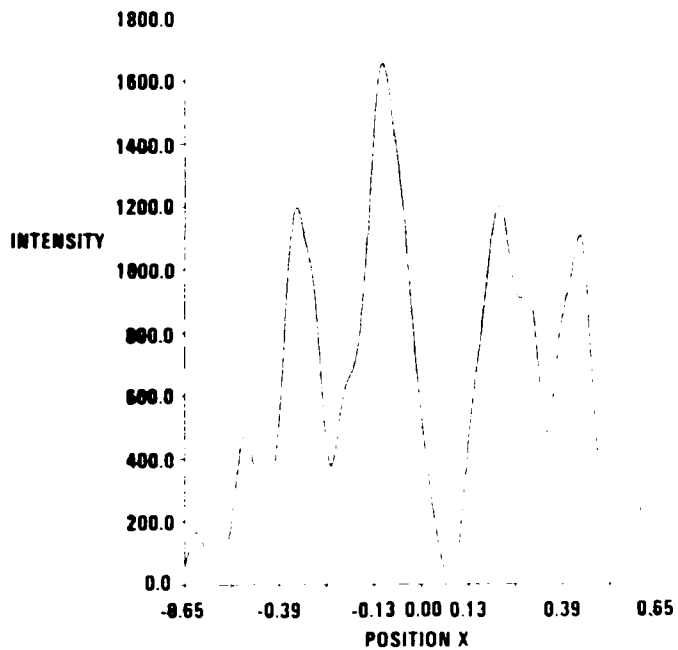


B.

Figure 6-12. Field into amplifier.

NSEG 2
 SEG FRNL NO 1.340
 BMCEN 0.00
 NX 512

| SEGMENT NUMBER | TILT ERROR | PISTON ERROR |
|----------------|------------|--------------|
| 1 | 0.30 | 0.00 |
| 2 | -0.10 | 0.00 |



NSEG 2
 SEG FRNL NO 1.337
 BMCEN 1071.00
 NX 512

| SEGMENT NUMBER | TILT ERROR | PISTON ERROR |
|----------------|------------|--------------|
| 1 | 0.30 | 20.80 |
| 2 | -0.10 | 3.35 |

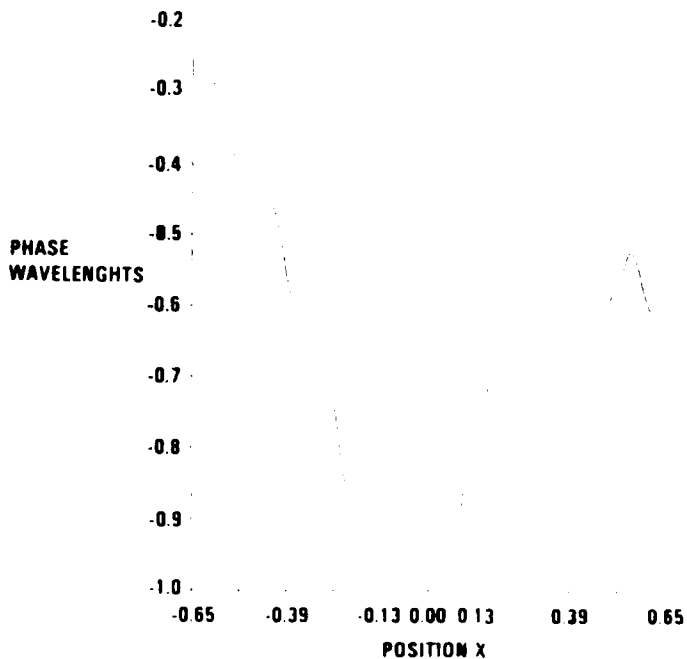
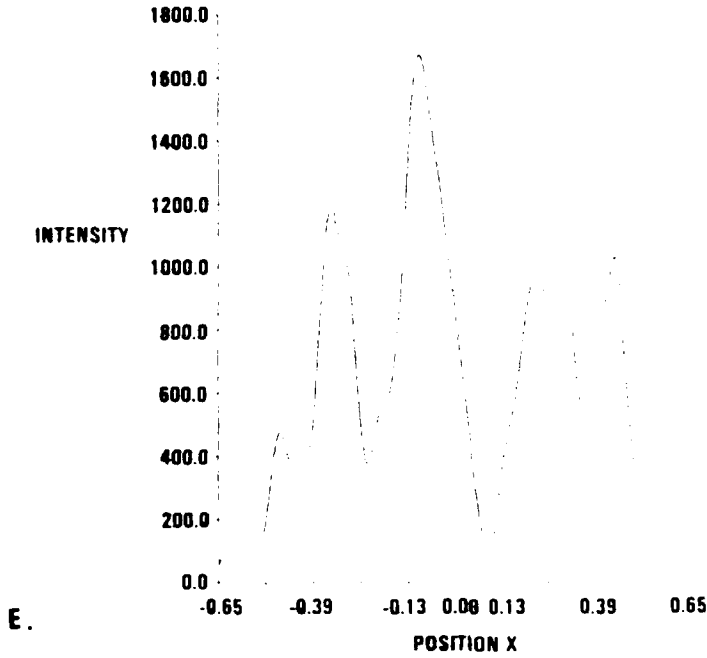


Figure 6-12. Field into amplifier (continued).

NSEG 2
 SEG FRNL NO 1.337
 BMCEN 10 1.00
 NX 512

| SEGMENT NUMBER | TILT ERROR | PISTON ERROR |
|----------------|------------|--------------|
| 1 | 0.30 | 20.80 |
| 2 | -0.10 | 3.35 |



NSEG 2
 SEG FRNL NO 1.340
 BMCEN 0.00
 NX 512

| SEGMENT NUMBER | TILT ERROR | PISTON ERROR |
|----------------|------------|--------------|
| 1 | 0.30 | 0.00 |
| 2 | -0.10 | 0.00 |

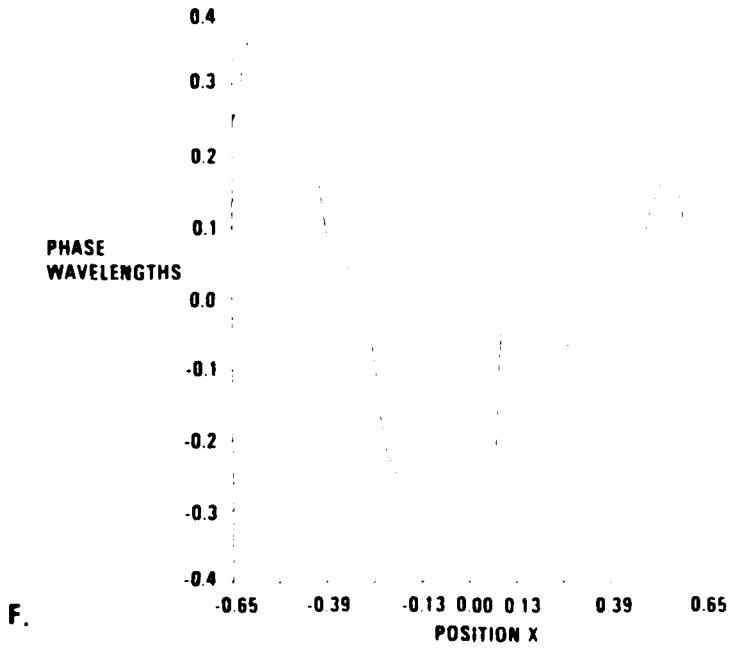


Figure 6-12. Field into amplifier (continued).

TABLE 6-1. Optical Train Assumed for Field Calculations.

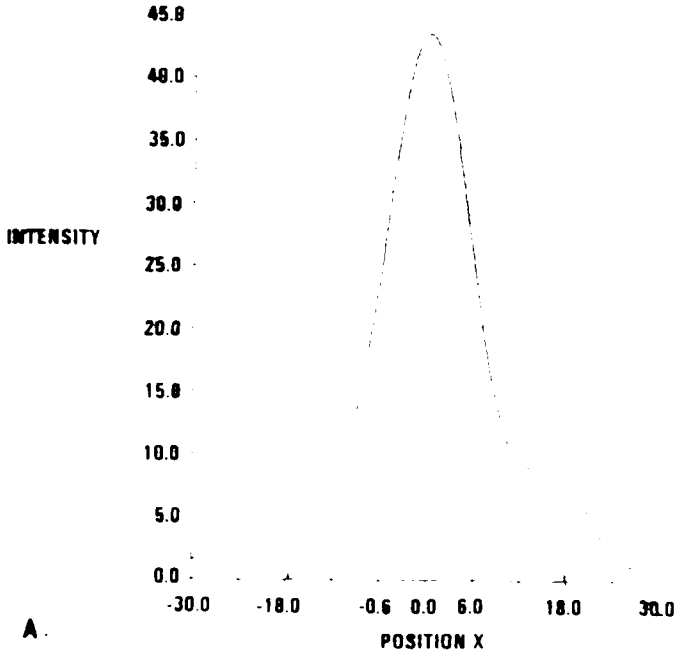
| From | To | Distance* | Magnification |
|------------|-------------------------|-----------|---------------|
| Beacon | Beam director primary | 10 | — |
| Primary | Beam director secondary | 2.3 | 1/12.5 |
| Secondary | Telescope | 3.3 | 1 |
| Telescope | | — | 1/17.6 |
| Telescope | Amplifier inner cone | 0.6 | 1 |
| Inner Cone | Outer cone | — | 1/3 |
| Amplifier | | 0.67 | 1 |
| Outer cone | Inner cone | — | 3 |
| Inner cone | SBS | 0.33 | 9 |

* Distance in units of primary mirror diameter

geometric size may be substantial, and difficulties may be encountered in avoiding beam aperturing. The entrance aperture to the amplifier annular gain region was taken to be 1.3 cm ($x = -0.65$ to $+0.65$ in Figure 6-12f), and that of the SBS cell to be 35 cm ($x = -17.5$ to $x = +17.5$ in Figures 6-13a through 6-13d). Beam displacement due to segment tilt, and interference effects from beam overlap, are also quite pronounced. For the assumed geometry at least, the wave optics fields differ markedly from the geometric optics fields (e.g., uniform amplitude and phase) normally used as input to the LFCM and BOUNCE codes.

NSEG 2
 SEG FRNL NO 0.164
 BMCEN 1071.00
 NX 512

| SEGMENT NUMBER | TILT ERROR | PISTON ERROR |
|----------------|------------|--------------|
| 1 | 0.00 | 0.00 |
| 2 | 0.00 | 0.00 |



NSEG 2
 SEG FRNL NO 0.164
 BMCEN 1071.00
 NX 512

| SEGMENT NUMBER | TILT ERROR | PISTON ERROR |
|----------------|------------|--------------|
| 1 | 0.00 | 0.00 |
| 2 | 0.00 | 0.00 |

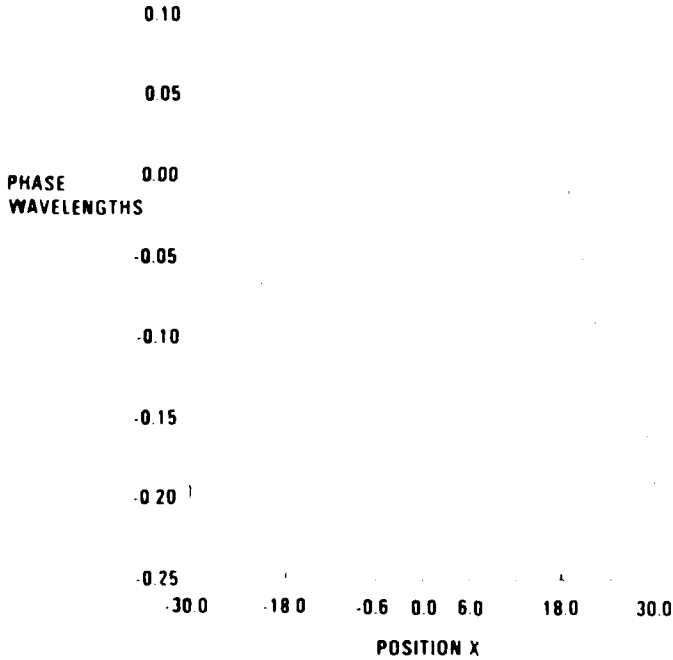
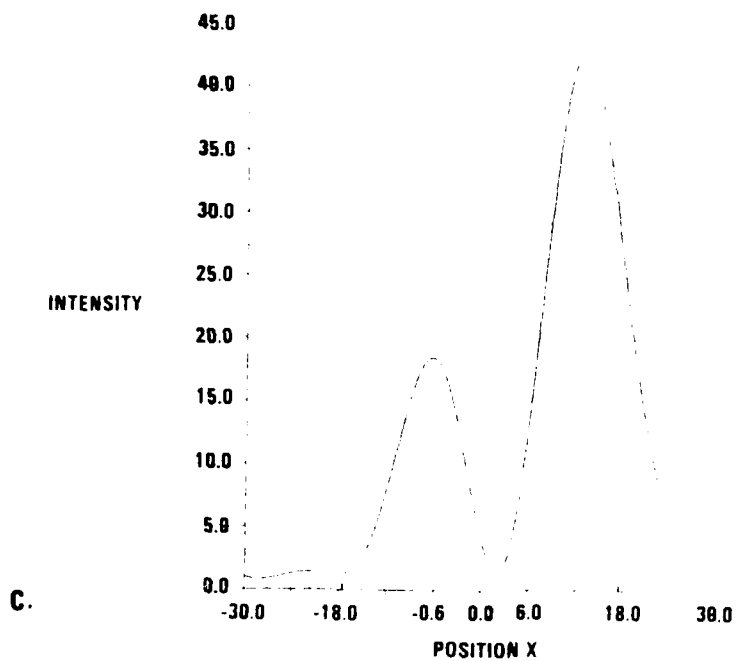


Figure 6-13. Field into SBS.

NSEG 2
 SEG FRNL NO 0.162
 BMCEN 1071.00
 NX 512

| SEGMENT NUMBER | TILT ERROR | PISTON ERROR |
|----------------|------------|--------------|
| 1 | 0.30 | 20.80 |
| 2 | -0.10 | 3.35 |



NSEG 2
 SEG FRNL NO 0.162
 BMCEN 1071.00
 NX 512

| SEGMENT NUMBER | TILT ERROR | PISTON ERROR |
|----------------|------------|--------------|
| 1 | 0.30 | 20.80 |
| 2 | -0.10 | 3.35 |

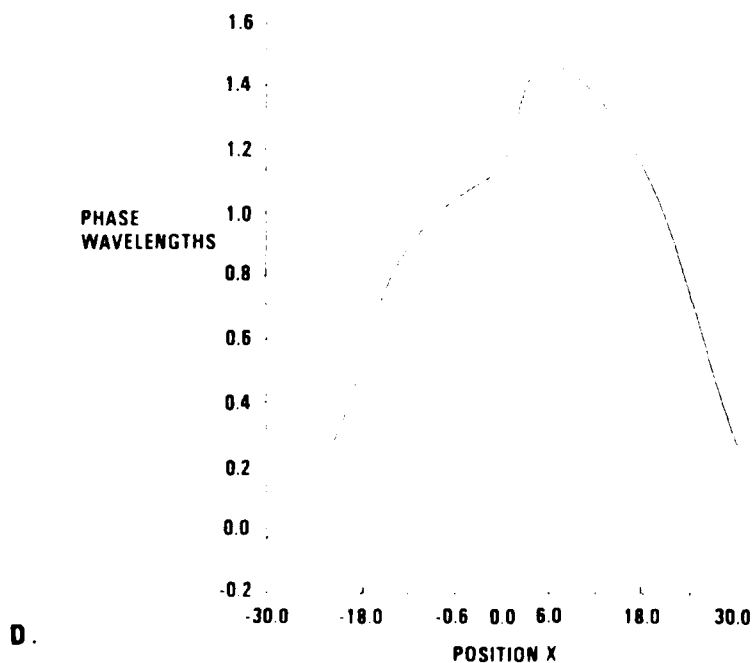


Figure 6-13. Field into SBS (continued).

7. PHASE-CONJUGATION SUBSYSTEM

7.1 PHASE CONJUGATION SUBSYSTEM PRELIMINARY CONCEPT AND TRADE STUDIES

7.1.1 Objective and Approach

The objective of the phase conjugation subsystem effort is to develop the analytical tools with which to design the SBS cell, spectral separation grating, quarter wave retarding coating, and focusing optics.

The approach was to use the BOUNCE and BRIWON codes to characterize the interaction of the following parameters:

1. SBS cell input power
2. SBS cell reflectivity
3. Threshold power (required for 10 percent reflectivity)
4. Beam focusing geometry (near- and far-field overlap)
5. Beam combination (several beams in a common focal volume)
6. Beam propagation issues (thermal blooming, self-focusing, etc.)
7. Stokes-seed back-injection (to lower threshold, but accomplish multibeam piston-error correction)
8. SBS conjugation fidelity (measure of output beam quality)
9. SBS medium properties (impurities, temperature, pressure, etc.)

Many of these parameters were examined using the previously mentioned codes, and the results were used to produce the preliminary configuration shown in this report. These results are presented in the remaining portions of this section.

7.1.2 Phase Conjugation Major Trade Issues

Several areas have been identified that require trade studies of candidate design approaches to meet the requirements. These issues are presented below.

7.1.2.1 Trade Issue: Type of Cell Medium, and Conditions

Relevant issues and comments: The type of gas used in the SBS cell affects conjugation fidelity, reflectivity, and threshold power. Pressure

and temperature also affect these parameters. Analytical results indicate xenon at 40 atm and 300 K has the desired SBS characteristics. COS experiments will address these issues.

7.1.2.2 Trade Issue: Cell Medium Purity

Relevant issues and comments: The level and type of impurities in the medium affect propagation phenomena such as thermal blooming and self-focusing. COS experiments will anchor analytical calculations.

7.1.2.3 Trade Issue: Flow Velocity

Relevant issues and comments: Flow velocity is relevant to thermal absorption issues and phonon rise time concerns, and is intimately associated with the flow direction. For transverse flow, the gas must move fast enough to limit thermal absorption, but not fast enough to smear the phonon grating which exists on time scales on the order of the phonon rise time, since this would reduce conjugation fidelity. Preliminary calculations show that a range of 20 to 80 meters/sec is acceptable.

7.1.2.4 Trade Issue: Flow Direction

Relevant issues and comments: Flow in the SBS cell that is either transverse or antiparallel to the beam will either not correct or correct, respectively, for the SBS frequency shift in the Stokes beam. Analysis (see Section 5.2.3) shows no shift compensation is required since there is small power loss in the amplifiers due to the SBS frequency shift. Therefore transverse flow is acceptable.

7.1.2.5 Trade Issue: Number of Cells

Relevant issues and comments: Each line requires separate focal volumes in the SBS medium; this may be accomplished through separation in a common cell, or by using individual cells for each line. Separate cells appear easier to fabricate, use less gas, and eliminate potential focal volume interference effects that might exist in a common cell.

7.1.2.6 Trade Issue: SBS Telescope f/Number

Relevant issues and comments: The focal length divided by the diameter of the focusing optics affects conjugation fidelity and cell length

and width requirements. Probable range is f/10 to f/50. COS experiments will address this issue.

7.1.2 Preliminary Configuration

The four side-by-side SBS cells were shown in Figure 4-7. Note that the fraction of energy that is transmitted through the cells is directed backward toward the rear of the spacecraft and out into space so that it will not disturb any satellite hardware. The exhausted helium and xenon gases also are directed out towards the back of the spacecraft.

7.2 PHASE CONJUGATION ANALYSIS

7.2.1 SBS Modeling

Phase conjugation is the wavefront process by which a beam retraces its path through aberrations and corrects its wavefront distortion by virtue of phase sign reversal over that of the forward beam. An important method of phase conjugation is SBS reflection from a phase conjugation cell containing an appropriate nonlinear optical medium. For PALS this is xenon at about 40 atm pressure.

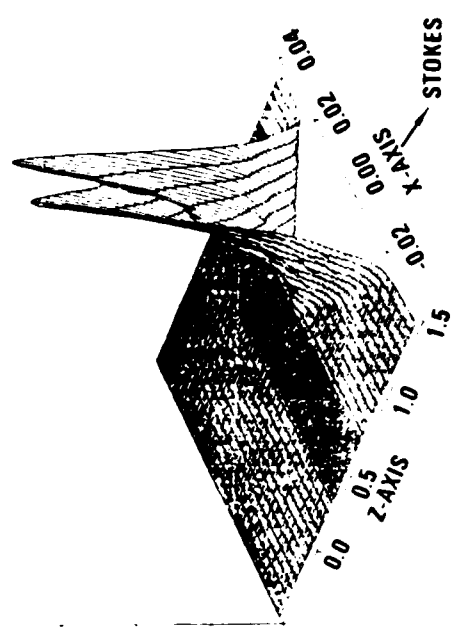
SBS phase conjugation occurs by means of the preferential amplification of the backscattered wave that is the phase conjugate, i.e., the (backward-going Stokes) wave with the apparent time-reversed propagation properties to those of the incident wave (pump beam).

In the case of a pump beam focused into the cell, the intense focal region comprises a substantial part of the so-called interaction region for the SBS phase conjugation. However, as seen in Figure 7-1a, the Stokes intensity is greatest forward of the focal region, and, in this case at twice threshold power, is restrained by the forward position of the mathematical cell window at 1 cm ahead of the focal center at the origin. The f/number (lens focal length divided by hypergaussian beam diameter) of the pump beam is 40. The Rayleigh range, i.e., the full length of the diffraction limited focal region, is approximately

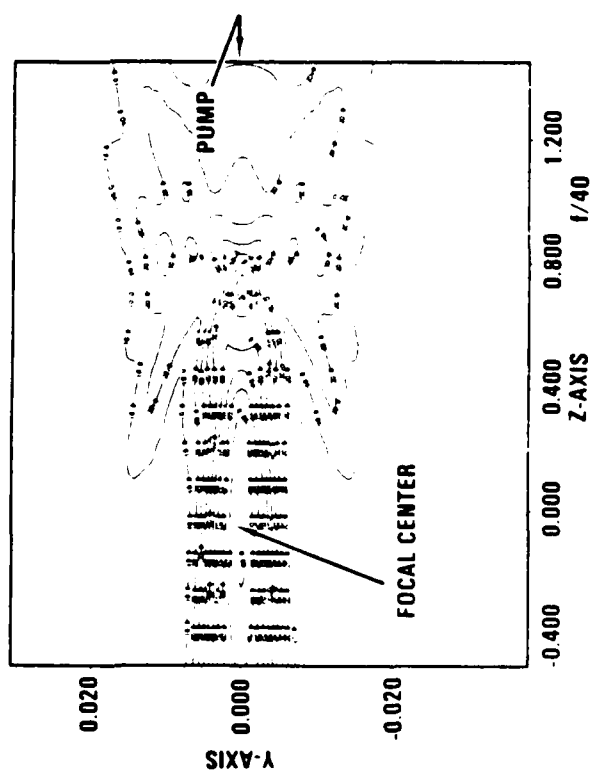
$$L = 4\lambda (F/\#)^2 = 1.5 \text{ cm} \quad (7.1)$$

a value which agrees with the contour plot of Figure 7-1b.

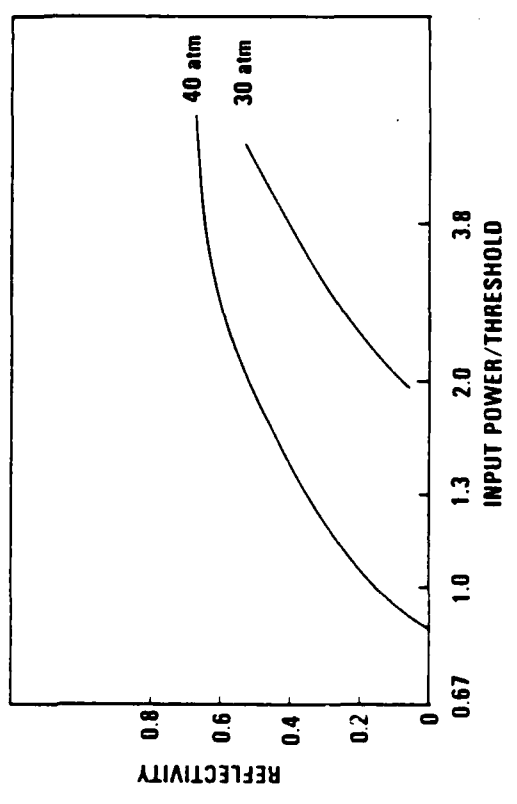
105
5.0
4.0
3.0
2.0
1.0
0.0



A. Stokes Electric Field Squared (esu)



B. Pump Intensity Contours (%)



Reflectivity Versus Power for Xenon

Figure 7-1. Characterization of SBS reflectivity from xenon gas.

Details of the SBS phase conjugation process are calculated in the BOUNCE code. The electromagnetic wave equations for the pump and Stokes beams are solved by a combination of amplification and propagation algorithms working over a discrete two-dimensional space. The gain sheets at which the amplification or gain is implemented are specified along the axial propagation direction. Diffractive propagation sideways is implemented by a fast Fourier transform technique in one transverse direction. Effects in the other transverse dimension are treated by simple geometrical focusing factors down to a diffraction-limited cutoff distance at the focal region.

The amplification derives from the SBS or stimulated Brillouin scatter in which pump photons are converted to Stokes photons at a rate that is proportional to the number of photons of both pump and Stokes waves. The spatial and temporal beats between the two waves drive an acoustic wave, i.e., phonons. This acoustic grating is the scatter mechanism whereby the complicated far-field pattern of pump intensity spots is replicated by Stokes backscatter. Aberrations have distorted the incident pump wavefront to produce this complicated far-field intensity pattern.

When the phonons have a large damping factor, as they usually do for backward light scatter at infrared or shorter wavelengths, the acoustic wave amplitudes are driven locally by the product of the pump and Stokes-complex-conjugate electric fields. The acoustic wave frequency and wave vector, in the plane wave decomposition of all the waves, are the appropriate differences of the pump and Stokes quantities, and they are also related to the acoustic wave dispersion relation involving the speed of sound in xenon.

The local nature of the relationship between acoustic wave amplitude and pump-Stokes product is lost when a cross-flow exists. A convolution of this electric field product and the exponential function for convection and damping with transverse distance along the flow replaces this local relationship. With increased cross-flow speed the smearing effect of this convolution is evident in a decrease in gain coefficient and in a new non-linear refractive index contribution. The gain coefficient reduction is a serious matter when competition with amplification for Stokes waves other

than the conjugate Stokes wave is at stake. Typically the phase conjugate Stokes wave has about a factor of two larger gain coefficient than for the similar but nonconjugate Stokes waves, in the absence of cross-flow.

If the distance d characterizes the transverse distance over which the pump-Stokes product is correlated, then the gain coefficient is reduced by the approximate factor

$$(1 + 2V\tau/d)^{-1}, \quad (7.2)$$

where τ is the reciprocal damping rate constant for the acoustic wave. This quantity has already been referred to as the small-signal phonon rise time or phonon lifetime. The cross-flow or transverse flow speed is denoted by V .

The rise time for phonons generated in forward SBS is much larger than for the backscatter SBS phonons. Thus, the cross-flow speed is chosen to flush phonons generated in forward SBS but not in backward SBS.

The BOUNCE code is difficult to run successfully at high reflectivity. A successor to BOUNCE has been developed that reaches convergence in its iterations in a somewhat different manner, and usually the costs to run BRIWON (or B1) are less.

Instead of using conservation of energy between the pump and Stokes beam as a criterion of convergence, BRIWON incorporates energy conservation within the amplification algorithm at the gain sheets. For convergence BRIWON requires the same results whether integrating the simultaneous equations in the forward direction or in the backward direction. Meanwhile, the pump boundary condition at the front of the cell and the Stokes boundary condition of growth from Stokes noise mainly from the back of the interaction region are satisfied.

Figure 7-1c also shows reflectivity curves for xenon at 30 and 40 atm. The horizontal scale is input pump power in units of threshold power for the 40 atm case. Threshold is defined as that power resulting in 10 percent SBS

reflectivity. The threshold power for 40 atm is calculated to be about 150 kW. This is close to that calculated from the formula that follows:

$$gIL = gPL / (2\lambda F/\#)^2 = 25 \quad (7.3)$$

or

$$P = 25\lambda/g \quad (7.4)$$

where g is the gain coefficient, P is the input power, $F/\#$ is the beam f /number, λ is the wavelength and L is the Rayleigh range discussed above. A round beam and a somewhat higher value for the gIL product, namely 30 instead of 25, yield 240 kW, as noted by NRL's Whitney, et al. (Ref. 7.1).

The horizontal scale in Figure 7-1c is logarithmic. The two curves for the different pressures lie almost a fixed horizontal distance apart, indicating that the reflectivities are in a fixed ratio to each other. This ratio is close to the square of the ratio of pressures. This is expected from the scaling of the gain coefficient, which is proportional to the square of the pressure. One power of pressure is the usual one from the dependence on the number density of scatters, while the second power of pressure is from the phonon rise time. That is, the gain coefficient is directly proportional to the phonon lifetime, which is inversely proportional to the phonon bandwidth. The bandwidth decreases with pressure because the kinematic viscosity and thermal diffusivity that damp the acoustic waves for the xenon both decrease with pressure at a given temperature.

The simultaneous SBS phase conjugation of two beams has been calculated with both codes. The results are not fully converged. BRIWON indicates that there is no penalty in reflectivity at a given power with two beams compared to one, provided that there is overlap of interaction volumes in the cell.

Beam quality as well as conjugation fidelity characteristics are output of the codes or of ancillary codes.

7.1 "SBS with an HF Laser," S. Whitney, et al, Post-deadline paper, presented at International Conference on Lasers 1985, Dec 2-6, Las Vegas, NV.

7.2.2 Competition with SBS

Nonlinear processes that might compete with SBS include stimulated Raman scattering, nonlinear absorption, stimulated thermal Brillouin scattering, and stimulated Rayleigh line scattering.

A process that competes with SBS is SRS, stimulated Raman scatter, which is possible for molecular xenon formed at these high pressures and densities. At 40 atm about 15 to 20 percent by number is diatomic xenon. The conversion of pump to Stokes photons in SRS excites internal rotation-vibration states (analogous to so-called optic phonons).

SRS has a gain coefficient that is usually much smaller than for SBS. A calculation based on polarizability data (Ref. 7.2) confirms this. If the xenon were entirely in diatomic form, i.e., as van der Waals molecules, the SRS gain coefficient at 40 atm would be about 3×10^{-5} cm/MW compared with the SBS gain coefficient of about 5×10^{-2} cm/MW.

Competition with SBS might occur in the short pulsed case, for which the slower rise time of the acoustic wave puts SBS in the transient regime. Then, the transient SBS gain coefficient might be less than the gain coefficient for SRS, which might be in the steady-state regime owing to the much shorter rise time (about 10^{-10} s) for the rotation-vibration modes of the molecular xenon.

Nonlinear absorption by multiphoton excitation of xenon electronic states is negligible. More than 19 HF photons are needed to reach the first excited state.

Impurities in xenon such as water vapor, carbon dioxide, and nitrous oxide are to be held to low concentrations, i.e., less than 0.1 ppmv. The linear absorption coefficient is then about 3×10^{-6} cm⁻¹ (that is, 0.3 per km). The STBS or stimulated thermal Brillouin scatter process has a gain coefficient (in the usual units of cm/MW) about 700 times the absorption coefficient (in cm⁻¹). This yields a coefficient about 5 percent of that of SBS, for xenon at 40 atm and impurities at less than 0.1 ppmv.

7.2 M.H. Proffitt, et al, Can. J. Phys. 59, 1459-1480 (1981).

STBS results from the absorption of energy from the pump beam, as in thermal blooming; this energy causes a thermal volume expansion that drives an acoustic wave analogous to that in SBS. Characteristics of the Stokes backscatter in frequency shift (107 MHz) and phonon rise time (260 ns) are also similar. Distinctions are seen only at high frequency resolution, where STBS gain coefficient maximum is offset from SBS maximum by about the phonon damping half-bandwidth.

SRLS is stimulated Rayleigh line scatter, which is also dependent on the linear absorption coefficient. However, in this process the driven entropy "wave" rather than the driven acoustic wave is the scatter mechanism. The gain coefficient for SRLS is comparable to that of STBS. The rise time is somewhat longer, however. Thus, in pulsed cases SRLS might be less important. However, in CW or quasi-CW cases, SRLS might dominate. The frequency shift between pump and Stokes signals would be very small for SRLS, compared to that for STBS, since an acoustic wave is not involved with SRLS.

Phase conjugation by backscattered SBS also competes with near-forward SBS. The gain coefficient increases as the angle of scatter decreases. However, the rise time for the phonons generated in the near-forward SBS increases even more strongly with decreasing angle of scatter. Thus, only very long pulsed or, of course, CW cases are concerned with near-forward SBS.

Near the conclusion of the PALS program, a time-dependent, quasi one-dimensional model has been developed to set engineering limits on the speed of crossflow or beam slewing for suppressing near-forward SBS while not diminishing backward-going SBS. The effective gain coefficient for various angles of scatter can be shown, as a function of elapsed time, to approach the usual steady-state coefficient.

The geometry of the focal region needs to be incorporated into the model so that the SBS output at various angles can be estimated as a function of time. The time may be identified with the ratio of the focal spot radius to the relative transverse speed due to crossflow or scanning by the beam.

The well-known behavior of the scattered field according to a Bessel function, whose argument is proportional to the square root of the the product of the elapsed time and the interaction length, is the basis of these effective gain coefficient curves.

7.2.3 Thermal Blooming, Self-Focusing, and IR Gas Breakdown in SBS Cell

The effects on SBS phase conjugation for single-pulse and quasi-CW cases are analyzed by approximate wave propagation formulae and the BOUNCE code with modifications. For thermal blooming, the quasi-CW and pulsed cases are considered and impurity level limits are set. In the CW case, a range of transverse flow speeds is specified. In the pulsed case, a limit on time variation of the beam deformation parameter during the phonon rise time is set. For self-focusing in the quasi-CW case, maximum power is determined by the breakdown threshold in clean xenon. In the pulsed case, focal motion is limited to $1/e$ of interaction length in a phonon rise time. Combined thermal blooming and self-focusing causes partial cancellation with an exponential intensity profile.

Thermal blooming is the distortion of a beam by the nonuniform decrease of refractive index produced by thermal volume expansion due to absorbed beam energy. Self-focusing is the contraction and related distortion of a beam by nonuniform refractive index increase due to the nonlinear effects of the beam intensity. Optical breakdown at HF wavelengths is the creation of plasma, usually in the vicinity of a beam focus by the acceleration of seed electrons in the beam electric field, the impact ionization of the medium, electron avalanche, and HF infrared absorption.

Phase conjugation by SBS in the baseline xenon cell at 40 atm could lose conjugation fidelity and SBS reflectivity if the thermal blooming of the pump and Stokes beams were large enough. Rays of the pump beam that are bent away from the SBS interaction region to where intensities are not high are not phase conjugated. Thus, aberrations introduced by thermal blooming cannot be wholly corrected by SBS phase conjugation.

The thermal blooming discussed here is caused by the absorption of energy at HF wavelengths owing to impurities such as water vapor, carbon dioxide, and nitrous oxide. In the CW or quasi-CW cases, a transverse flow

is introduced to carry away the SBS medium that is disturbed by the heating effect of infrared absorption. Without flow or an equivalent shearing of the beam there would be a continual heating of the medium and detrimental distortion of the beam until very long times when thermal conduction would set up a steady state.

Self-focusing in xenon is possible due to the nonlinear effect of electrostriction on the index of refraction. The coefficient that characterizes this effect is large owing to the large polarizability of xenon atoms. Self-focusing is often accompanied by optical breakdown in the intense focal region. Breakdown competes with, but does not necessarily eliminate SBS.

The pulsed cases of thermal blooming and self-focusing are different from the CW or quasi-CW cases because of the shortness of the elapsed time compared to the transit time of sound waves over a local beam radius. For the focused geometry situation, the beam radius is taken to be the diffraction limited spot radius. This size is characteristic of the finest structure of the strongest intensities, for which the thermal blooming effects are by far the greatest.

For short pulses, because the medium cannot easily adjust its density, and hence, its refractive index, when the sound waves have not crossed the beam to signal an adjustment, the effects of thermal blooming and self-focusing are smaller than for CW or quasi-CW by the square of the ratio of the elapsed pulse time to the sonic transit time. Quasi-CW refers to the cases of long enough laser pulses that the regions of greatest refractive index change are in their steady state with regard to the sonic transit time.

The effects on the beam quality in either phenomenon are conveniently summarized in the distortion parameter DP. This parameter accounts for the change in intensity on axis due to the sideward spread or contraction of the beam. The lowest order wavefront distortions of piston and tilt are correctable by phase conjugation in the usual manner, since changes in relative intensity are not involved, though details of location of the interaction region are.

The next order wavefront distortion of spherical focus or defocus displaces the point of geometric focus. Only the time dependence of this effect is important, and only when there is substantial change in intensity distribution in the interaction region for SBS during a so-called phonon lifetime, which lifetime is the small-signal acoustic wave rise or decay time.

In the CW or quasi-CW cases, the cross-flow causes the pump and Stokes beams to deflect against the flow for thermal blooming. The distortions in the direction perpendicular to both the flow and the original beam directions are essentially free of this type of wavefront tilt. For convenience, the distortion parameter is calculated along this perpendicular direction.

It is noted that thermal blooming does not merely defocus the beam. The central region of the beam intensity distribution acts somewhat in this manner while the wing region acts oppositely, in accordance with the opposite sense of curvature of the distribution and of that induced in the wavefront. This is cylindrically symmetric with no cross-flow. In effect, cross-flow maps the beam intensity distribution to new positions stretched along the flow direction.

The energy conservation equation can be used to express the intensity I on axis in terms of the refractive index be as follows:

$$\frac{\partial I}{\partial s} + \vec{\nabla} \cdot \left(\frac{I}{r} \vec{\nabla} \int_0^s n ds' \right) = 0 \quad \rightarrow \quad I \propto e^{-DP} \quad \text{at } r_{\perp} = 0 \quad (7.5)$$

where DP, the distortion parameter, is given by

$$DP = \int_0^{\ell} \frac{ds}{n(s, \vec{r}_{\perp})} \int_0^s ds' \left[\nabla_{\perp}^2 n(s', \vec{r}_{\perp}) + \vec{\nabla}_{\perp} n(s', \vec{r}_{\perp}) \cdot \vec{\nabla}_{\perp} \ln I(s, \vec{r}_{\perp}) \right]_{\vec{r}_{\perp}=0} \quad (7.6)$$

with the variables of integration s' and s being distances along ray paths, and \vec{r}_{\perp} the transverse coordinate, as the rays are brought to a focus in the SBS medium. The propagation distance in the medium to the front of the focal region is ℓ .

The distortion parameter is easily evaluated for a Gaussian-shaped beam. The result for the CW or quasi-CW cases is as follows:

$$DP = \frac{dA}{dt} \frac{16t}{\pi\lambda^2}, \quad (7.7)$$

where $\frac{dA}{dt} = \left| \frac{dn}{dT} \right| \frac{\alpha P}{n\rho C_p}$

and $t = \begin{cases} \text{long-pulse duration or} \\ \lambda F\# / V, \text{ with cross-flow } V. \end{cases}$

In the CW or quasi-CW cases, the useful criterion is that DP be less than unity. The conclusion for thermal blooming is that the absorbed power per unit cross-flow speed be less than

$$\alpha PF\# / V < 3 \text{ (W/cm)}^2 \text{ (m/s)} \quad (7.8)$$

$F\#$ = beam F-number

n = refractive index

λ = wavelength

V = cross-flow speed

C_p = specific heat

P = input power

α = absorption coefficient

ρ = density

T = temperature

The condition that the distortion parameter be less than unity in the CW or quasi-CW case and the condition that the cross-flow not even halve the gain coefficient [see Equation (7.2)] can be combined to give the condition that

$$\alpha P < 15 \text{ W/cm}^2, \quad (7.9)$$

or, with the absorption coefficient α about $3 \cdot 10^{-6} \text{ cm}^{-1}$, that the input power satisfy the condition

$$P < 5 \text{ MW} . \quad (7.10)$$

The input power for the COS experiments is not to exceed 5 MW. The range of f/number is to be 15 to 30, which is consistent with the condition stated above for the input power.

The CW or quasi-CW case for self-focusing is not greatly affected by subsonic cross-flow. Self-focusing in xenon at HF wavelengths is likely to be mostly electrostrictive. The gas pressure increases to balance the electrostrictive pressure. The resulting increase in gas density and in refractive index is the same as without the cross-flow to terms of order squared in the Mach number.

The pulsed cases require a different condition on the input power. Namely, a condition that limits the change in the intensity distribution during the SBS acoustic wave rise time. Otherwise the SBS phase conjugation would not be able to keep up with the beam changes. A simple condition taken here is that the change in the distortion parameter be small in a phonon rise time.

This condition is written as

$$\tau \frac{dDP}{dt} < 1 , \quad (7.11)$$

where τ is the phonon rise time and $d(DP)/dt$ is the time-derivative of the distortion parameter DP. Upon evaluating this expression for a Gaussian beam, the condition becomes

$$\frac{dA}{dt} \frac{\tau t^2}{t_s^2} \frac{8}{\pi \lambda^2} < 1 \quad (7.12)$$

or

$$\alpha P < \frac{60 \text{ W/cm}}{(t/t_s)^2} \quad (7.13)$$

$$t_s = \frac{\lambda F/\#}{C_s} \quad (7.14)$$

where

τ = phonon rise time = 0.26 μ s for 40-atm Xe

F/# = focal length/beam diameter

C_s = sound speed

λ = wavelength

or

$$P < 20 \text{ MW}/(t/t_s)^2, \text{ when } \alpha = 3 \times 10^{-6} \text{ cm}^{-1}. \quad (7.15)$$

The square of the ratio of pulse time to sonic transit time appears, as discussed earlier. This ratio is supposed to be less than unity. A rectangular pulse in time is assumed for the sake of simplicity.

Similar analysis is done with pulsed self-focusing. The product, phonon rise time times the time derivative of the distortion parameter (actually, its negative), is to be less than unity. The condition on input power is as follows:

$$\frac{P}{P_c} \frac{t\tau}{t_s^2} < 1, \text{ with } P_c = n c \lambda^2 / (128 n_2) \approx 1 \text{ MW}, \quad (7.16)$$

where the nonlinear refractive index coefficient n_2 is taken as

$$n_2 = \frac{\left(\rho \frac{\partial \epsilon}{\partial \rho}\right)^2}{16\pi \rho C_s^2 n} \approx 0.15 \times 10^{-11} \text{ esu, for 40-atm Xe,} \quad (7.17)$$

where

$$\rho \frac{\partial \epsilon}{\partial \rho} \approx \frac{(\epsilon-1)(\epsilon+2)}{3} \quad (7.18)$$

ϵ = dielectric constant = n^2

ρ = density

The condition on input power for the pulsed self-focusing case is also consistent with the upper limit of 5 MW and f/number range of 15 to 30.

Optical breakdown in the SBS cell might be most influential. Experiments at 1.35 μm wavelength (Ref. 7.3) indicate a breakdown threshold intensity of about 20 GW/cm^2 at 40 atm xenon. Scaling to HF wavelength (2.8 μm) by an inverse or an inverse-square wavelength dependence yields an estimate of 5 to 10 GW/cm^2 for the breakdown threshold intensity. Then, the condition that the pump intensity that is transmitted through the forward-positioned SBS region to the focal region be less than this threshold is

$$P < 4 (F/\#)^2 / (1-R), \text{ in kW}, \quad (7.19)$$

where R is the SBS reflection coefficient. The full state of affairs for the SBS/breakdown interaction is not yet known.

The opposing effects of thermal blooming and self-focusing can be made to cancel with the appropriate absorption coefficient and corresponding exponentially rising time history for the pulsed case or exponentially grow in spatial profile in the flow direction in the region just forward of the Rayleigh range. The 1/e-folding time is given by

$$\left[\rho \frac{d\epsilon}{d\rho} \right] / [a(\gamma-1)c] \quad (7.20)$$

c = light-speed

γ = ratio of specific heats

7.3 M.A. Greimer-Mothes and K.J. Witte, preprint, 1986.

and the 1/e-folding distance is the cross-flow speed times this time-constant (Ref. 7.4).

For xenon at 40 atm with less than 0.1 ppmv impurity level, the time-constant is a convenient 1 μ s. With 20 m/s flow speed, the distance is 20 μ m, which is to be compared to the focal spot diameter of 6 F/# μ m at HF wavelength.

7.3 SUBSCALE EXPERIMENTS

The overall objective of the subscale experiments task has been to provide preliminary experimental data to support the PALS design activities on phase conjugation related issues. Specifically, these experiments were designed to study the SBS threshold and reflectivity, and conjugation fidelity as a function of the following experimental parameters: (1) f/number of the SBS telescope, and (2) bandwidth.

The f/number of the SBS telescope has a significant impact on the APACHE system design. Based on modeling and numerical analysis it is believed that the threshold for the SBS process should be independent of the f/number of the focusing telescope, but prior to these experiments no documented experimental results were available. Furthermore, the effect of f/number on conjugation fidelity was an issue which had received relatively little attention but significantly impacts system design.

The bandwidth of the pump laser also impacts the conjugation process. The SBS process requires a finite length over which the Stokes beam interacts with the pump to produce the phase conjugate return. If the coherence length of the laser is less than this SBS interaction length then the reflectivity and fidelity of the conjugate return will be degraded. In the subscale experiments, the plan was to run the laser both narrow band (with the SAM single axial mode etalon in place) and broadband (with the SAM removed) with variations in the SBS interaction length being controlled by the f/number of the focusing lens.

7.4 P.R. Longaker and M.M. Litvak, Journ. Appl. Phys., 40, 4033-4041 (1969), see eq. (A6). Note on Eq. (A3): Divide r.h.s. by $(\gamma-1)$. Note on eq. (A5): c is light speed here only.

A key output of this experimental program is a data base for validating the upgraded capabilities of the BOUNCE code, which was modified during the PALS program to include the effects of near-field aberrations and absorption. The data also were to supply information for setting medium purity requirements on the conjugating material as well as flow rates in the flowing SBS cell, and to assist in setting system level requirements (notably the f/number of the SBS telescope).

Figure 7-2 shows a schematic layout of the test setup used for these experiments. A photograph of the facility is presented in Figure 7-3. The laser source is a Molectron Nd:YAG laser operating at $1.06 \mu\text{m}$ with a pulse length of approximately 15 ns (FWHM) and a maximum pulse energy of 250 mJ (in practice, to avoid damage to the spatial filter the pulse energy was kept below about 100 mJ). The beam hits a turning flat and is directed to a multielement telescope with a 3 m effective focal length with a spatial filter positioned at focus. This focal length was chosen to keep the fluence levels at focus below damage levels of the spatial filter and air breakdown levels. Beam splitters are located on both sides of the spatial filter for joule-meter readings. Beyond the telescope, the beam is recollimated and directed to the SBS focusing lens which is varied over the f/number range of 10 to 50. Two SBS cells were used in the study using CCl_4 and xenon. All of the successful experiments performed to date utilized the liquid CCl_4 cell. Further work using the high pressure xenon cell is to be deferred to the APACHE program.

Measurements of the characteristics of the laser are presented in Figures 7-4 and 7-5. The far-field intensity distribution of the laser measured using a CID camera and the beam quality are shown in Figure 7-4. Using the power-through-the-pinhole technique, the beam quality of the beam incident on the SBS cell is measured to be $\text{BQ}=1.10$. Figure 7-5 shows the bandwidth characteristics of the laser measured using a Fabry-Perot interferometer. With the SAM (single axial mode) etalon in place, the bandwidth of the laser at $1.06 \mu\text{m}$ is measured to be approximately 200 MHz, yielding a coherence length of 1.5 m. The $P(t)$ trace obtained simultaneously with the bandwidth measurements shows the characteristic shape of a Q-switched laser with a sharp rise followed by a somewhat longer decay. With the SAM

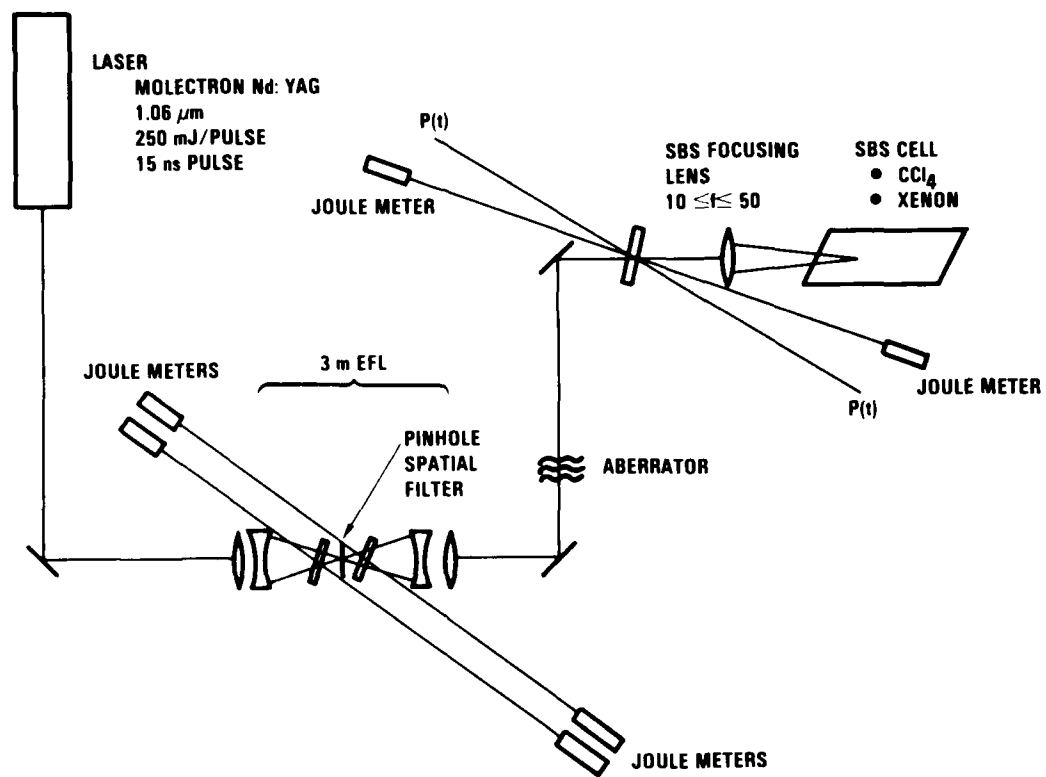
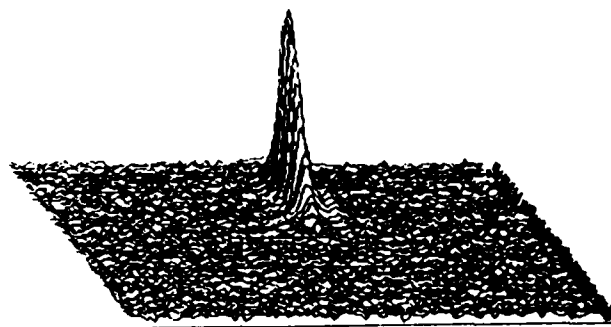


Figure 7-2. Schematic layout of experimental test setup.



Figure 7-3. Photograph of the experimental facility.



CID Isometric



Contour Plot

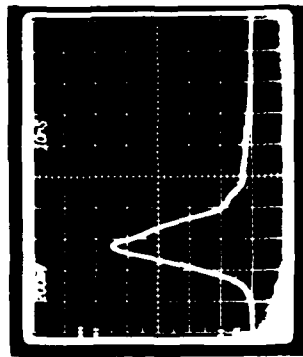
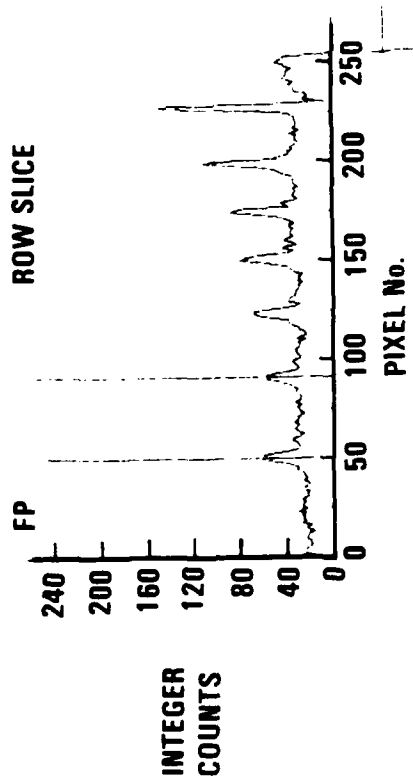
BQ into SBS cell = 1.10

• **Power through pinhole method**

Figure 7-4. Measurements of the Nd:YAG laser far-field intensity distribution and beam quality.

removed, the character of the $P(t)$ trace is significantly altered, with several peaks and dips noted in the trace. The Fabry-Perot interferogram for this case shows the bandwidth to be about 13 GHz, corresponding to a coherence length of slightly over 2 cm.

Several examples of SBS conjugation using $P(t)$ traces from the CCl_4 liquid cell are presented in Figure 7-6. In the oscilloscope traces, both the incident pump beam and the Stokes return (time delayed by approximately 50 ns on the trace) are shown on the same sweep. The first series of tests shows the effect of amplitude of the pump beam on the conjugate return. For an incident pump beam energy of 1.9 mJ, no Stokes return is observed. This result is consistent with the calculated energy threshold for SBS in CCl_4 of 4.4 mJ (based on a conversion from power to energy using FWHM). When the pump energy is increased to 2.9 mJ, a Stokes return is observed with a peak reflectance of approximately 50 percent, while reflectivity measured in terms of energy is 14 percent. This disparity between power and energy reflectivity results from the fact that the phonon rise time in CCl_4 at $1.06 \mu\text{m}$ (9 ns) is comparable to the duration of the pump beam pulse. Note that the observance of an SBS return at an energy level below the calculated value is an indication that the computation of threshold

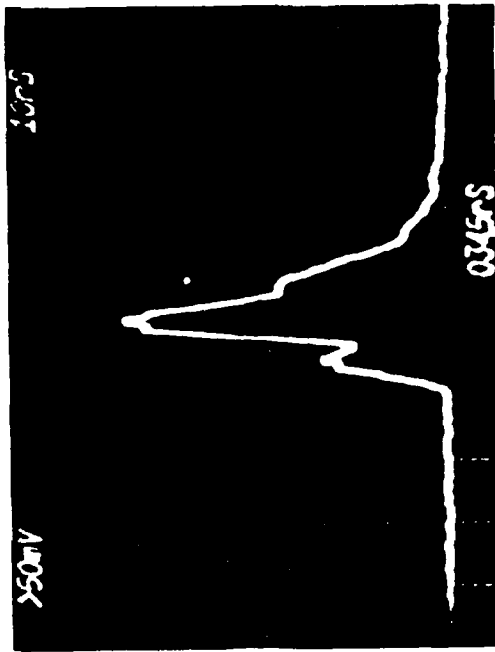


P(t)

BW = 195 MHz
 $L_{COHERENCE} = 1.5 \text{ m}$

FABRY-PEROT

Bandwidth (SAM etalon removed)



BW = 13 GHz
 $L_{COHERENCE} = 2.3 \text{ cm}$

Figure 7-5. Laser bandwidth measurements.

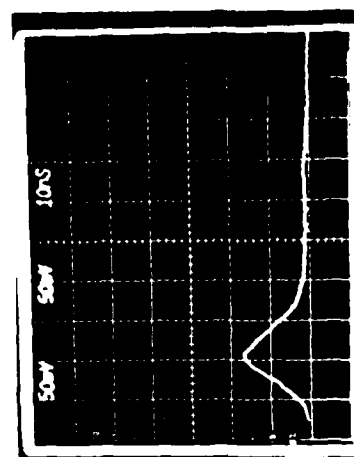
energy using the pulse FWHM to convert from power to energy is only an approximation. A more definitive comparison would be to compare the instantaneous power from the $P(t)$ trace at the point in time when the SBS process begins, and such a determination is presently being made. In the last trace of this series, the pump beam energy is increased to 17.1 mJ, and the reflectivity of the Stokes return is about 50 percent in terms of energy and over 80 percent in terms of peak power.

Also shown in Figure 7-6 is an example of a trace obtained when the laser was operating multimode, such that evidence of mode beating is observed. The interesting feature from these results is that the high frequency structure of the mode beating which is superimposed on the pulse is reproduced by the conjugate return, even though the rise time for this structure (approximated to be less than 1 ns) is significantly faster than the phonon rise time. This type of response is predicted for broadband input as long as the coherence length is longer than the interaction length. Some attenuation in this high frequency structure is observed in the SBS return, however, indicating that the phonon rise time has acted as a low pass filter.

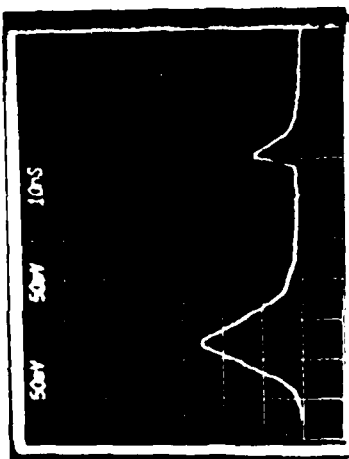
The remaining experimental data to be presented deal with the effects of f /number on conjugation threshold and reflectivity. Figure 7-7 shows the results of SBS energy reflectivity experiments performed as a function of f /number of the SBS focusing lens over the range of $f/10$ to $f/50$. The data are plotted in the form of reflected energy as a function of incident beam energy. From these results it is observed that both the threshold and reflectivity of the SBS conjugate return (having a slope efficiency of 90 percent) are independent of f /number over the range of f /numbers investigated.

An interpretation of these results may be made using the expression for the small signal gain. From analytical modeling it is known that the threshold for SBS phase conjugation occurs when the SBS small signal gain, equal to g , the gain coefficient of the medium, times I , the intensity, times l , the pump/Stokes interaction length, is greater than approximately 25. As the f /number of the focusing lens changes, both the intensity of the beam near focus and the depth of focus (DOF) change such that $I(\text{DOF})$ is

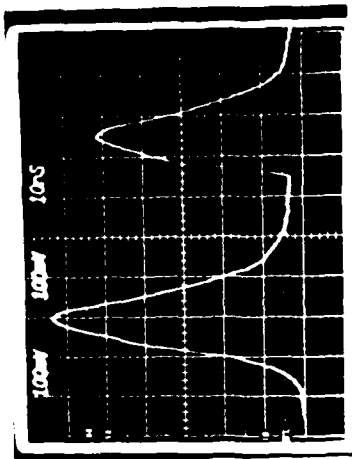
SBS reflectivity as function of incident energy



$E_{in} = 1.9 \text{ mJ}$
 $E_{out} = 0$

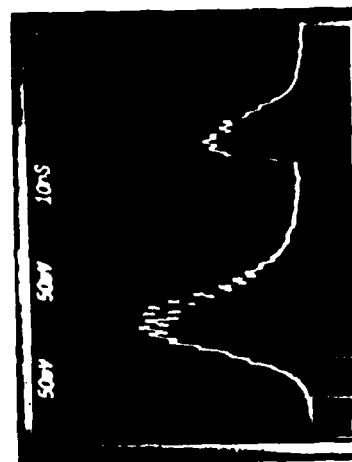


$E_{in} = 2.9 \text{ mJ}$
 $E_{out} = 0.4 \text{ mJ}$
 $R = 0.14$
 $E_{\text{calculated threshold}} = 4.4 \text{ mJ}$



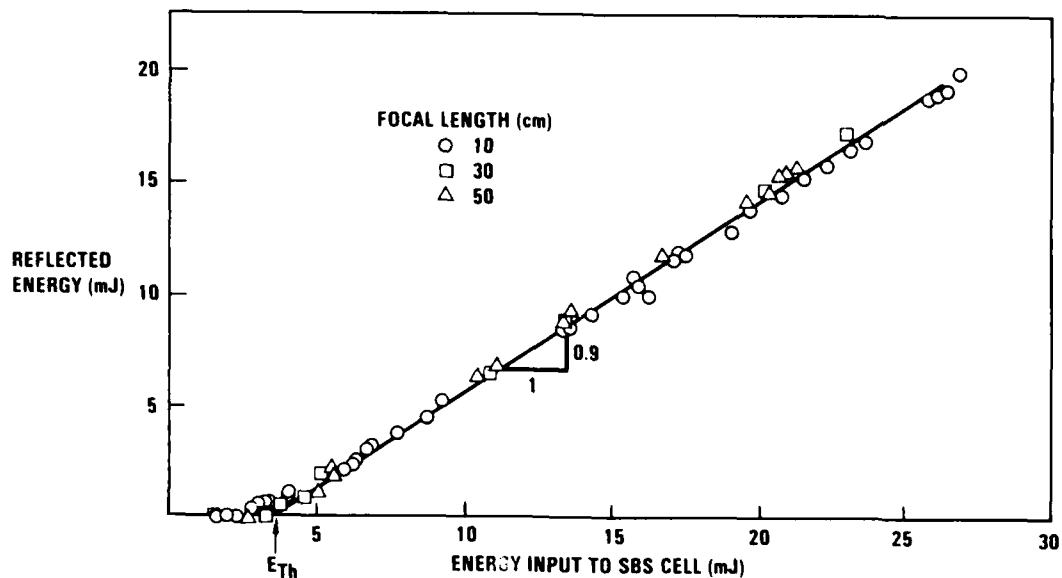
$E_{in} = 17.1 \text{ mJ}$
 $E_{out} = 8.7 \text{ mJ}$

Example of laser multimoding reproduced by SBS return



Incident energy = 5.9 mJ
 Reflected energy = 1.6 mJ

Figure 7-6. Examples of SBS reflectivity using CCl₄.



SBS threshold and reflectivity independent of f/number

- Slope efficiency = 0.9
- Threshold: 3.5 mJ (measured)
4.4 mJ (calculated based on FWHM)

Figure 7-7. Effect of f/number on reflectivity

a constant. The data shown in Figure 7-7 suggest that as the intensity varies, the length of the region over which significant interaction between the pump and the Stokes correspondingly changes such that the gIL product exceeds that for conjugation threshold. It is believed that this process will continue until the required interaction length for SBS exceeds the coherence length of the laser after which both the reflectivity and the fidelity of the conjugate beam will be degraded.

The data presented in Figures 7-7 summarize the present status of the experiments performed on the PALS program. As part of the follow-on work to be performed on the APACHE program, several additional experiments are planned to address all of the issues previously identified in the experimental objectives. This work will include examining the effects of f/number on conjugation fidelity, aberrations in the near field, absorption in the conjugating medium, and effects of finite phonon rise time using xenon as the conjugation medium.

One of the issues which still remained at the conclusion of the PALS program in the area of subscale experiments was conjugation using xenon gas. Preliminary attempts to use a xenon cell for phase conjugation were unsuccessful, in that poor reflectivity was obtained, and gas breakdown may also have been occurring. Following the CDR presentation at NRL, additional effort was undertaken to assess the cause of these difficulties as part of the final report preparation. This work revealed that a potential cause for these problems lies in contamination of the gas caused by impurities within the cell. Because of the specific nature of the design of the cell, attempts to remove these impurities proved to be unsuccessful. Since these impurities appeared to be the cause of the poor conjugation performance, a new cell was designed with medium purity as an important requirement. The cell has been fabricated, and preliminary inspection suggests that the medium purity difficulties experienced earlier will not be encountered in the new design.

END

DTIC

8-86